POLITECNICO
MILANO 1863

SCUOLA DI INGEGNERIA INDUSTRIALE
E DELL'INFORMAZIONE

Synchronous high revisit mixed sensor constellation: architectural design optimisation and trade-offs for emergency response

Tesi di Laurea Magistrale in
Space Engineering - Ingegneria Spaziale

Author: **Alessandro Federico Catalano**

Student ID: 10539416
Advisor: Prof. Camilla Colombo
Co-advisors: Dott. Ing. Luca Soli
Academic Year: 2021-22

This content is original, written by the Author, Alessandro Federico Catalano. All the non-originals information, taken from previous works, are specified and recorded in the Bibliography.

When referring to this work, full bibliographic details must be given, i.e.

Alessandro Federico Catalano, "Synchronous high revisit mixed sensor constellation: architectural design optimisation and trade-offs for emergency response". 2023, Politecnico di Milano, Master Thesis in Space Engineering, Supervisor: Camilla Colombo, Co-supervisor: Luca Soli.

Abstract

This study addressed the design of a synchronous high revisit constellation of optical and Synthetic Aperture Radar (SAR) small satellites dedicated to emergency response in Italy. The constellation was optimised for optical and SAR data fusion. In fact, optical and SAR data can be fused and jointly analysed to improve the information content; however, the two acquisitions should be made within a short time interval (or synchronously), especially when fast time-changing phenomena are involved, such as emergencies.

Three new figures of merit that express the synchronous constellation's performance were presented and optimised in this work. These new figures of merit are the synchronicity time, synchronous revisit time and synchronous coverage. In particular synchronicity time expresses the required time interval between the optical and SAR acquisitions and, in this thesis, it is introduced as a variable that has to be minimised, rather than as a fixed value imposed by the designer. Moreover, the main sources of uncertainties are discussed, and then the Pareto front that expresses the compromise between synchronous performance and cost drivers was found by employing a variation of NSGA-II. Three constellation orbital architectures were analysed: a Walker pattern with optical and SAR satellites on Sun-synchronous orbits, a Walker with satellites in generally inclined orbits, and a hybrid pattern with optical satellites on Sun-synchronous orbits and SAR satellites in generally inclined orbits. Results show that synchronicity time has a strong influence on synchronous revisit time, synchronous coverage and costs. Moreover, The pattern with satellites on inclined orbits yields the best results for regional coverage over Italy. However, optical satellites on Sun-synchronous orbits can provide more consistent performances over seasons due to favourable illumination conditions.

This work has been developed as a collaboration between Thales Alenia Space Italia S.p.A. and the Department of Aerospace Science and Technology of Politecnico di Milano.

Keywords: constellation design, data fusion, Synthetic Aperture Radar (SAR), optical, multi-objective optimisation, floods, critical infrastructures, Earth observation, hybrid constellation, synchronisation

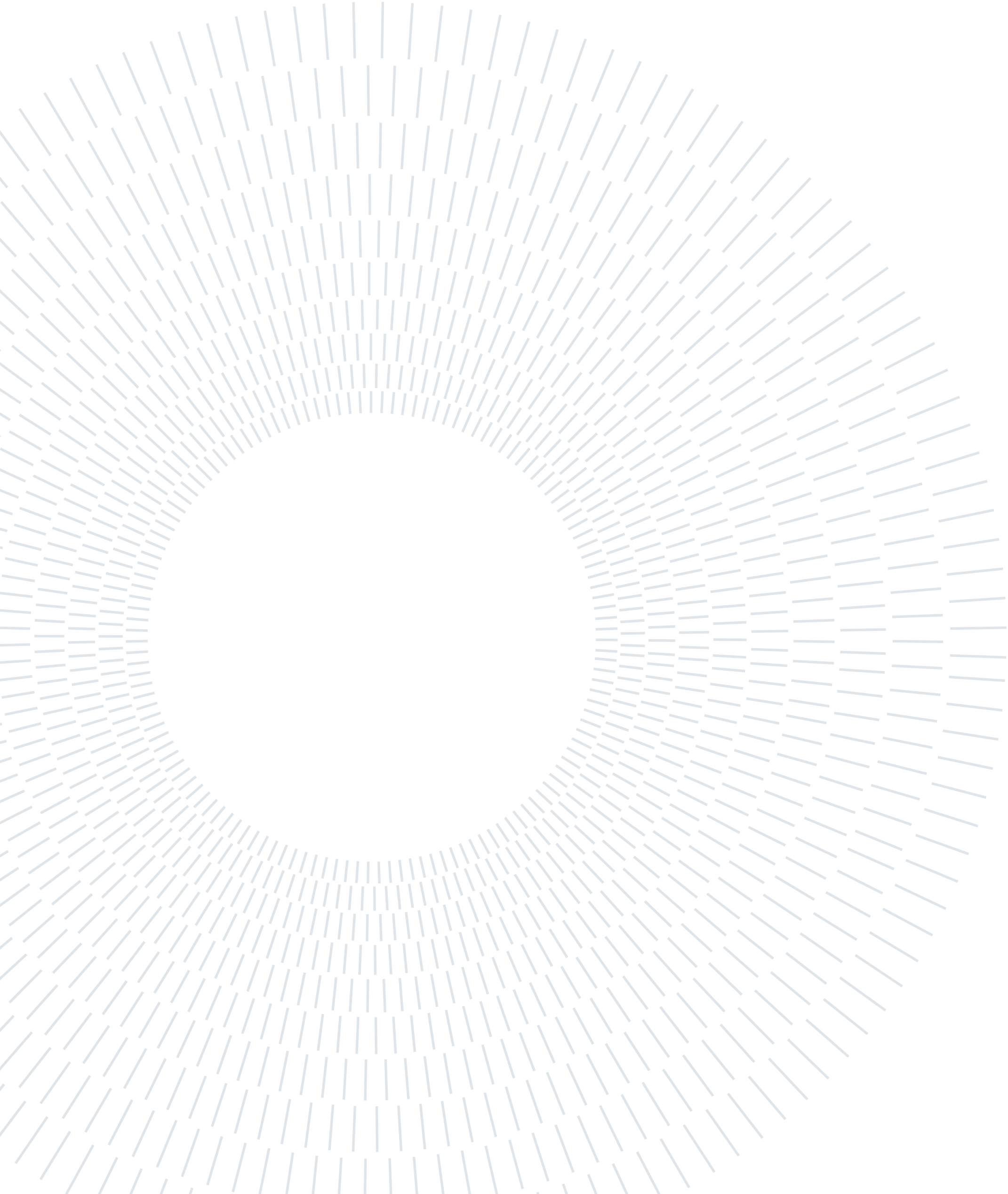

Sommario

Questo studio ha affrontato la progettazione di una costellazione sincrona ad alta rivisita di piccoli satelliti ottici e Synthetic Aperture Radar (SAR) dedicata alla risposta alle emergenze in Italia. La costellazione è stata ottimizzata per la fusione di dati ottici e SAR. Infatti, questi dati possono essere fusi e analizzati congiuntamente per migliorare il contenuto informativo; tuttavia, le due acquisizioni dovrebbero essere effettuate entro un breve intervallo di tempo (o in modo sincrono), soprattutto quando sono coinvolti fenomeni di cambiamento temporale rapido, come le emergenze.

In questo lavoro sono state presentate e ottimizzate tre nuove figure di merito che esprimono la performance della costellazione sincrona. Queste sono il tempo di sincronicità, il tempo di rivisita sincrono e la copertura sincrona. In particolare il tempo di sincronicità esprime l'intervallo di tempo richiesto tra le acquisizioni ottiche e SAR e, in questa tesi, viene introdotto come una variabile che deve essere minimizzata, piuttosto che come un valore fisso imposto dal progettista. Inoltre, le principali fonti di incertezza sono state discusse, e il fronte di Pareto che esprime il compromesso tra prestazioni sincrone e driver di costo è stato trovato, impiegando una variante di NSGA-II. Sono state analizzate tre architetture orbitali di costellazione: un pattern Walker con satelliti ottici e SAR su orbite eliosincrone, un pattern Walker con satelliti in orbite generalmente inclinate e un pattern ibrido con satelliti ottici su orbite eliosincrone e satelliti SAR in orbite inclinate. I risultati mostrano che il tempo di sincronicità ha una forte influenza sul tempo di rivisita sincrono, sulla copertura sincrona e sui costi. Inoltre, il pattern con satelliti su orbite inclinate fornisce i migliori risultati per la copertura regionale sull'Italia. Tuttavia, i satelliti ottici su orbite eliosincrone possono fornire prestazioni più costanti nel corso delle stagioni grazie a condizioni di illuminazione favorevoli.

Questo lavoro è stato sviluppato in collaborazione tra Thales Alenia Space Italia S.p.A. e il Dipartimento di Scienze e Tecnologie Aerospaziali del Politecnico di Milano.

Parole chiave: progettazione di costellazioni, fusione dati, radar ad apertura sintetica (SAR), ottico, ottimizzazione multi-obiettivo, inondazioni, infrastrutture critiche, osservazione della Terra, costellazioni ibride, sincronizzazione

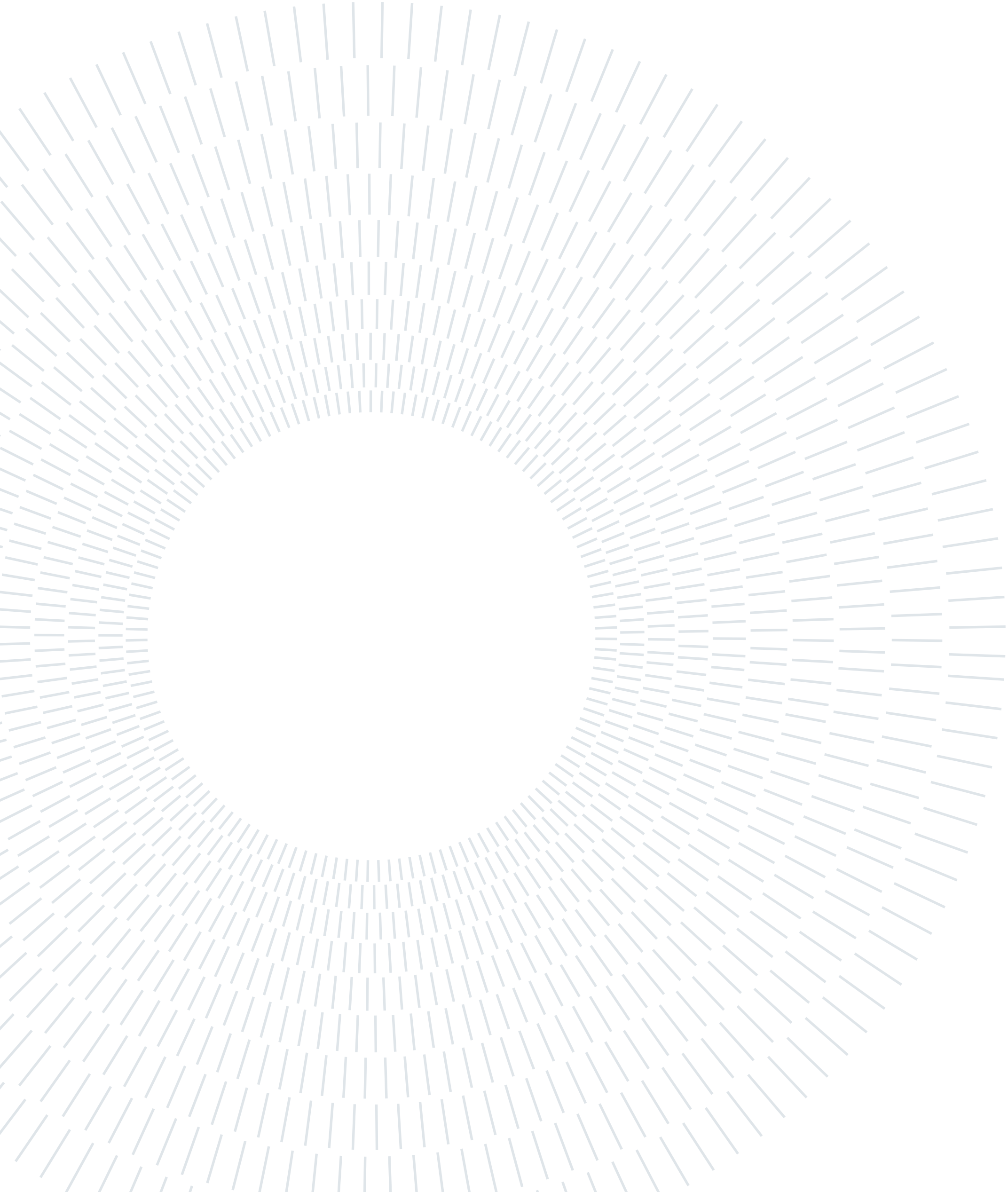

Contents

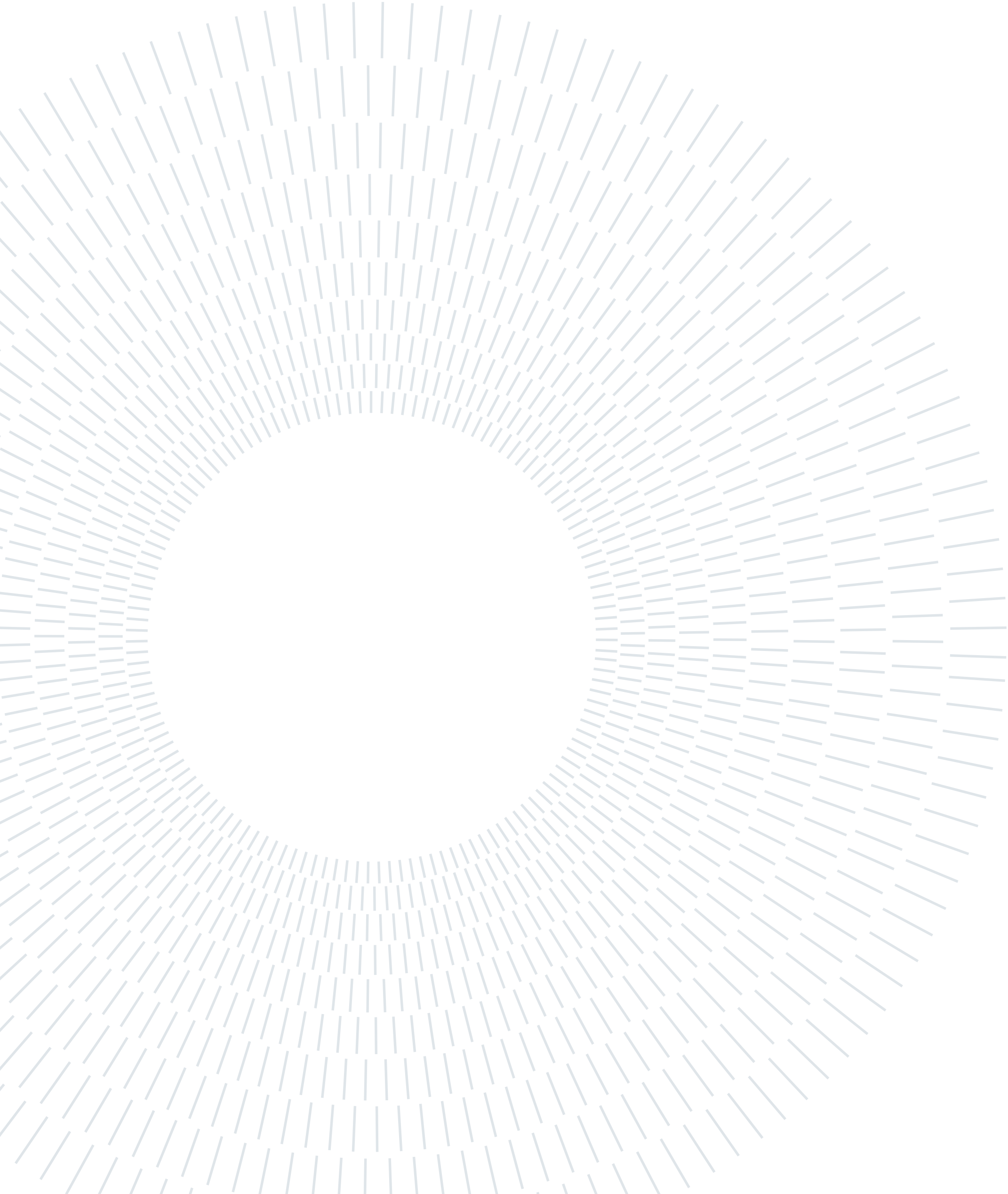

List of Figures

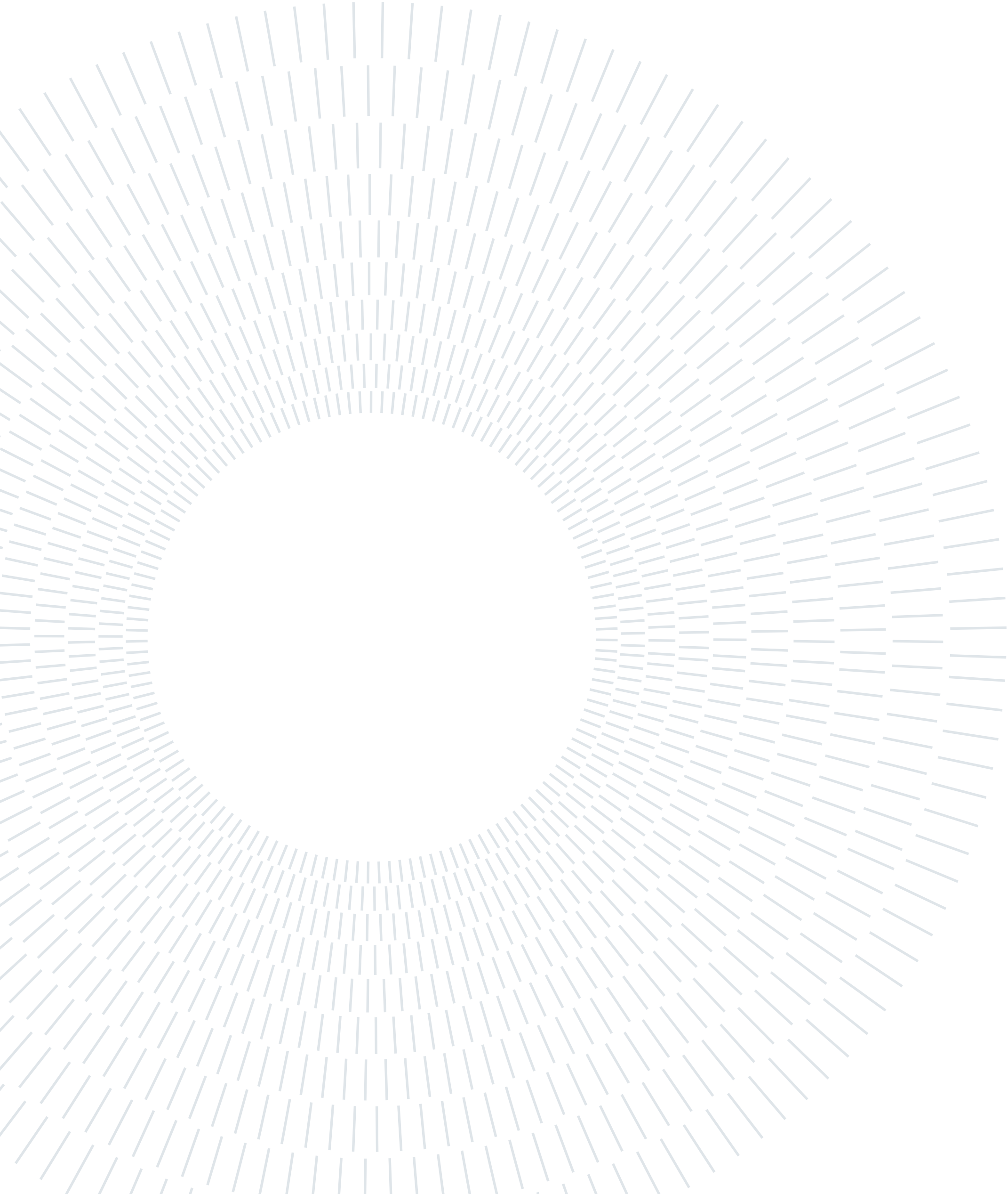

List of Tables

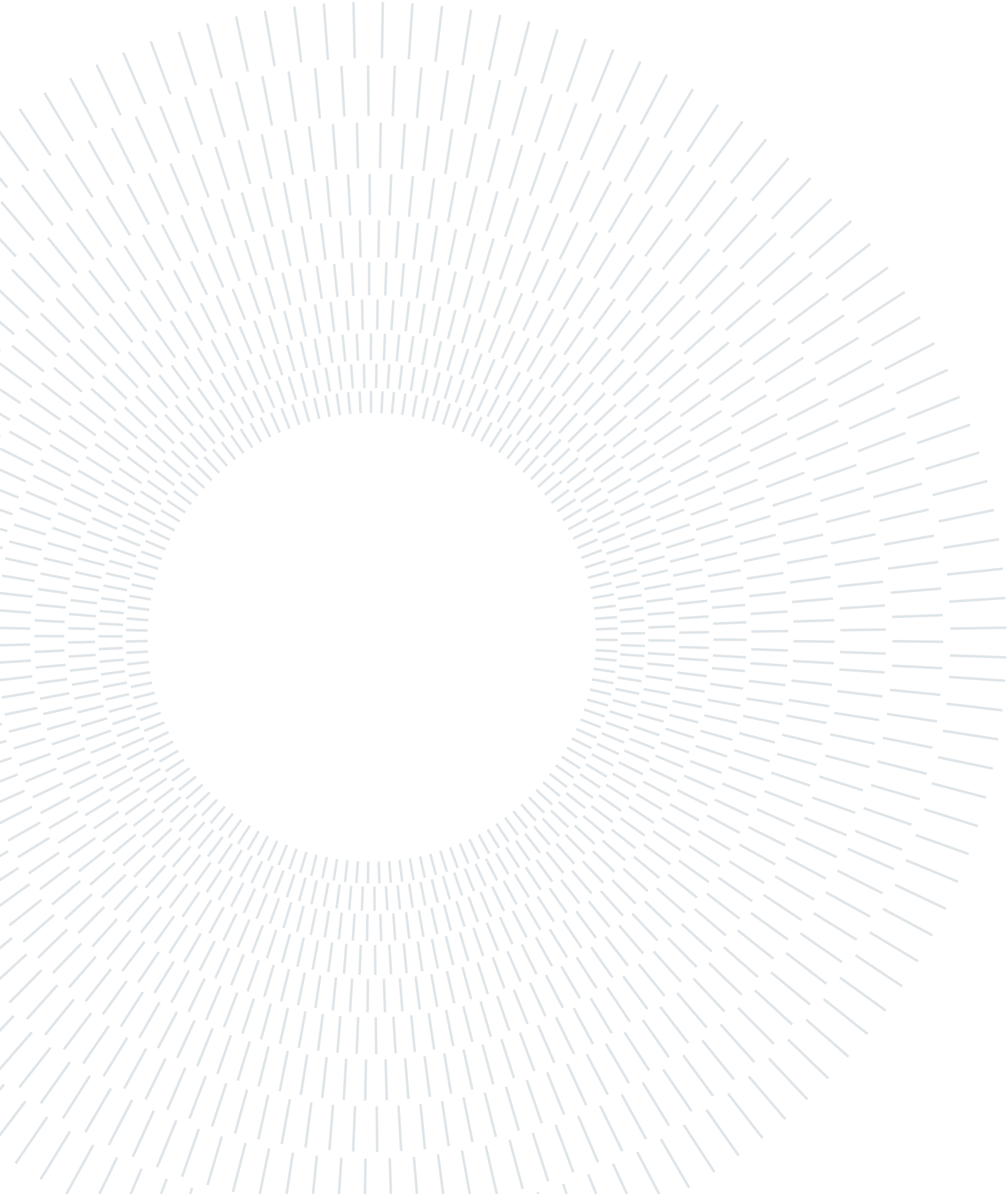

Nomenclature

Symbols

Variable	Description	SI unit
a	Orbit semi-major axis	[km]
B_d	Doppler bandwidth	[Hz]
B_p	Chirp bandwidth	[Hz]
$B_\perp$	Critical baseline	[m]
c	Speed of light	[m/s]
dp	Pixel size	[µm]
e	Orbit eccentricity	[-]
ϕ	Interferometric phase	[rad]
F	Walker phasing parameter	[-]
F_l	Optical focal length	[m]
$\mathbf{F}$	Objective functions vector	
f	Objective function	
FOV	Field of View	[deg] or [rad]
GSD	Ground Sampling distance	[m]
H	Satellite altitude	[km]
i	Orbit inclination	[deg] or [rad]
k	Revolutions for ground track repetition	[-]
L_{det}	Detector size	[µm]
l	SAR antenna aperture	[m]
λ	Wavelength	[m] or [µm]
M	Mean anomaly	[rad]
m	Days for ground track repetition	[-]
n	Mean motion	[rad/s]

Ω	Right Ascension of the Ascending Node (RAAN)	[deg] or [rad]
ω	Argument of perigee	[deg] or [rad]
$\omega_\oplus$	Earth's angular rotation	[deg] or [rad]
P	Number of planes	[-]
PRF	Pulse repetition frequency	[Hz]
R	Range	[m]
ρ_a	Azimuth resolution (Az.)	[m]
ρ_g	Ground range resolution (Rg.)	[m]
ρ_r	Slant range resolution	[m]
S	Number of satellites per plane	
T	Number of satellites	[-]
T_n	Nodal period	[s]
T_{θ_G}	Greenwich nodal period	[s]
θ	True anomaly	[deg] or [rad]
θ_i	Incidence angle	[deg] or [rad]
τ_p	Pulse length	[s]
W	SAR antenna width	[m]

Acronyms

DEM	Digital Elevation Model
DInSAR	Differential Synthetic Aperture Radar Interferometry
ε-NSGAII	Epsilon Dominance Non-dominated Sorting Genetic Algorithm II
EA	Evolutionary algorithm
EO	Earth observation
ESA	European Space Agency
GEO	Geosynchronous Orbit
GPS	Global Positioning System
InSAR	Interferometric Synthetic Aperture Radar
IPCC	Intergovernmental Panel on Climate Change
ISPRA	Institute for Environmental Protection and Research
LEO	Low Earth Orbit
LTAN	Local time at ascending node
LTDN	Local time at descending node

MINSGA	Modified Illinois Non-dominated Sorting Genetic Algorithm
MOEA	Multi-Objective Evolutionary Algorithm
MOEA/D	Multi-Objective Evolutionary Algorithm based on Decomposition
MOOP	Multi-Objective Optimisation Problem
MOPSO	Multi-Objective Particle Swarm Optimisation
MS	Multispectral
NIR	Near-Infrared
NSGA-II	Non-dominated Sorting Genetic Algorithm II
PAN	Panchromatic
PNRR	National Recovery and Resilience Plan
PS	Permanent Scatterer
RADAR	RAdio Detection And Ranging
RAR	Real Aperture Radar
SAR	Synthetic Aperture Radar
SLAR	Side Looking Airborne Rada
SNR	Signal-to-Noise Ratio
SoC	Streat-of-Coverage
SSO	Sun-Synchronous Orbit
SWIR	Short-Wavelength Infrared
TSO	Transmission System Operator
UAV	Unmanned Aerial Vehicle
VIS	Visible
VNIR	Visible and Near-Infrared
WMO	World Meteorological Organization

Constants

Earth gravitational parameter $\mu \approx 3.9860 \times 10^5\,\mathrm{km}^3/\mathrm{s}^2$

Earth mean equatorial radius $R_\oplus \approx 6378.16\,\mathrm{km}$

Earth's second zonal harmonics $J2 \approx 1.0826e-3$

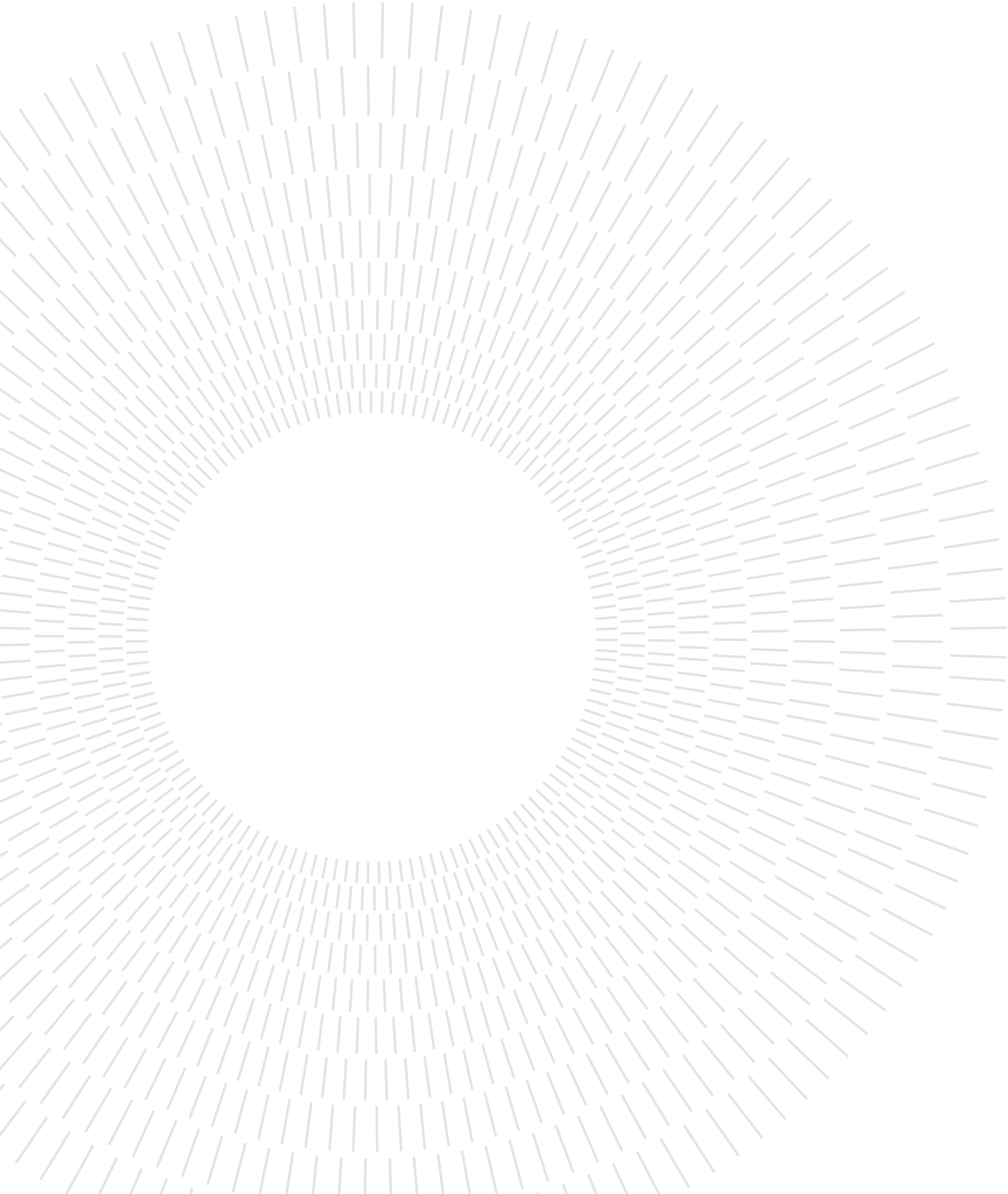

1 | Introduction

1.1. Context and motivation

Earth observation (EO) is defined as the process of gathering information about the Earth's surface and atmosphere via remote sensing instruments [1]. These data can be acquired from different platforms, namely unmanned aerial vehicle (UAV), drones, planes or satellites, each posing advantages and disadvantages. The main benefit of using satellites is related to their potential to cover large areas of the globe with regular observations. On the contrary, planes usually provide better spatial resolution, but they present additional costs and issues associated with the necessity of employing the related workforce, such as pilots and technicians. Drones and UAVs solve these problems, but they are limited by regulations and lower carrying capacity.

EO data can be gathered with many typologies of instruments, such as optical and Synthetic Aperture Radar (SAR) sensors. Optical instruments are passive sensors that deliver high-resolution images providing information about the spectral properties of the sensed target. However, they require good illumination conditions and cannot operate in the presence of clouds or smoke. On the contrary, SAR sensors are active instruments that can operate in any illumination conditions and penetrate clouds. They are sensitive to scattering mechanisms influenced by the roughness and dielectric proprieties of the target and can exploit phase information to measure small deformations.

The geospatial information derived from satellite data is already exploited in many commercial sectors, such as energy, transport, utilities, agriculture and insurance. In fact, EO data can be used for a wide variety of applications, including characterising land use (urban analysis, precision farming), detecting damage caused by natural and human-made disasters (floods, hurricanes, earthquakes, oil spills), providing information about the exploitation of resources (oil fields, minerals), and supporting defence and security [2], [3]. Furthermore, by acquiring images of a scene at different times, it is possible to monitor environmental variables such as vegetation phenology and snow cover, and to observe the impact of human activities like urban sprawl and deforestation [2]. In addition, they can be instrumental in understanding and mitigating the impact of climate change [2].

The devastating effects of climate change are already evident in our times, and the frequency of extreme climate events that can threaten our society is increasing. The Intergovernmental Panel on Climate Change (IPCC), in its Sixth Assessment Report (AR6) [4], highlighted how extreme events such as floods, heavy precipitations, droughts and fire weather have already increased in frequency and are expected to increase even more in the next few years. Therefore, mitigation, adaptation, and risk management strategies are fundamental for reducing social and economic risks caused by climate change and the consequent catastrophes. EO solutions can play a crucial role in the management of natural disasters in any phase of the emergency management cycle, including preparedness, early warning, response and recovery after the event. However, the most demanding phase is the emergency response because it requires timely EO data, which can be used to manage rescue operations and save human lives immediately after the disaster. For example, EO data can be employed during a flood to detect flooded areas and even measure the flood depth. Extreme climate events can also damage critical infrastructures that are essential in our society. For instance, overhead power lines are critical infrastructures particularly sensitive to strong wind, landslides, floods, snow and icing. EO solutions can effectively be adopted to monitor critical infrastructures and support decision-makers during an emergency. However, even in this case, timely observations are essential for a fast response. Therefore, in the future, frequent and timely observation will be crucial to enable and support new beneficial applications of EO.

Furthermore, data from different sensors, such as optical and SAR sensors, can be coupled and jointly analysed by data fusion practices to enhance the information content and improve the overall quality of the measurements [2]. Data fusion practices are currently widely applied in many remote sensing tasks, such as land cover mapping and agriculture [5]–[7], disaster management [8], [9] and urban infrastructure detection and monitoring [10]. However, to have meaningful information, the two sensors must observe the scene within a short time interval to avoid temporal decorrelation. *Synchronicity* between the acquisitions, defined as the capability of observing the same location with the two sensors within a short time interval, is essential for time-sensitive applications like disaster response and when fast time-changing phenomena are involved. Therefore, synchronous sensing can be critical for improving the quality of the fused data, thanks to the reduction of temporal decorrelation. However, it is not always possible to find acquisitions with this temporal characteristic at the target site [11], since data fusion is currently obtained by combining the information coming from independently operated sensors, such as Sentinel-1 and Sentinel-2, or Sentinel-1 and Landsat. Therefore, realising a hybrid optical and SAR constellation designed for obtaining synchronous acquisitions can fill this gap and solve the issue. However, no constellation of this kind exists at this moment.

Due to the importance that EO has in our modern society, many entities are currently investing in many upstream and downstream EO applications. The European Space Agency (ESA) budget allocated to this domain is growing, reaching 1768.7 M€ in 2023 (i.e. 25.0% of the total budget) [12]. In particular, ESA has developed seven EO missions under the Sentinel programme. These satellites contribute to the Copernicus programme, which monitors our planet and its environment, and provides free and open data, information and services for the ultimate benefit of the citizens of Europe [13]. Moreover, the Italian Government is investing 1.23 B€ in the EO domain thanks to the National Recovery and Resilience Plan (PNRR) as part of the Next Generation EU, the economic recovery package to support the European Union (EU) member states after the COVID-19 pandemic [14]. This investment will be partially employed to realise the IRIDE satellite constellation, which will serve both public administrations and commercial partners. In particular, eight services for public administrations have been identified: coastal service and maritime-coastal monitoring, air quality service, ground motion service, land cover and land use service, hydrometeorological service, water resources service, emergency service and security service [15], [16].

In the last decade, private companies have also invested in the EO sector in the context of the so-called New Space Economy. Therefore, small satellite optical and SAR constellations are becoming increasingly common thanks to technological miniaturisation, reduced launch cost and a growing demand for near real-time, high-resolution and high revisit data. These private companies have deployed many optical and SAR small satellite constellations in the last few years, such as ICEYE, Capella, PlanetScope, SkySat, and BlackSky. These small satellite technologies have complementary goals to large monolithic missions. In fact, large satellites can usually provide more accurate measurements and cover a more extended part of the planet thanks to their wider swath. On the contrary, small satellites can rely on their lower unit cost and the possibility of deploying multiple of them with a single launch or cheaper launch vehicles. In this way, larger constellations can be obtained, enabling a higher observation frequency of an area of interest.

1.2. Background

A constellation is defined as a set of satellites that work together as a system to achieve a common objective [17]. These systems are often adopted because they can provide a higher revisit rate than a single satellite and, in some cases, even give continuous coverage of the entire globe. For this reason, they are mainly used for Earth observation, communication, and navigation, where coverage and revisit requirements are particularly important [17]. However, the design of distributed satellite missions is challenging, as the range of potential architectures increases along with the number of satellites, and no general rules exist for constellation design [17]. Nevertheless, several studies have approached the problem of satellite constellation optimisation, trying to realise a design that minimises the cost while maximising the performance.

The first studies in this field were focused on finding the minimum number of satellites required to provide continuous global coverage or zonal coverage of latitude ranges. In 1961, Luders [18] proposed the Street-of-Coverage (SoC) theory, analysing the problem of providing continuous coverage of latitude bands. Successive works [19], [20] applied analytical method techniques to study the problem of providing redundant coverage (i.e. the same area is covered by more than one satellite) with SoC constellations. In the 1970s, Walker [21]–[23] introduced a symmetric constellation pattern with circular orbits with the same altitude and inclination, and he determined that continuous coverage of the Earth would require at least five satellites. Today, his constellation pattern, known as Walker Constellation, has reached great popularity. For example, it is used by the Galileo Navigation System constellation and the Global Positioning System (GPS) constellation. In the 1980s, Draim [24], [25] introduced high-altitude elliptic orbits and found out that four satellites would provide continuous Earth coverage.

However, the coverage problem for Earth observation systems differs from navigation and communication satellites since it would be extremely expensive to have a constellation that provides continuous coverage of the whole Earth [17] due to the limited swath provided by remote sensing sensors. In fact, the swath of optical and SAR sensors can reach some hundreds of kilometres at maximum, and it is even smaller for high and very-high resolution sensors. Thus, only discontinuous coverage can be practically achieved, and the analysis mainly focuses on minimising the gap between the observations [17].

Therefore, different approaches have been used to face the more complex problem of discontinuous coverage. For instance, Ulybyshev's [26] geometrical method can be utilised to calculate the maximum revisit time of symmetric constellations. However, this method has some limitations since it assumes that each satellite carries the same instrument, with a nadir-pointing conical field-of-view, and orbital perturbations are neglected. The advancement of computational tools for numerical simulations led to significant advancements in constellation design methods. These tools overcome the limitations of traditional geometrical methods and enable the analysis of satellites carrying instruments with more complex geometries. The orbits of the satellites can be accurately modelled to account for various perturbative forces and provide more advanced coverage metrics, like statistics on revisit and response times, rather than only maximum revisit time [27]. As a result, evolutionary algorithms, such as genetic algorithms and simulating annealing, have been widely used in constellation optimisation, thanks to their ability to combine integer and continuous variables and to deal with discontinuous and non-differentiable objective functions [28]–[30]. Early studies with genetic algorithms focused on minimising only a single objective, for example, intending to minimise the revisit time with a fixed number of satellites. However, constellation design is inherently a multi-objective problem since a compromise between competing requirements representing performance and cost must be found. In this case, multi-objective optimisation algorithms allow characterising the trade-off between competing objectives, providing a set of optimal solutions known as the Pareto front. The first usage of a multi-objective optimisation algorithm for constellation design has been found in Mason et al. [31], which demonstrated how genetic algorithms could be used to find a trade-off between performance and cost by using the Modified Illinois Non-dominated Sorting Genetic Algorithm (MINSGA). In the following few years, multi-objective genetic algorithms have been used to optimise different constellation patterns and objective functions [32]–[34]. In 2006, Ferringer and Spancer [35] employed the Non-dominated Sorting Genetic Algorithm II (NSGA-II) for the first time in this field, generating the set of optimal constellation designs that shows the trade-off between temporal and spatial resolution. This genetic algorithm has been one of the most used algorithms for constellation optimisation, and many studies in which this algorithm is used are available in literature [36]–[41].

Some researchers used a modified version of NSGA-II, changing, for example, the algorithm's selection, crossover, or mutation mechanisms. For instance, Reed et al. [42] and Whittecar and Ferringer [43] used a modified NSGA-II (i.e. ε-NSGA) based on ε-dominance selection mechanism. Hitomi and Selva [27] proposed a modified NSGA-II in which each candidate solution (or individual) is represented by a variable-length chromosome, optimising asymmetric constellations more efficiently. Only recently, new multi-objective optimisation algorithms have been explored, such as Multi-Objective Particle Swarm Optimisation (MOPSO) [44] and Multi-Objective Evolutionary Algorithm based on Decomposition (MOEA/D) [45], [46].

Despite the large number of studies investigating constellation design, the problem of mixed sensor synchronous constellations has been addressed only in the work of Chiatante [47]. In his research, Chiatante optimised a small satellite optical-SAR constellation, laying the foundations for defining the synchronous performances of a mixed sensor constellation. Starting from a previous work by Sartoretto [48] on SAR constellation design, Chiatante proposed an optical-SAR constellation with optical satellites placed in tandem (trailing or leading) to a SAR constellation optimised for the regional coverage problem over Italy. In particular, he fixed a maximum time interval between a pair of optical and SAR measurements required for synchronous optical-SAR data fusion, and he set its value to 60 seconds based on wildfire emergency requirements. In this way, he was able to optimise the daily data fusion opportunities, i.e. the number of potential acquisitions that can be obtained with this temporal characteristic. However, the required time interval between the two mixed acquisitions (from now on called *synchronicity time*) strongly depends on the final applications and the user's needs. Therefore, it needs to be further investigated in relation to the phenomena that are sensed. Furthermore, different constellation patterns and optimisation approaches can be addressed, as done in this work.

1.3. Thesis objective and original contributions

This thesis aims to explore the optimal design of a small satellites $(150 - 200\,\mathrm{kg})$ optical-SAR constellation. The constellation will be optimised for the regional coverage over Italy, and it will serve the main decision-makers involved in emergency response and critical infrastructure monitoring. Specifically, the emergency response related to floods and ice sleeve formation on overhead power lines will be investigated. The first part of the thesis will focus on identifying the main stakeholders involved during the emergency response in Italy and their main activities by analysing two case studies. In this way, it will be possible to identify their needs and derive requirements for the system.

Moreover, this thesis will study the specific problem of mixed sensor constellations optimisation. The proposed constellation aims to provide synchronous optical and SAR data, namely two mixed optical and SAR acquisitions within a short time interval, which could be beneficial for data fusion applications. Therefore, the performance of a synchronous optical-SAR constellation will be explored by introducing three new figures of merit that can give the designer a meaningful representation of the synchronous performance of the constellation. In particular, the synchronicity time will be introduced as a metric that determines the time interval between an optical and a SAR acquisition. Additionally, the synchronous revisit time will be presented to describe how often a target can be potentially sensed by the two sensors within a short time interval, and the synchronous daily coverage will be proposed as a metric that expresses the spatial extension of the territory of interest that the constellation can synchronously sense in a day. The optimisation will be performed without a fixed value of the synchronicity time but rather exploring a range between 1 and 15 minutes. This approach will enable the identification of the most optimal synchronicity time based on trade-offs between this variable and other system parameters, providing the designer with greater flexibility in designing the constellation. Furthermore, this element introduce a new and more flexible approach to optimizing mixed sensor constellations. The performance of the constellation will be evaluated by updating a code previously developed by Chiatante [47] and Sartoretto [48], introducing the computation of the new figures of merit of synchronicity time, synchronous revisit time and synchronous coverage. The synchronous revisit time will be evaluated starting from the definition of the data fusion opportunities introduced by Chiatante [47] and by computing the frequency of these opportunities. Instead, the synchronous coverage is evaluated thanks to the developement of a code module that provides the optical coverage, and then by integrating it with a SAR coverage module. Finally, the synchronicity time will become a new variable of the problem that has to be minimised instead of being a fixed value of 60 seconds as in the previous works.

Furthermore, some aspects related to the solution uncertainties will be explored, with the identification of the primary sources of uncertainty. The modelling tool will be validated through STK, and two different multi-objective optimisation algorithms will be tested and compared, namely a variation of NSGA-II included in MATLAB [49] and the MOEA/D [50].

A new optimisation approach will also be proposed. In previous work, Chiatante [47] employed a two-step methodology, initially performing optimisation of SAR constellation followed by adding the optical satellites in tandem. This approach aimed to identify the true anomaly shift that would maximise data fusion opportunities. In this work, the optical and SAR constellations will be optimised in a single step, enabling the exploration of new constellation patterns.

The optimisation tool provided in the thesis is proposed as an instrument that can be implemented during the preliminary phase of the space project. In particular, thanks to the optimisation tool, it is possible to develop some of the mission's preliminary technical requirements, starting from identifying the goals and needs of top-level customers and end-users. Specifically, the number of satellites and a rough launch cost can be developed, together with the orbital parameters of the satellites and the expected performance in terms of synchronous coverage and revisit. These elements can be used during feasibility studies of phase A as a starting point for more precise cost estimations and for the complete definition of possible system and operations concepts. However, in the successive phases of the design process, the support of more precise modelling tools should be considered to reduce the intrinsic uncertainties of this tool. Additionally, the computation of some figures of merit is excluded from the analysis, for example, the ground station visibility, data age, response time, and instrument duty cycle.

1.4. Thesis overview

The remainder of this thesis is organised as follows:

- Chapter 2 provides a comprehensive review of the relevant literature and theoretical frameworks related to constellation design and constellation mission analysis, SAR and optical systems, Earth observation, floods, critical infrastructure monitoring and multi-objective optimisation.
- In Chapter 3, some of the currently active optical and SAR satellite missions are reported and analysed.
- Chapter 4 presents two case studies that are relevant to the final application of the constellation. Specifically, the timelines of the 2017 Abruzzo snowfall and the 2022 Marche flood are described.
- In Chapter 5, some user and system requirements are provided after an operational analysis in Capella (open-source software for model-based systems engineering).
- The adopted methodology is provided in Chapter 6. The modelling tool for the coverage and revisit computation is described, along with the new figures of merit proposed for mixed sensor constellations. Finally, the problem's mathematical formulation is provided.
- In Chapter 7, the results obtained after the optimisation are presented, discussed and interpreted. Moreover, some optimal designs are selected, and their performances are further discussed.
- Chapter 8 provides a summary of the main findings of the study and their possible application, as well as recommendations for future research in this area.

2 | Literature review

2.1. Overview of satellite constellations

The development of a satellite constellation is a complex process involving several steps, namely the constellation design, the launch procedure, the build-up strategy, the maintenance strategy and the end-of-life procedure. The constellation design is the first important step of the mission analysis process, in which the orbital parameters of the satellites are defined as a function of the mission objectives, thanks to the employment of an optimisation algorithm. In order to express the system's performance, some performance indices (or figures of merit) are identified and employed as objectives to maximise. In addition, cost drivers, such as the number of satellites, are used as objectives to minimise. Therefore, optimisation methods are employed to identify a set of optimal constellation designs that maximise the performance at the minimum cost.

This section will give an overview of the most common figures of merit for Earth observation satellites, along with the main issues affecting the constellation design process, based on the literature review of Wertz [17], Huang [51], Chiatante [47], Sartoretto [48] and Sand [52].

2.1.1. Figures of merit for Earth observation constellation

In order to assess the performance of an Earth observation constellation, some figures of merit are commonly analysed during the design process. In particular, the two key performance indices which will be considered in the optimisation process of this work are the percentage coverage and the revisit time. In addition, the data age and the response time are other significant indices commonly employed for assessing the performance of Earth observation constellations. These parameters are usually computed over a territory of interest, which can be the entire globe or a more specific area. In this thesis, the territory of interest is the Italian surface that will be discretised in grid points representing a specific latitude and longitude. In this way, it is possible to evaluate the selected figures of merit on each grid point. It is worth mentioning that these metrics are traditionally defined for constellations adopting a single instrument. In the case of hybrid mixed sensor constellations, new indices should be defined to take into account the peculiarities of this typology of constellations. To fill this gap, the synchronous coverage and revisit time will be introduced and discussed in Section 6.3.

Percentage coverage

The percentage coverage is defined as the percentage of the territory of interest that can be sensed by the satellites in a given amount of time [47], [52]. It depends on many factors, such as the swath, the duty cycle of the instrument (i.e. the maximum time of continuous acquisition per orbit), the number of satellites, and the constellation scheduling [47]. For example, large monolithic satellites generally have a wider swath and a higher duty cycle than small satellites, so a constellation of large satellites can cover a larger portion of the Earth's surface with fewer satellites. Moreover, optical sensors are limited by illumination constraints and the presence of clouds, so even the working conditions influence their coverage [47]. In particular, coverage would be zero during the night or with the presence of clouds. On the contrary, SAR satellites can operate in any condition, providing coverage even at night and with clouds. In this work, the illumination constraint will be considered when assessing the coverage and revisit of optical satellites. On the contrary, clouds will not be modelled because their presence is difficult to predict. Coverage is also influenced by observation scheduling, which is usually optimised by the operator to exploit the available satellite resources in the most efficient way. However, coverage does not give information on the time gap between the observations, which needs to be investigated with the revisit time.

Revisit time

Revisit time is defined as the time elapsed between two consecutive observation opportunities [47], [52]. Therefore, during the simulation, a grid point is considered revisited whenever it is inside the access area of the instrument. In this way, it is possible to compute the minimum, the maximum and the average time gap between the revisits, which are called, respectively, minimum revisit time, maximum revisit time and average revisit time [52]. In this sense, revisit time is a metric that can be different for each grid point since it varies with the latitude and longitude of the target. However, in this work, the revisit time over the whole Italian surface needs to be evaluated. In this case, statistics among all the grid points can be computed, such as the minimum, the maximum, and the mean revisit time among all the grid points. Revisit time gives an important hint on the frequency of the observations that the system can provide. However, it is worth mentioning that in a real-case scenario, not every revisit opportunity can be exploited by the satellites to acquire data. In general, the acquisitions are limited by the duty cycle of the satellite, the storage capability and the scheduling of the observations. For this reason, the revisit time must be supported by percentage coverage to better understand the real fraction of territory that could be sensed in a certain amount of time. Revisit time, instead, depends only on the number of satellites, the constellation pattern and the instrument access angles. Therefore, a constellation composed of many small satellites outperforms large monolithic satellites in revisit time since the same area can be revisited by the frequent passage of the many satellites belonging to the constellation [47].

Data age

Data age measures the time elapsed between the measurement of a satellite and the delivery of the data to the user. It is a crucial parameter, particularly for emergency response, when rapid time-changing phenomena are involved, and it is essential to have up-to-date data for making accurate and informed decisions [47], [52]. In fact, if the delivered data are too old, there is a greater chance that the state of the emergency is not accurately described anymore. Data age is mainly influenced by the constellation orbital pattern and the downlink options, which depend on telecommunications technology and on the number and location of the ground stations [47].

Response time

The system response time refers to the time elapsed from a request to observe a specific location until we can observe it. Therefore, it is a measure that includes several steps [47], [52]

- managing the request;
- uplinking the command to the satellite;
- sensing the requested scene;
- downlinking the data to a ground station;
- delivering the product to the user.

It can be influenced by the number of satellites, the revisit time, the location and number of the ground stations and the employment of inter-satellite links. Moreover, it is also influenced by the data storage capacity since if the satellite storage is full, new requests cannot be handled [47].

2.1.2. Constellation design

Designing a satellite constellation is a complex task that involves several considerations [17], [48]. The designer's main aim is to find the most affordable constellation that fulfils the system specification. However, many variables influencing the design are involved, and no absolute rules exist. Therefore, the design process involves several trades based on cost vs performance considerations. The following are the primary factors that determine the system cost, performance, or both [17]:

- The *number of satellites* is one of the main cost drivers since it is usually proportional to the cost of the constellation. At the same time, it is the principal determinant of the coverage and the revisit time. Thus, a common goal in constellation design is to achieve the required performance with the minimum number of satellites. Although having fewer satellites in a constellation may reduce the cost, this is not always true. In fact, smaller constellations may require large and complex satellites with a wide swath, which are more expensive to produce. Additionally, since constellations with fewer satellites are often located at higher altitudes, the launch costs may also be greater.
- The *launch options* are another important cost driver. In particular, the number of launches that are required to deploy the full constellation has an essential impact on the price, as well as the launcher that is used. In general, small satellites that belong to the same plane are usually deployed in batches to reduce the required number of launches.
- The radiation *environment* has a strong impact on system cost. Satellites orbiting at higher altitudes are exposed to a higher level of radiation, which can limit the operative lifetime and require more complex and expensive systems.
- The orbit selection also affects the *perturbations* the satellites will face and thus the required delta-V for *station-keeping*. For example, altitude has an influence on the level of drag. Hence, satellites orbiting at the same altitude, inclination and eccentricity are usually used to maintain the constellation structure over time since all the satellites are affected by similar perturbative effects due to Earth's oblateness.
- During the design process, it is also crucial to consider collision avoidance, build-up and replenishment strategies, as well as end-of-life procedures.

In this thesis, the number of satellites and the launch cost required for the full constellation deployment will be selected as objectives to minimise. The other aspects are also considered during the design in order to guarantee the feasibility of the mission, particularly considering the employment of small satellites. However, the precise cost estimation will not be assessed in this preliminary analysis and needs to be investigated more thoroughly in more advanced phases of the project.

2.2. Specialised orbits

The state of a spacecraft can be uniquely identified by using six parameters, which can be defined by the components of the three-dimensional vectors of position, $\boldsymbol{r}$, and velocity, $\boldsymbol{v}$, or the classical Keplerian elements [51], [53]:

- the semi-major axis, a
- the eccentricity, e
- the inclination, i
- the Right Ascension of the Ascending Node (RAAN), Ω
- the argument of perigee, ω
- the true anomaly, θ

Orbit selection is one of the most complex tasks in mission design because many options need to be evaluated, and the orbit parameters have a heavy impact on a large number of requirements [54]. For example, the orbit altitude is one of the parameters which has the most remarkable impact on mission requirements: a higher orbit can provide better coverage, but it is more expensive to achieve, exposes the satellites to a more adverse radiation environment and worsen the spatial resolution of optical instruments. In this work, only Low Earth Orbits (LEO) are considered because they are more suitable for small satellites considering environmental constraints, limited available power, size of the instruments, resolution requirements of the sensors, and cheaper launch costs. Some consideration on the orbit parameters will be later used to derive constraints on the orbit parameters, defining the admissible domain in the decision space for the optimisation.

Additionally, the so-called specialised orbits are usually selected for the specific characteristics that make them particularly appropriate for specific applications. An overview of the most common specialised orbits can be found in the book of Wertz [54], namely Geosynchronous (GEO), Sun-Synchronous (SSO), Molniya, frozen, repeating ground track, and Repeat Coverage (RCO) orbits. The employment of specialised orbits is not mandatory, but they are commonly exploited for their beneficial characteristics. Therefore, Sun-synchronous and repeating ground track orbits will be considered in this work because of their advantages in remote sensing applications.

2.2.1. Repeating ground track orbits

Repeating ground tracks are orbits that retrace their ground track over a certain time interval [47], [53], making them particularly favourable in Earth observation for their consistent viewing angle at each passage and periodic revisits over the same location [53], [54]. They depend on the relationship between the nodal period, T_n, which is the time interval it takes the satellite to make two successive equator crossings, and the nodal period of Greenwich, T_{θ_G}. The nodal period, T_n, can be computed as [53]:

$$T_n = \frac{2\pi}{n + \dot{\omega} + \dot{M}_0} \tag{2.1}$$

where n is the mean motion, while $\dot{M}_0$ and $\dot{\omega}$ represent the mean anomaly's rate of change and the argument of perigee rotation rate due to the effects of the secular J_2 perturbation, respectively [47], [53]:

$$\begin{aligned} n &= \sqrt{\frac{\mu}{a^3}} \\ \dot{\omega} &= -\frac{3}{2}\frac{\sqrt{\mu} J_2 R_\oplus^2}{a^{7/2}(1-e^2)^2}\left(\frac{5}{2}\sin^2 i - 2\right) \\ \dot{M}_0 &= -\frac{3}{2}\frac{\sqrt{\mu} J_2 R_\oplus^2}{a^{7/2}(1-e^2)^{3/2}}\left(1 - \frac{3}{2}\sin^2 i\right) \end{aligned} \tag{2.2}$$

The nodal period of Greenwich, T_{θ_G}, is defined as the period of the Earth's rotation with respect to the ascending node [53]:

$$T_{\theta_G} = \frac{2\pi}{\omega_\oplus - \dot{\Omega}} \tag{2.3}$$

where $\omega_\oplus$ is the Earth's angular rate, and the nodal precession $\dot{\Omega}$ due to the secular J_2 effect is [47], [53]:

$$\dot{\Omega} = -\frac{3}{2}\frac{\sqrt{\mu} J_2 R_\oplus^2}{a^{7/2}(1-e^2)^2}\cos i \tag{2.4}$$

If an orbit repeats its ground track after k revolutions of the satellite and m rotations of the Earth, the ratio between the nodal period of Greenwich and the satellite nodal period is a rational number [47], [53]:

$$\frac{T_n}{T_{\theta_G}} = \frac{m}{k} = \frac{\omega_\oplus - \dot{\Omega}}{n + \dot{\omega} + \dot{M}_0} \tag{2.5}$$

The implicit equation in Equation (2.5) express a relationship between m, k, the inclination i, the eccentricity e, and the semi-major axis a. Once four of these five parameters are fixed, the fifth can be determined by numerically solving Equation (2.5). Moreover, the parameters m and k are usually selected to be coprime (i.e. without common factors) to avoid redundancy. In fact, what is relevant in Equation (2.5) is the ratio m/k. For example, the repeating ground with $m = 3$ and $k = 13$ is the same as that with $m = 6$ and $k = 26$, as they have the same ratio.

The main drawback of a repeating ground track orbit is that satellites experience Earth's geopotential perturbations in a periodic fashion, potentially causing resonance effects and magnifying the impact of perturbations [17], [54].

2.2.2. Sun-synchronous orbits

A Sun-synchronous orbit (SSO) is a type of orbit that maintains an approximately constant angle between the orbital plane and the Sun's direction. In fact, the Earth's oblateness causes the orbital plane to rotate in the inertial space at a rate that matches the mean Earth's rotation rate about the Sun. This property is particularly useful for optical satellites because it ensures that any location is sensed with consistent illumination conditions since the satellite will always pass over any given point on the Earth's surface at the same time of day [17], [54]. The constant illumination angle is also beneficial for the consistent exposure of solar panels to the Sun's rays. Moreover, some SSO, like dawn-dusk orbits, can minimise the number of eclipses. Many missions have exploited Sun-synchronous orbits to reduce battery size or eliminate a second gimbal in the solar array drive. However, this solution is generally not cost-effective since the launch cost of the Sun-synchronous orbit is approximately 30% higher than a less inclined orbit [54]. Nevertheless, because of their high inclination, SSOs tend to provide worse coverage at the Italian latitudes. In fact, coverage is usually maximised at latitudes that are near the orbit inclination [47], [55]. The strengths and weaknesses of Sun-synchronous orbits for SAR and optical satellites are summarised in Table 2.1.

Each Sun-synchronous orbit is characterised by a specific Local Time at Ascending Node (LTAN), which is the local mean time at which the spacecraft crosses the equator, and that remains constant over time.

In Sun-synchronous orbits, the nodal precession rate, $\dot{\Omega}_{SSO}$, is imposed to 360° in a sidereal year. Thus, manipulating Equation (2.4), it is possible to express the inclination

	SSO	Generally inclined
Coverage at mid-latitudes	Worse coverage at mid-latitudes because a higher amount of time is spent over the poles.	Good coverage at a latitude near the orbit inclination [47], [55].
Duty cycle (SAR)	Consistent exposure of solar panels to the Sun's rays. Among all the possible Sun-synchronous orbits, dawn-dusk orbits are usually used to minimise the number of eclipses. Thus smaller solar arrays and batteries are required, or a longer duty cycle can be achieved.	Solar panels may require additional degrees of freedom since the position of the Sun relative to the orbit plane is variable. Larger solar arrays and batteries are required, or the duty cycle is shorter.
Illumination conditions (Optical)	Illumination is consistent over time, facilitating comparisons between acquisitions taken at different times (useful, for example, when long-term variations need to be monitored). 8.30-11.00 and 13.00-15.30 orbits are usually used by optical satellites for their optimal illumination conditions.	Illumination conditions are not consistent over time
Launch cost	Higher	Lower

Table 2.1: Sun-synchronous orbits strengths and weakness.

as a function of the eccentricity and the semi-major axis:

$$i = \cos\left(-\frac{2\dot{\Omega}_{SSO}a^{7/2}(1-e^2)^2}{3R_{\oplus}^2 J_2\sqrt{\mu}}\right) \tag{2.6}$$

2.3. Walker constellations

Mission analysis for satellite constellations is more complex than a single satellite mission since each of the T satellites belonging to the constellation has a different orbit. Therefore, in theory, the number of parameters that need to be defined is $6T$, i.e. six Keplerian elements (or position and velocity components) times T satellites. To simplify the design, symmetric orbital patterns that reduce the decision space are usually adopted, such as Walker constellation [21], [23], which relies only on four parameters (in the notation proposed by Walker $[i\!: T/P/F]$), plus the semi-major axis. Each satellite in the constellation has a circular orbit with the same inclination and altitude. Thanks to these characteristics, each satellite is subject approximately to similar perturbations, and thus the constellation structure remains constant in time without additional station-keeping manoeuvres.

The four parameters defining a Walker pattern are [47], [56]:

- i = the inclination;
- T = the total number of satellites in the constellation;
- P = the number of planes;
- F = the relative phasing parameter.

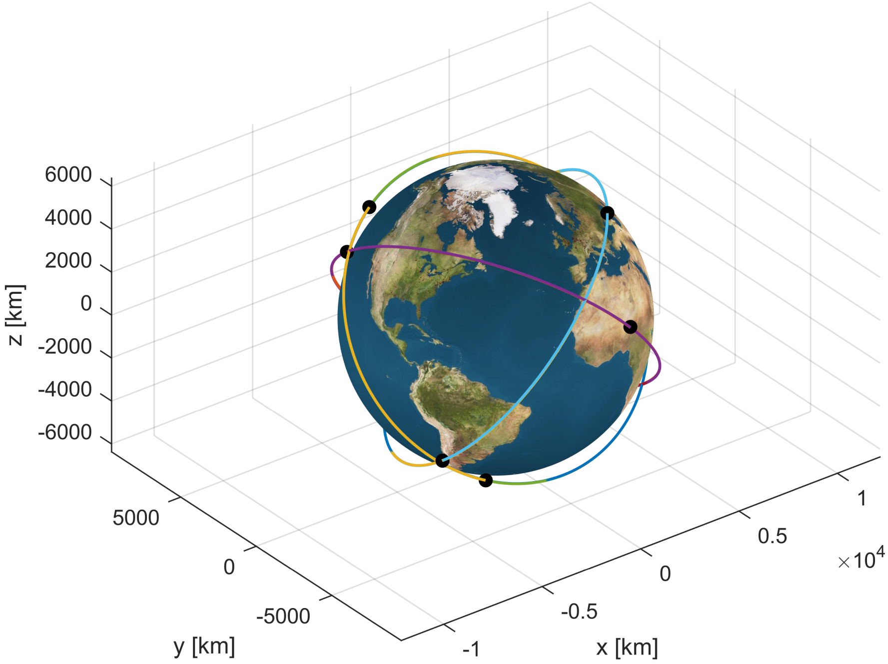

Figure 2.1: Walker Delta constellation, [50 deg: 9/3/1]

The T satellites are equally divided among the P planes, and each plane contains $S = T/P$ satellites evenly spaced in true anomaly by a value equal to $\Delta\theta = 360^\circ\, P/T$, or $\Delta\theta = 2\pi\, P/T$. The right ascension of the ascending node of the j-th orbit plane is

$\Omega_j = W\frac{2\pi j}{P}$, with $W = 1$ for Walker Delta pattern and $W < 1$ for Walker Star pattern, and $j = 1, \ldots, P$. The phasing parameter $F \in [0,\ P-1]$ is an integer number that determines the relative phasing between satellites in adjacent orbit planes: $\Delta\Phi = F\,(360°/T)$. An example of Walker constellation is given in Figure 2.1.

2.4. Remote sensing and Earth observation

Remote sensing is the measurement of the physical characteristics of an object without physical contact. The two main components of a remote sensing system are an illumination source that emits radiant energy and a recording sensor that collects it. The main difference between optical and SAR instruments is that while the first requires an external energy source (i.e. usually the Sun or a thermal energy source), the second one provides its own illumination source. Therefore, SAR sensors can operate in any illumination condition, even at night, while optical sensors not. For this reason, SAR instruments are called active sensors, while optical systems are passive sensors. Moreover, one of the most limiting aspects of optical sensors is that they cannot penetrate clouds, in contrast to SAR. In order to characterise the physical properties of the scene, the instrument measures how the target objects (vegetation, water bodies, buildings...) interact with the received radiation that can be absorbed, emitted, reflected or scattered. Furthermore, radiation can also interact with the atmosphere, which usually is an unwanted effect in Earth's observation application, but becomes desired if atmospheric properties need to be evaluated.

2.4.1. Synthetic Aperture Radar (SAR)

The origin of RAdio Detection And Ranging (RADAR) dates back to the turn of the 20^{th}, but it was only in the 1950s that the first imaging radar, capable of providing two-dimensional representations of the scene, was invented [57], [58]. Such an instrument was the so-called Side Looking Airborne Radar (SLAR) or Real Aperture Radar (RAR), in which the antenna is mounted laterally on a moving aircraft. Its ability to acquire images in the dark and through clouds made this technology very attractive. However, its main weakness is the limited resolution, which depends on the distance between the sensor and the ground, and the antenna aperture. This limitation makes SLAR impractical for space applications since it would require a huge antenna to achieve acceptable resolution. For example, a 480 m long antenna would be necessary to achieve a 50 m resolution from an X-band SLAR operated at 800 km altitude. An important invention in 1951 was the technique of "Doppler beam sharpening" by Carl Wiley of the Goodyear Aircraft

Corporation that made it possible to overcome this limitation, allowing the realisation of the first Synthetic Aperture Radar (SAR), which is a technological evolution of SLAR [58]. SAR is a high-resolution imaging radar that must be operated from a moving platform (typically an aircraft or a satellite) to simulate or “synthesise” a virtual aperture much larger than the physical antenna length. For this reason, SAR instruments can achieve a much better resolution compared to SLAR. A complete overview of SAR technology can be found in the book by Woodhouse [59] and in Moreira et al. [58], and some aspects will be summarised in this section.

Radars operate typically in the microwave region defined as the 0.3 - 300 GHz frequency range, but not all frequencies are available for radar systems. In particular, SAR sensors can transmit energy in one of the microwave bands shown in Table 2.2. SAR orbiting systems mainly use three frequency bands, that is the X-band (3 cm), the C-band (5 cm), and the L-band (24 cm), while the first P-band (30-100 cm) SAR sensor in orbit is planned for launch in August 2024, mounted on the Biomass satellite [60]–[62]. On the contrary, Ka- and Ku-band bands have only been used in experimental airborne SAR systems [57].

Band	Wavelength [cm]	Frequency [GHz]
Ka	1.1 - 0.8	27 - 40
K	1.7 - 1.1	18 - 27
Ku	2.4 - 1.7	12 - 18
X	3.8 - 2.4	8 - 12
C	7.5 - 3.8	4 - 8
S	15 - 7.5	2 - 4
L	30 - 15	1 - 2
P	100 - 30	0.3 - 1

Table 2.2: Designation of microwave bands.

The wavelength has an important role related to the penetration capabilities of the transmitted microwave signal, such that longer wavelength signals (e.g. L-band) have a higher penetration depth, making them particularly suitable for biomass and vegetation mapping, thanks to the possibility to penetrate deeper into vegetation canopies. On the contrary, X-band can achieve higher resolutions and smaller antennas, but it is rarely used for characterising biomass, and it cannot map activities underneath canopies.

SAR typically has a rectangular antenna of physical length l and width W that is mounted

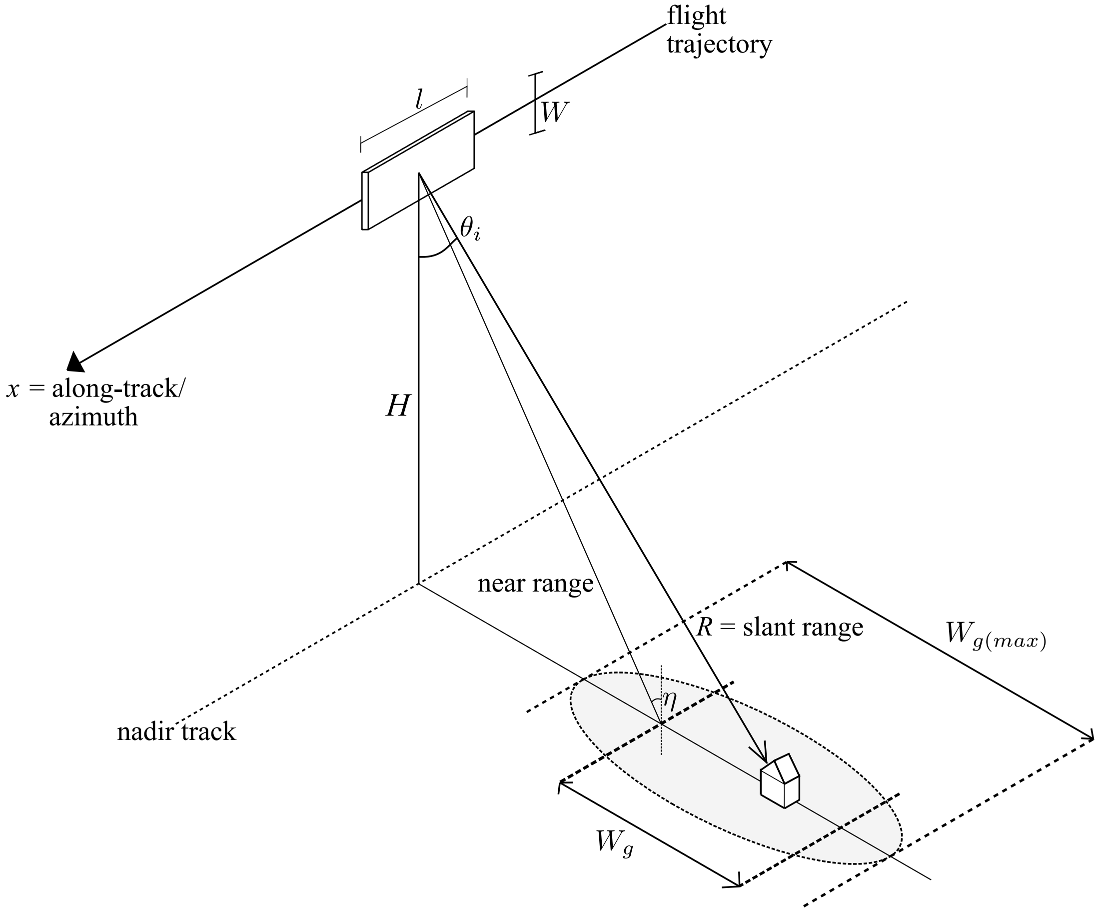

Figure 2.2: Stripmap SAR imaging geometry.

on a moving platform. The antenna is pointed laterally to the left or right side with respect to the along-track direction, as illustrated in Figure 2.2. A SAR is a pulsed radar that alternately transmits a pulse and receives echoes while it moves along its trajectory, and therefore it is capable of generating two-dimensional images in which the two coordinates are range, R, and azimuth (along-track), x. In particular, the time delay between the transmission and the reception of the pulse is proportional to the distance R between the target and the radar. Two of the most important performance parameters of a SAR system are the range resolution (Rg.) and the azimuth resolution (Az.). Range resolution is defined as the minimum distance in range between two targets that the radar system can separately detect, and it is computed as [59]:

$$\rho_r = \frac{c\tau_p}{2} \tag{2.7}$$

in which τ_p is the time duration of the pulses transmitted by the system, and c is the speed of light. However, in order to improve this resolution, many radar systems make use of a linear *frequency modulated* (FM) or *chirped* pulse of bandwidth B_p, such that the resulting resolution becomes [59]:

$$\rho_r = \frac{c}{2B_p} \tag{2.8}$$

The ground range resolution ρ_g, which describes the ability to discriminate objects that are situated on the ground, is calculated from ρ_r, projecting the range onto Earth's surface via the local incidence angle θ_i:

$$\rho_g = \frac{\rho_r}{\sin\theta_i} \tag{2.9}$$

thus, if the incidence angle increases, ground range resolution improves.

Similarly, the azimuth resolution ρ_a is defined as the smallest separation between two point targets that the radar can detect in the along-track direction, and it is computed as [59]:

$$\rho_a \geq \frac{v}{B_D} = \frac{l}{2} \tag{2.10}$$

where l is the antenna length and B_D is the Doppler bandwidth. The fact that azimuth and range resolution do not depend on the distance from the target could seem surprising. However, distance still has an important role in power requirement analysis since it affects the Signal-to-Noise Ratio (SNR), so a higher distance from the target implies a higher power required.

The illuminated swath width on the ground, $W_{g(max)}$, depends on the wavelength, λ, and it can be determined by the expression of the 3-dB beamwidth of the antenna in the elevation plane, projected onto the ground [63]:

$$W_{g(max)} \approx \frac{\lambda R}{W\cos\theta_i} \tag{2.11}$$

SAR antenna design is complicated by the need to consider ambiguous returns in both the azimuth and range dimensions [63]–[65]. In fact, in order to avoid ambiguous return in range, the width of the desired ground swath W_g is bounded by [63]:

$$W_g < \frac{c}{2PRF\sin\theta_i} \tag{2.12}$$

where the Pulse Repetition Frequency (PRF) is the number of pulses per second emitted by the radar, and c is the speed of light.

Similarly, in order to avoid ambiguities in the azimuth direction, a lower bound on the

PRF is given by [63]:

$$PRF > \frac{v}{\rho_a} \tag{2.13}$$

in which v is the platform velocity in the along-track direction.

Therefore, combining Equations (2.12) and (2.13), it is possible to obtain the constraint [63]:

$$W_g < \frac{c}{2PRF \sin\theta_i} < \frac{c}{2v \sin\theta_i}\rho_a \tag{2.14}$$

that can be rearranged as follows [63]:

$$\frac{W_g}{\rho_a} < \frac{c}{2v \sin\theta_i} \tag{2.15}$$

which underlines how a large swath is at odds with a good azimuth resolution.

Moreover, if the best possible resolution and the widest possible swath are required, a constraint on the minimum area of the SAR antenna can be derived by combining Equations (2.10), (2.11) and (2.15) [63]:

$$A_{SAR}^{min} = 4\frac{v\lambda \tan\theta_i R}{c} \tag{2.16}$$

This last constraint shall only be respected if both the best possible resolution and the widest possible swath are needed simultaneously. Therefore, a smaller area is actually allowed (at the cost of a smaller swath and/or worse resolution).

The equations reported in the discussion are valid only for a SAR instrument operating in Stripmap mode. However, SAR systems can operate in three main imaging modes obtained by controlling the antenna radiation pattern:

- *Stripmap* mode: the look angle remains constant, and the instrument images a single continuous strip on the ground.
- *ScanSAR* mode: a sequence of pulses, called burst, are transmitted, illuminating several sub-swath that are obtained electronically steering the antenna beam. This technique allows obtaining a wider swath than Stripmap. However, azimuth resolution is reduced, as each sub-swath is illuminated for a shorter time than in Stripmap mode, and the synthesised aperture is smaller.
- *Spotlight*: the antenna is steered in the along-track direction toward a fixed target on the ground that is illuminated for a longer time, increasing the synthetic aperture length. In this case, a small area on the ground is sensed, but the azimuth resolution

is improved.

SAR interferometry

Differential synthetic aperture radar interferometry (DInSAR) is a radar technique that allows measuring small displacements at a wavelength scale. It is used for a variety of applications, such as measuring glacial motion and deformation, monitoring infrastructure and buildings, and measuring tectonic deformations after an earthquake or small deformations due to ground subsidence [58]. The technique exploits the phase of a SAR image, which is related to the one-way distance (or slant range R) of the point on the ground that is illuminated by the radar. If two acquisitions are made from slightly different satellite geometries, as shown in Figure 2.3, it is possible to compute the phase difference between the two acquisitions, ϕ_{int}, which is the interferometric phase [58]:

$$\phi_{\text{int}} = \phi_{\text{flat}} + \phi_{\text{topo}} + \phi_{\text{defo}} + \phi_{\text{atm}} + \phi_{\text{decorrelation}} \tag{2.17}$$

where ϕ_{flat} and ϕ_{topo} are geometric terms that can be removed based on an Earth ellipsoid model and a Digital Elevation Model (DEM). The last two contributions are related to atmospheric delay and speckle. The phase contribution related to the displacement is ϕ_{defo}, which can be expressed as [58]:

$$\phi_{\text{defo}} = \frac{4\pi}{\lambda} \Delta r_{\text{defo}} \tag{2.18}$$

where Δr_{defo} is the displacement projected onto the line of sight. It can be noted from Equation (2.18) how the phase difference is highly sensitive to the displacement, such that a displacement of $\lambda/2$ would produce a phase difference of 2π. A limitation of this technique is that the interferogram phase can only assume values between $-\pi$ and π radians, so unwrapping techniques are needed to measure deformation causing a phase difference higher than 2π.

The incoherent phase contribution, $\phi_{\text{decorrelation}}$, due to speckle can sometimes be predominant, so it is important to select pixels with good coherence to obtain accurate measurements. The Permanent Scatterer (PS) technique [66] is often used to avoid this problem, which exploits pixels that show a stable amplitude behaviour over time, usually corresponding to point-like targets such as buildings or rocks. One of the sources of decorrelation is called geometrical decorrelation, generated by the fact that the two acquisitions are made with different viewing geometry. This unwanted contribution increases if the normal baseline to the line of sight $B_\perp$ increases. The two SAR images become completely

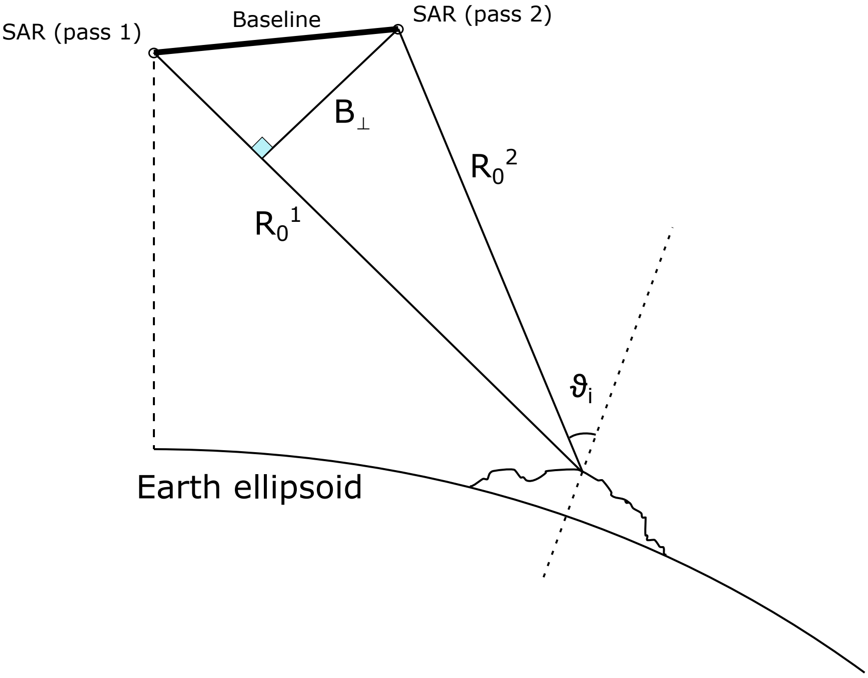

Figure 2.3: Imaging geometry of Differential synthetic aperture radar interferometry (DInSAR).

uncorrelated when the critical baseline, $B_{\perp,\,\mathrm{crit}}$, is reached [58]:

$$B_{\perp,\,\mathrm{crit}} = \frac{\lambda\, R_0}{2\rho_r}\tan(\theta_i) \tag{2.19}$$

where λ is the wavelength of the radar, ρ_r is the radar range resolution, and θ_i is the incidence angle of the radar beam.

2.4.2. Optical instruments

Optical instruments are passive systems that receive and collect a photon flux generated by a target on the ground that reflects the radiation emitted by the Sun or emits energy itself. Additionally, the atmosphere can also absorb or backscatter some photons, acting as a filter that attenuates the radiation at some specific bands. The photon flux is collected using optical elements such as lenses and mirrors; then, it is spectrally separated to isolate the useful wavelengths and, at last, transferred to detectors which convert the photons into an electronic signal, i.e. either a current or a voltage. The spectral separation stage is generally obtained thanks to a filter, a disperser (like a prism or a grating) or an interferometer [67]. Optical instruments operate in specific bands of the spectrum that range from the ultraviolet (0.1 µm) to the infrared (30 µm). Nevertheless, the bands most commonly used are those within the visible spectrum (VIS, 0.4-0.7 µm), near-infrared (NIR, 0.7-1.0 µm), and short-wavelength infrared (SWIR, 1.0-3.0 µm).

The spatial resolution of a remote sensing optical system is evaluated through the Ground Sampling Distance (GSD), which expresses the distance between pixel centres measured on the ground. For example, a $GSD = 1\,\mathrm{m}$ implies that each pixel corresponds to a 1x1 m square on the ground. The GSD of an image is determined by the pixel size of the detector, dp, the focal length, F, and the distance from the target, H [68]:

$$\frac{GSD}{H} = \frac{dp}{F} \tag{2.20}$$

The focal length, F_l, also influences the instrument's Field Of View (FOV), and they are related through the equation [69]:

$$FOV = 2\arctan\left(\frac{L_{det}}{2F_l}\right) \tag{2.21}$$

where L_{det} is the size of the detector. Therefore, a good spatial resolution (i.e., a small GSD) may require a large focal length, but this will result in a narrow FOV.

Furthermore, sensors can be classified based on their spectral range and the number of spectral bands in which they can measure electromagnetic radiation.

Therefore, panchromatic sensors are able to capture black and white images in a single band, typically in the visible and near-infrared (VNIR) portion of the electromagnetic spectrum. Instead, multispectral sensors can capture images in several different spectral bands, typically employing 3 to 10 bands. Lastly, hyperspectral sensors can capture detailed spectral information about the materials present in the scene thanks to their ability to measure electromagnetic radiation in hundreds or thousands of narrow bands. However, only some wavelengths can be practically adopted, as some of them are blocked by the atmosphere, which acts as a filter for electromagnetic radiation. Indeed, the atmosphere has its own transmittance, indicating the fraction of radiation that can be transmitted through it. As an example, the transmittance of the standard atmosphere in the VNIR and SWIR spectrum obtained by the LibRadtran software is shown in Figure 2.4.

A key parameter of an optical imaging system is the Signal-to-Noise ratio (SNR), which measures the level of a desired signal compared to the level of background noise. Consequently, images with high SNR are more desirable to derive accurate information [67]. SNR depends on many factors, but mainly on spatial resolution (i.e. GSD), satellite altitude, the efficiency of detectors, and the Sun's irradiance at ground level. This last element has a strong impact and mostly depends on the atmospheric composition, target reflectance, and acquisition geometry. It can be determined through radiative transfer models implemented in software such as MODTRAN or LibRadtran. An important geometrical parameter influencing the Sun's irradiance is the Solar Zenith Angle (SZA), which is the angle between the zenith and the centre of the Sun's disk, as illustrated in Figure 2.5. In fact, if the Sun is too low on the scene, the signal will be weak, and the scene will appear dark. On the contrary, the sensor could saturate if the Sun is near the zenith and the scene too bright. Typical values of SZA can range from 10° to 80°, which will be considered as a constraint when the optical satellite coverage and revisit are evaluated in the modelling software of this work.

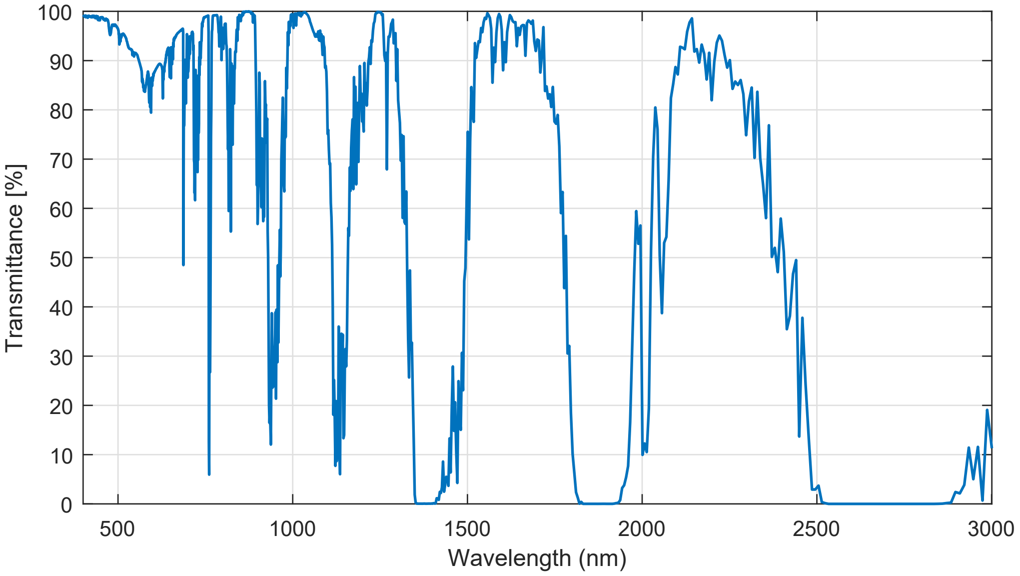

Figure 2.4: Atmospheric transmittance in the visible, near-infrared and short-wavelength infrared spectrum obtained by LibRadtran.

Optical satellites typically operate in pushbroom mode, meaning that they continuously acquire a strip on the ground with a fixed incidence angle [67].

2.5. Floods phenomena overview

Floods consist of the temporary overflow of water in areas in which normally there is no water [70]. They can be caused by the overflow of water bodies such as rivers, streams, canals, lakes and, for coastal areas, by the sea. Floods originate mainly from heavy rainfalls, but they can also occur as a consequence of the breakdown of hydraulic works such as dams or embankments. Floods can have catastrophic effects, causing loss of human

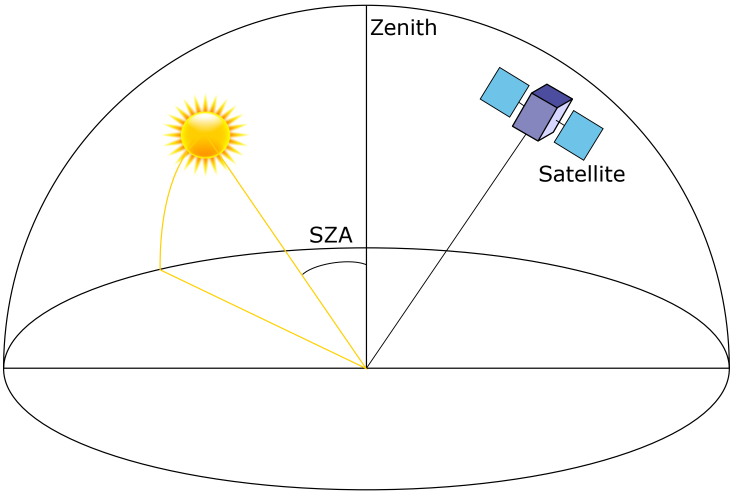

Figure 2.5: Optical satellite imaging geometry.

life and damage to infrastructure and buildings. According to the World Meteorological Organization (WMO) [71], from 1970 to 2019, floods accounted for 44% of all natural disasters. These floods caused 16% of deaths due to natural hazards and 31% of economic losses. Moreover, climate changes are also causing an increase in the frequency of intense rainfall events and, consequently, an increase in the frequency of flash floods [72].

According to ISPRA (Institute for Environmental Protection and Research) [73], the Italian territory is particularly exposed to flood risk. In fact, the total Italian area with high flood probability cover 16 223.9 km^2 (5.4% of the national territory), with medium flood probability 30 195.6 km^2 (10.0% of the national territory), and low hazard areas 42 375.7 km^2 (14.0% of the national territory), with 6.8 million inhabitants exposed to flood risk.

Flood risk is driven by many factors, both natural and anthropic [70]. Indeed, many natural factors can give rise to fast and catastrophic phenomena, for example, exposure to intense meteorological phenomena combined with geological and geomorphological conformation (e.g. small hydrographic basins, which have extremely rapid response time-lapses to precipitations). In addition, the hydrogeological risk is influenced by anthropic elements, like population growth, urbanisation, unauthorised construction in hazardous areas, deforestation, the use of agricultural techniques that are not environmentally friendly, and lack of maintenance of waterways.

Earth observation technologies can be effectively employed in flood emergency response to quickly assess flood damage, identify flooded areas, and prioritise response efforts. However, timely observations are needed for a fast response and effectively save lives.

2.5.1. Optical and SAR remote sensing for flood emergency management

Satellites can effectively be exploited for every phase of flood management, including mitigation and preparedness (before the flood), rescue and relief (during the flood), and recovery (after the flood) [74]. For example, meteorological satellites play a crucial role in flood preparedness by providing early warnings through continuous weather monitoring. On the other hand, communication satellites can be useful in rescue and relief efforts during floods by enabling satellite communication in otherwise inaccessible areas.

Even optical and SAR sensors can have an important role. Near-infrared sensors are particularly effective in detecting floods because the near-infrared spectral bands are strongly absorbed by water but reflected by land. High-resolution imagery is also used to determine the detailed damage to houses, roads, levees, and other structures and help during the post-disaster assessment, thanks to change detection techniques [74], [75]. However, despite the numerous applications of optical sensors in flood management, they often face challenges due to high probabilities of cloud coverage during or after a flood event. These challenges make it difficult for optical sensors to capture clear images of the ground, making them unsuitable for mapping and monitoring floods in most cases. In order to overcome these limitations, microwave SAR sensors are preferred as they are able to penetrate clouds and effectively capture images in adverse weather conditions. Additionally, water is easily detectable in SAR images since it appears dark due to its smooth surface, which causes low backscatter, while the surrounding terrain appears bright due to its rough surface. Moreover, SAR data can be used to obtain DEMs that represent the topography of the region and can be used to simulate and predict the movement of water and the spread of flood thanks to hydrological models [75]. In this way, it is also possible to locate vulnerable areas and produce risk maps. Both optical and SAR images have also been combined with DEM to produce flood depth and flood extent maps [74]. These maps can be particularly useful during the emergency response phase, giving important information about the situation and helping decision-makers to prioritise response efforts to the most affected areas. Furthermore, data fusion for surface water detection has been found to reduce uncertainty compared to single-polarisation SAR [76].

2.6. Critical infrastructures

Critical infrastructures are organisational and physical structures and facilities of such paramount importance to a nation's society and economy that their failure or deterioration would result in grave consequences [77]. An example of critical infrastructures are facilities related to electricity generation, transmission and distribution. In fact, the increasing dependence on electricity for electronic devices, industrial production, and daily life makes modern society more vulnerable to power outages. Therefore, a blackout can significantly impact our daily life and the economy, especially if it has a long duration. After a power outage, other critical infrastructure such as communication and transportation may be impaired, heating and water supply may be disrupted, and production and trade may be halted. Furthermore, emergency services like fire, police, and ambulances may be unable to function due to the failure of telecommunication systems. Hospitals may only be able to operate as long as their emergency power supply is adequately fuelled. Financial trading, cash machines, and supermarkets may also be forced to close.

The resilience of critical infrastructures is crucial for the well-being of our modern society and for reducing potential economic losses due to their damage. EO data can be essential in monitoring different kinds of infrastructures, helping the operators to quickly detect and respond to environmental hazards; in particular, the problem of power grid monitoring will be investigated in more detail in this thesis.

2.6.1. Blackouts and ice sleeves

The electric power industry is particularly vulnerable to natural disasters and other environmental factors. This is especially due to the large spatial extent of power infrastructure facilities, such as long-distance overhead power transmission lines, which are often located in areas prone to natural risks. For instance, the Italian territory has about 22 000 km of very high-voltage power lines, 46 000 km of high-voltage, 350 000 km of medium-voltage, and 780 000 km of low-voltage [78]. Strong wind, storms, lightning, wildfires, falling trees, heavy snowfall, heavy rain, wet snow, and icing have been identified as the main natural factors that have the potential to cause significant damage to power lines [79]. Among these risks, icing on power lines is a recurring problem in Italy, causing failures on high- and medium-voltage power lines during the cold season. Indeed, every year in Italy, the estimated cost of damages from these snowstorms is greater than 200 million euros [80], [81].

Icing accretion is caused by three typologies of phenomena, namely wet snow, glaze, and hard rime. However, only the first kind strongly influences power lines in Italy. Wet snow typically forms when the ambient temperature is between -0.5 °C and 2.0 °C. If a minimum of 10 mm of precipitation falls under this condition, ice can accumulate on the conductor, forming a so-called ice sleeve. This type of ice is characterised by a high density, which can reach up to 850 $\mathrm{kg\,m^{-3}}$ [82]. Wet snow events typically last for 18-24 hours and can produce snow sleeves up to 15 cm in diameter. This can result in an additional load on conductors of up to 8-10 kg/m, which can cause serious damage to overhead lines. In some cases, the conductor can also undergo an extra load due to the intense wind [81].

Several defence techniques are available for avoiding or mitigating the effect of wet snow. A possible solution tested by TERNA (the Italian Transmission System Operator) is a passive system consisting of counterweights that increase the torsional stiffness of conductors [80], [81] and prevent the formation of ice sleeves. Szabó et al. [82] proposed a method based on meteorological models called Dynamic Line Rating (DLR), that can predict the anti-icing current needed to heat the conductor up to a temperature that prevents the formation of ice sleeves. Other defence strategies based on power dispatching can be implemented to minimise supply failures. However, to effectively implement this strategy, it is necessary to have a good prediction of icing phenomena a few days in advance of the event. A forecast system for the Italian territory was developed by RSE S.p.A. The system is named W.O.L.F. (Wet snow Overload aLert and Forecast) and is available online at `http://newwolf.rse-web.it/`. It combines a meteorological model and an ice accretion model to forecast the maximum load of ice sleeves and their hazard on the Italian territory up to 72 hours in advance. The hazard level is reported in a WebGIS interface, with a spatial resolution of 5 km. In addition, anti-icing currents to prevent snow formation on power lines are predicted. This system has proven to be effective in predicting many hazardous events but presents some inevitable uncertainties related to the adopted forecast models [80], [81]. Therefore, the false alarm rate may be high, or some events may not be predicted. Additionally, the low spatial resolution of 5 km makes this tool particularly limited. Therefore, EO data could be used to monitor power lines during a wet snow event in order to distinguish false alarms and detect the formation of ice sleeves more precisely. In this way, the W.O.L.F. system will serve just as an early warning tool. A more detailed description of the W.O.L.F. system can be found in Bonelli et al. [80], and Lacavalla et al. [81].

2.6.2. Optical and SAR remote sensing for overhead power line monitoring

Due to electricity's significance in our modern society, effective monitoring and maintenance of power lines are of utmost importance. Traditionally, these power lines are surveyed through field surveys (on foot) or aerial surveys (from helicopters). However, as the power line network spans over large areas, various remote sensing techniques have been proposed for this purpose [83]. In a review by Matikainen et al. [83], different remote sensing technologies that can be effectively adopted for power line corridor surveys were discussed, including SAR images and optical satellite, but also aerial images, thermal images, airborne laser scanner data, land-based mobile mapping data, and UAV data.

SAR images have been used to indirectly monitor the security of infrastructures by detecting mine subsidence and landslides using DInSAR and PS interferometry [84], [85]. Jingnan [86] examined the scattering characteristics of transmission towers and determined that it is possible to monitor deformation changes caused by ice buildup using high-resolution SAR images. The field of power line monitoring has also seen many patent applications [83]. For example, Soli and Calabrese [87] patented a SAR-based monitoring method that uses electromagnetic mirrors to monitor partially visible or non-visible targets. This method can be applied to monitor buildings and infrastructures and to see conductors of overhead power lines, which often have a small radius and are challenging to detect.

Optical satellite images have been widely used for monitoring vegetation near power line corridors. Indeed, multispectral satellite stereo images can be employed to identify hazardous vegetation that may come into contact with the lines and cause flashovers [83]. Ahmad et al. [88] investigated vegetation encroachment and discussed how multispectral satellite stereo images could be used to create a 3D DEM of transmission line corridors to identify vegetation that poses a threat to power lines and can result in blackouts.

2.7. Multi-objective optimisation

Constellation design is often formalised as a Multi-Objective Optimisation Problem (MOOP) since the designer's main goal is to identify an optimum orbital pattern that can minimise cost and maximise performance. Costs and performances are mathematically expressed by means of two or more *objective functions* that should be minimised (or maximised) at the same time. For instance, in this work, the cost of the constellation will be expressed by the total number of satellites and the launch cost. In contrast, the performance will be expressed by the synchronous revisit time, synchronous daily coverage and synchronicity time of the hybrid optical-SAR constellation. Since these objectives are in contrast, it is not possible to obtain a single solution that minimises the cost and maximises the performance at the same time, so a set of compromise solutions is found, i.e. the so-called Pareto set. Several reviews have been written about the fundamental theory of multi-objective optimisation. However, the literature review of this chapter used as references the books of Burke et al. [89], Martì et al. [90], and Vasile et al. [91].

In a MOOP, each objective function f_i can be collected in the objective function vector:

$$\mathbf{F}(\boldsymbol{x}) = [f_1(\boldsymbol{x}),\, f_2(\boldsymbol{x}),\, \ldots,\, f_k(\boldsymbol{x})] \tag{2.22}$$

in which k is the number of objective functions $f_i : Q \rightarrow \mathbb{R}$, and $\boldsymbol{x} = [x_1,\, x_2,\, \ldots,\, x_n]^T$ is the vector of the decision variables. The set $Q \subset \mathbb{R}^n$ is the domain of $\mathbf{F}$, also called parameter space or decision space. Moreover, the decision variables may be subjected to m inequality, and p equality constraints:

$$g_i(\boldsymbol{x}) \leq 0 \quad i = 1, 2, \ldots, m \tag{2.23}$$

$$h_i(\boldsymbol{x}) = 0 \quad i = 1, 2, \ldots, p \tag{2.24}$$

Furthermore, upper and lower boundaries are set to the decision variables:

$$x_i^{(L)} \leq x_i \leq x_i^{(U)}, \qquad i = 1, 2, \ldots, n. \tag{2.25}$$

2.7.1. Pareto optimality

Since the objective functions are often in conflict, usually, there is not a single point that optimises all the objective functions at the same time, so a set of trade-off solutions should be found. Indeed, in this kind of problem, we look to a set of feasible solutions $\boldsymbol{x}^*$ that are said to be *Pareto optimal*. The idea of Pareto optimality is based on the principle of domination. Mathematically, the vector $\boldsymbol{x}^* \in Q$ is said to dominate another solution $\boldsymbol{x} \in Q$ if [92]:

$$\begin{aligned} &\forall i \in \{1, 2, ..., k\},\ f_i(\boldsymbol{x}) \leq f_i(\boldsymbol{x}^*),\ \text{and} \\ &\exists i \in \{1, 2, ..., k\},\ f_i(\boldsymbol{x}) < f_i(\boldsymbol{x}^*). \end{aligned} \tag{2.26}$$

Then, a solution $\boldsymbol{x}^*$ is said to be Pareto optimal if there does not exist another solution $\boldsymbol{x}$ that dominates it. That is to say, there exists no feasible vector of decision variables that would improve at least one objective function without degrading another one. The set of Pareto optimal points is called the Pareto front, Pareto frontier, or Pareto boundary. Note that the definition in Equation (2.26) is valid if the objectives shall be minimised. If some objective functions must be maximised, the equation's sign must be modified accordingly.

2.7.2. Possible approaches to multi-objective optimisation

Even if in a MOOP there are many optimal trade-off solutions, from a practical viewpoint, the designer can realise only one of them. For this reason, after the optimisation process, only one solution should be selected, often using higher-level information about the problem to express preferences among the objectives. However, an alternative approach called *preference-based* procedure can be used. In this case, a composite objective function is formed as the weighted sum of the objectives, transforming the multi-objective optimisation problem into a single-objective one. After that, classical single-objective optimisation methods can be used to find a single optimum solution belonging to the Pareto-optimal set. Both approaches usually need high-level information about the problem that is often non-technical, qualitative, and experience-driven [89]. However, when a *preference-based* procedure is followed, high-level information must be used a priori to form a weights vector, and the optimisation outcome is highly sensitive to this choice and not easy to predict. On the contrary, with the first approach, this information is used only at the end of the optimisation to select one of the solutions.

2.7.3. Classical methods: weighted sum approach

With this method, the set of objective functions is transformed into a single objective by pre-multiplying each objective with a user-supplied weight. With this method, the problem assumes the form [89]:

$$\begin{cases} \text{Minimise:} & F(\boldsymbol{x}) = \sum_{i=1}^{k} w_i f_i(\boldsymbol{x}) & \\ \text{Subjected to:} & g_i(\boldsymbol{x}) \leq 0, & i = 1, 2, \ldots, m \\ & h_i(\boldsymbol{x}) = 0, & i = 1, 2, \ldots, p \\ & x_i^{(L)} \leq x_i \leq x_i^{(U)}, & i = 1, 2, \ldots, n. \end{cases} \tag{2.27}$$

in which w_i are weights used to convert the problem to a single-objective one. This method is one of the simplest approaches, but it is not always easy to define the weights w_i a priori. An additional limit is that this procedure cannot be used to find Pareto-optimal solutions lying on the non-convex portion of the Pareto-optimal front. Because of these limitations, this method will not be adopted in this work.

2.7.4. Classical methods: ε-constraint method

The ε-constraint method is used to deal with problems having non-convex objective spaces. The MOOP is reformulated by keeping only one of the objective functions, f_μ, and transforming the others in inequality constraints [89]:

$$\begin{cases} \text{Minimise:} & f_\mu(\boldsymbol{x}) & \\ \text{Subjected to:} & f_i(\boldsymbol{x}) \leq \varepsilon_i, & i = 1, 2, \dots, k \text{ and } i \neq \mu \\ & g_i(\boldsymbol{x}) \leq 0, & i = 1, 2, \dots, m \\ & h_i(\boldsymbol{x}) = 0, & i = 1, 2, \dots, p \\ & x_i^{(L)} \leq x_i \leq x_i^{(U)}, & i = 1, 2, \dots, n. \end{cases} \tag{2.28}$$

where the parameter ε_i represents an upper bound of the value of the i-th objective function f_i. This method will be partially exploited in this work to reduce the objective space. In fact, the coverage and the revisit time of the SAR constellation will be constrained according to the system requirements. In this way, only solutions compliant with the requirements will be obtained. However, the problem will remain multi-objective.

2.7.5. Multi-objective evolutionary algorithms

Evolutionary Algorithms (EAs) are metaheuristic optimisation algorithms inspired by natural selection mechanisms based on Darwin's principle of the survival of the fittest. The basic operations of every EA are the following:

1. A random set of potential solutions, called "population", is generated. Each element of the set is called "individual" and contains the decision variables of the problem.
2. Some elements of the populations are selected, and the *fittest individuals* have more probability to be selected. In multi-objective evolutionary algorithms (MOEAs), the fittest solutions are usually ranked based on the principle of nondominance, i.e. nondominated solutions have a higher probability of being selected.
3. The selected individuals will "mate" and generate a set of "offspring" (or children), i.e. a new population created by randomly applying the evolutionary operators of crossover and mutation.
4. These children will constitute the new parents that will be selected in the next iteration. Each iteration is also called "generation".

EAs are stochastic algorithms since random decisions are made during the process. Therefore, different runs will typically produce different solutions. Moreover, MOEAs need to include also a diversity maintenance mechanism. In fact, because of the stochastic noise, EA can tend to reach a single solution, and some strategies need to be applied to avoid this risk. For this reason, some MOEAs penalise solutions that are too similar in the objective function space, promoting evenly spread solutions along the Pareto front. An alternative to facilitate diversity is a relaxed Pareto dominance selection technique, such as the ε-dominance mechanism [93]. Some MOEAs also include an external archive (or "secondary population") that is used to store all the best solutions found among all the generations, and that will constitute the approximation of the Pareto optimal set produced by the MOEA. There is a wide number of EAs, but some of the most used are: Strength Pareto Evolutionary Algorithm 2 (SPEA2) [94], Pareto Archived Evolution Strategy (PAES) [95], Nondominated Sorting Genetic Algorithm II (NSGA-II) [96], Pareto Envelope-based Selection Algorithm (PESA) [97], and Multi-objective Evolutionary Algorithm based on Decomposition (MOEA/D) [50].

2.7.6. Other metahuerisics

There are several other multi-objective metaheuristics available, for example, some bio-inspired algorithms, such as Artificial Immune Systems (AIS) [98], [99], Particle Swarm Optimisation (PSO) [100], and Ant Colony Optimisation (ACO) [101]. A database containing some of the most used MOEAs is available at `https://emoo.cs.cinvestav.mx/software.php`, created and maintained by Dr. Carlos A. Coello Coello. It is also worth mentioning PlatEMO [102], an open-source platform that offers more than 200 multi-objective algorithms in MATLAB.

The power of metaheuristics stems from their flexibility and capability to deal with complex problems such as constellation design. However, they do not provide deterministic results and could be computationally expensive. An additional issue is the extremely large number of algorithms of this kind, such that it is often difficult to choose the most suitable one for the specific problem [103]. This work will investigate two evolutionary algorithms: the NSGA-II algorithm included in MATLAB and the MOEA/D obtained from `https://emoo.cs.cinvestav.mx/software.php`.

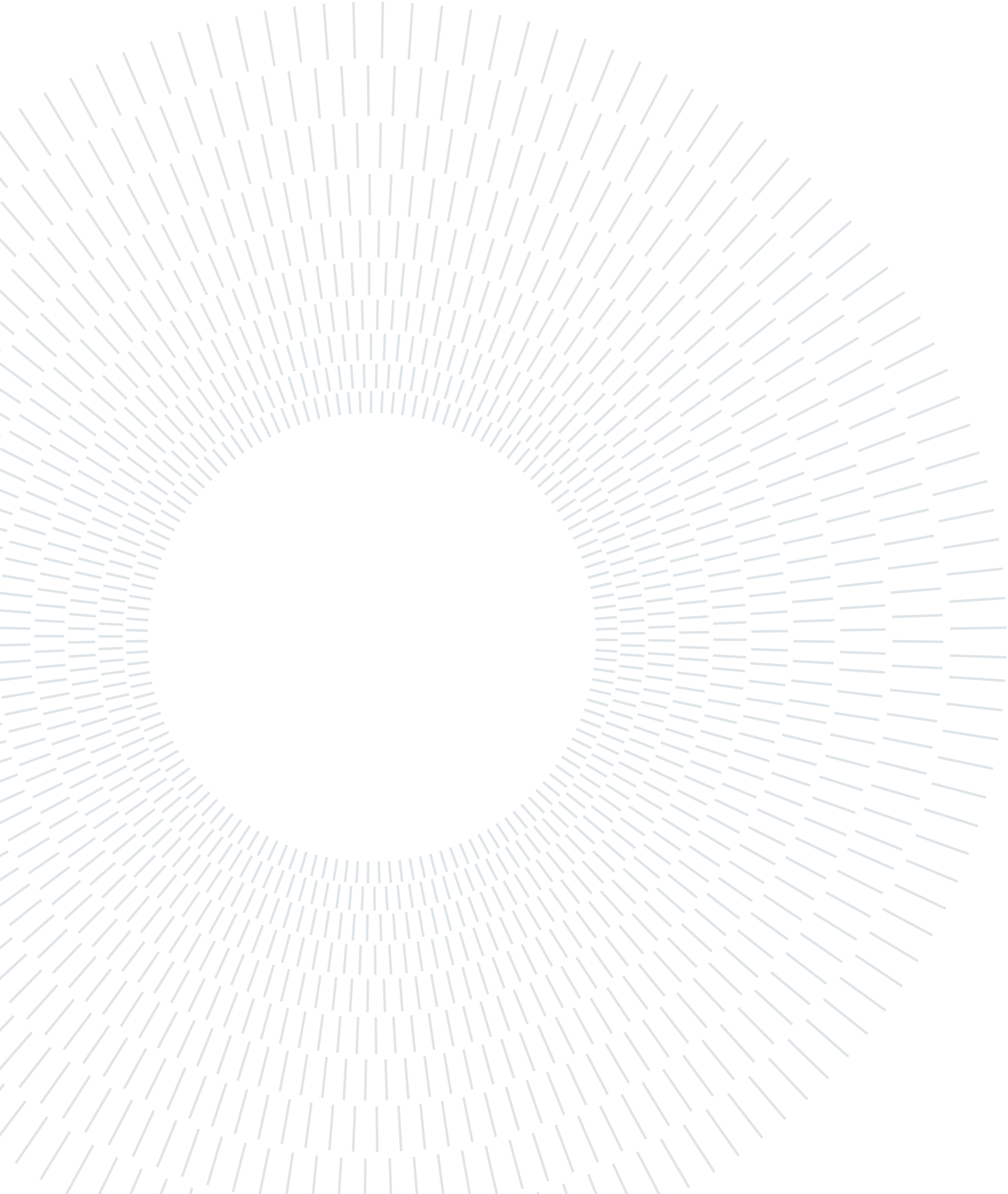

3 | Remote sensing missions

In this chapter, some of the currently active remote sensing missions will be reported and discussed, with a focus on small satellite constellations. Only SAR, optical, and mixed optical-SAR sensor constellations will be reported in the discussion. The review of these constellations partially refers to the work of Sartoretto [48] e Chiatante [47]. The main characteristics of some of the currently active missions are also summarised in Tables 3.1 to 3.3.

3.1. SAR constellations

3.1.1. Sentinel-1

Sentinel-1 is the first mission of the Copernicus Programme, and it is a constellation operated by ESA [104], [105]. The constellation was initially composed of two C-band SAR satellites, Sentinel-1A and Sentinel-1B, but Sentinel-1B has been retired due to an anomaly experienced on December 23, 2021. However, Sentinel-1C and Sentinel-1D are currently under development, with Sentinel-1C planned to be launched in 2023. The satellites are placed in a Sun-synchronous dawn-dusk orbit, with a LTAN of 18:00 h, an altitude of 693 km, and an inclination of 98.2°. Each satellite weighs approximately 2300 kg and has two solar panels measuring 7.36 x 1.73 m, while the SAR antenna is 12.3 m long and 0.821 m wide. The satellites are only right-looking, with an access angle that goes from 18.3° to 46.08°, and they can operate in four operating modes, that are Stripmap (80 km swath), Extra Wide Swath (400 km swath), Interferometric Wide Swath (250 km swath), and Wave. The maximum duty cycle is 25 minutes per orbit. The resolution is 5 x 5 m (Az. x Rg.) in Stripmap mode, 5 x 20 m in Interferometric Wide Swath mode (IW), and 20 x 40 m in Extra Wide Swath mode (EW). The system can acquire both single- and dual-polarisation images. The mission provides free and open data through the Copernicus Open Access Hub [106].

3.1.2. COSMO-SkyMed and COSMO-SkyMed - Second Generation

COSMO-SkyMed (COnstellation of small Satellites for the Mediterranean basin Observation) is a four-satellite Italian SAR constellation, launched between 2007 and 2010 [107], [108]. It is the first dual-use (military and civil) Earth observation constellation, funded by the Italian Ministry of Research and the Italian Ministry of Defence. The program is managed in cooperation between ASI and the Ministry of Defence, with Thales Alenia Space Italia (TAS-I) serving as the prime contractor. Some of the main applications of COSMO-SkyMed data include defence and security applications (such as surveillance, intelligence, mapping, damage assessment, vulnerability assessment, and target detection/localisation), risk management applications (such as flood, drought, landslide, volcanic/seismic, forest fire, industrial hazard, and water pollution monitoring), and other applications such as marine and coastal environment monitoring, agriculture, forestry, cartography, environment, geology and exploration, telecommunication, utilities and planning.

Starting in 2018, COSMO-SkyMed Second Generation (CSG) [109], [110] began providing continuity for the mission. Currently, there are six active COSMO-SkyMed satellites (four of the first generation and two of the second generation), and the remaining two satellites, CSG-3 and CSG-4, are scheduled to be launched in 2024 and 2025, respectively.

The COSMO-SkyMed satellites are placed in Sun-synchronous polar orbits with an inclination of 97.86° at a nominal altitude of 619.6 km and an orbital period of 97.22 minutes. The LTAN is 06:00, and each satellite is placed in the same nominal orbit, with a difference in the true anomaly. The constellation has a maximum revisit time of 12 hours over Italy, and it can operate in three different System Operative Modes, which can only be changed by the Italian Government Authorities [108]:

- Routine mode: user requests are planned once a day (a request can be satisfied within 72 hours).
- Crisis mode: planning is done twice a day (a user request can be satisfied within 36 hours).
- Very urgent mode: an asynchronous mode that allows the servicing of an image acquisition request with the minimum possible latency (a user request can be satisfied within 18 hours).

Each satellite mounts an X-Band SAR antenna that measures 5.7 x 1.4 m and can operate in three different acquisition modes: Spotlight, Stripmap and ScanSAR, with a swath that ranges from 10 km to 200 km, and a resolution that can reach 0.3 x 0.6 n [Az. x Rg.] in Spotlight mode for the Second Generation. The First Generation satellites weigh 1700 kg each and are equipped with eight solar arrays with a combined area of 18.3 m^2. The Second Generation satellites weigh 2230 kg each. The system has a duty cycle of 10 minutes in Stripmap and ScanSAR modes.

3.1.3. ICEYE constellation

ICEYE's constellation is the world's largest small SAR satellite constellation, currently consisting of 21 satellites with 27 additional spacecrafts planned to be launched by 2024 [111], [112]. The overall mission objective of ICEYE is to provide timely and reliable Earth observation data to enable better decision-making. Each satellite weighs 85 kg and has five fixed solar panels that can generate a peak power of 345 W [113]. The satellites are placed in either Sun-synchronous or inclined orbits at an altitude between 472 and 582 km. The X-band SAR sensor on each satellite utilises an electronically steerable active phased array antenna that measures 3.2 x 0.4 m. It is capable of operating in Spotlight, Stripmap, SLEA (Spot Extended Area), and ScanSAR modes, with a ground resolution of 1 x 1 m in Spotlight mode, 3 x 3 m in Stripmap mode, and 15 x 15 m in ScanSAR mode. The swath is 30 km in Stripmap mode, with an incidence angle ranging from 10° to 30°, and 5 km in Spotlight mode, with an incidence angle between 20° and 35°. Only single-polarisation VV data is available. A tasking service is available, and images are usually delivered within 24 to 48 hours of the initial request[114].

3.1.4. Capella X-SAR

Capella Space is a commercial start-up company that is developing a constellation of 36 SAR microsatellites [115], [116]. The constellation is currently composed of 8 satellites, with a mass of about 112 kg and orbiting in Sun-synchronous and inclined orbits at an altitude of 481-588 km. The main payload is a 3.5 m aperture mesh-based reflector X-band SAR antenna that acquires single-polarisation HH images. The resolution depends on the nominal scene size: it ranges from 0.5 to 3.1 m for a Spot and from 1.5 m to 11.5 m for a Strip, with a swath of 5 km for both modes. Solar panels provide up to 400 W of power, contributing to a duty cycle of 9 minutes per orbit during peak usage orbits. The access angle is 25°-40° for Standard Products, 15°-45° for Extended Products and 5°-45° for custom products. A tasking service supports three "Tasking Tiers", which give the certainty that a tasking request will be collected within a 1-day, 3-day, or 7-day period.

	Sentinel-1	**Cosmo-SkyMed Prima Generazione**	**Cosmo-SkyMed Seconda Generazione**	**ICEYE**	**Capella**
N. of satellites	1 (2 in 2023)	4	2	21	8
Orbit type	SSO	SSO		SSO/inclined	SSO/inclined
Altitude	693 km	619 km		472 - 582 km	481 - 588 km
Inclination	98.2°	97.86°		Polar/inclined	45° / 53° / 97°
LTAN/LTDN	18:00	06:00		15:05; 14:04; 21:36; 22:30	9:00-11:00/16:30
Satellite mass	2300 kg	1700 kg	2230 kg	85 kg	112 kg
Sensor Name	C-SAR	SAR 2000	CSG-SAR SAS		
Band	C-Band	X-Band	X-Band	X-Band	X-Band
Resolution (Az. x Rg.)	5 x 5 m (Stripmap); 20 x 40 m (EW); 5 x 20 m (IW); 5 x 5 m (Wave)	1 x 1 m (Spotlight); 5 x 5 m (Himage); 20 x 20 m (Ping Pong); 30 x 30 m (ScanSAR Wide); 100 x 100 m (ScanSAR Huge)	0. 8 x 0.8 (Spotlight); 3 x 3 (Stripmap); 12 x 5 (Ping-Pong); 3 x 3 (QuadPol); 20 x 4 m (ScanSAR-1); 40 x 6 m (ScanSAR-2)	0.25x0.5m (Spotlight); 3x0.5-2.5 m (Stripmap); 1x0.5 m (SLEA); 15 x 15 m (ScanSAR)	0.5-3.1 x 0.5-3.1m (Spotlight); 1.7-11.5 x 1.5-11.5 m (Stripmap); 1-5 x 0.7-5 m (Site)
Polarizations	Single (HH, VV); Dual (HH+HV, VV+VH)	Single (HH, HV, VH, VV); Alternating (HH/VV, HH/HV, VV/VH)	Single (HH, VV); Dual (HH+HV, VV+VH); Quad (HH+HV+VV+VH)	VV	HH
Swath	80 km (Stripmap); 400 km (EW); 250 km (IW)	10 km (Spotlight); 40 km (Himage); 30 km (Ping Pong); 100 km (ScanSAR Wide); 200 km (ScanSAR Huge)	10 km (Spotlight); 40 km (Stripmap); 30 m (Ping-Pong); 40 (QuadPol); 100 km (ScanSAR-1); 200 km (ScanSAR-2)	30 km (Strip); 5 km (spot); 15 km (SLEA); 100 km (ScanSAR)	5 km
Access angles	18.3°-46.08° (Only right looking)	20°-59°	20° - 60°	10° - 30° Stripmap; 20° - 35° (Spotlight)	25° - 40° (Standard Products); Up to 15° - 45° (Extended Products); Up to 5° - 45° (Custom Products)
Acquisition modes	Stripmap; Interferometric Wide Swath; Extra Wide Swath; Wave	Spotlight; Stripmap (Himage and Ping Pong); Scansar (Wide and Huge)	Spotlight; Stripmap; Ping-Pong; QuadPol; ScanSAR	Spotlight, Stripmap, Scansar	Spotlight, Sliding Spotlight, Stripmap
Tasking service	N	Y	Y	Y	Y
Data policy	Free & open	Commercial; dual-use	Commercial; dual-use	Commercial	Commercial

Table 3.1: SAR constellations main features

3.2. Optical constellations

3.2.1. Sentinel-2

Sentinel-2 is a constellation of two optical imaging satellites that is part of the Copernicus Program [117], [118]. The main instrument on these satellites is a Multispectral Imager (MSI) with two focal planes that collect visible and near-infrared light (VNIR) and short-wave infrared (SWIR) radiation. The MSI has three visible bands with a spatial resolution of 10 m, one visible band with a resolution of 60 m, three near-infrared bands with a resolution of 20 m, and six short-wave infrared bands with a resolution of 60 m. The swath of the instrument is 290 km. The total mass of each satellite is approximately 1200 kg, and a 7.1 m^2 solar panel provides energy to all subsystems. The images are typically acquired in push-broom mode, but a lateral mode capability for emergency event monitoring is also available. The two Sentinel-2 satellites are in Sun-synchronous orbits with a local time at ascending node (LTAN) of 10:30, at an altitude of 786 km. The mission provides free and open data through the Copernicus Open Access Hub [106].

3.2.2. Planetscope (DOVEs)

PlanetScope is a multispectral satellite constellation operated by Planet Labs, consisting of approximately 130 CubeSats 3U (called DOVEs) [119]–[121]. Since 2016, three DOVE types with different capabilities have been launched: Dove Classic, Dove-R, and Super-Dove. The resolution of the images captured by these satellites is approximately 3 - 4 m in the visible and near-infrared spectral range (VNIR). The DOVEs are able to acquire off-nadir images with a maximum angle of +/- 5° and a swath of 25 km for Dove Classic and Dove-R, and 32.5 km for SuperDove. The DOVEs are launched in batches called "flocks", consisting of tens of CubeSats, and they operate at an altitude range of 450 - 580 km in Sun-synchronous or generally inclined orbits. Each DOVE has a weight of approximately 5.8 kg and is equipped with a fixed solar panel measuring 0.3 x 0.7 m.

3.2.3. SkySat

Skysat is the largest constellation of high-resolution imaging satellites, composed of 21 satellites that provide panchromatic and multispectral imagery [119], [122], [123]. It is operated by Planet Labs, which acquired the constellation when they purchased Terra Bella company (formerly Skybox Imaging) from Google in 2017. The first satellite, SkySat-1 was launched in 2013. The resolution is variable, depending on the orbit altitude of each satellite, and ranges from 0.57 m to 0.86 m for panchromatic images, and from 0.75 m to

1 m for multispectral images. The swath is 8 km at the nadir for SkySat-1 and-2, 5.9 km for SkySat-3 to -15 and 5.5 km for SkySat-16 to -21. Moreover, the constellation provides stereo and tri-stereo images, and can capture video clips lasting from 30 to 120 seconds at 30 frames per second. The constellation exploits Sun-synchronous and generally inclined orbits. SkySat-1 to -15 are in Sun-synchronous orbits with the local time at descending node (LTDN) ranging from 10:30 to 14:00, while the remaining satellites are in orbits with an inclination of 53°. The altitude is from 400 km to 600 km. The mass of the satellites is approximately 110 kg, and they have body-mounted solar panels with a total area of $1.6\,\mathrm{m}^2$.

3.2.4. BlackSky

BlackSky Constellation [124] is a constellation of high-resolution imaging microsatellites. It is operated by BlackSky Global, which was formerly a subsidiary of Spaceflight Industries. The microsatellites are developed by LeoStella LLC, a partnership between Thales Alenia Space and BlackSky. There are currently 17 operational microsatellites in the constellation, with an expected lifespan of approximately four years each. The ultimate goal of BlackSky Global is to create a constellation of 60 satellites. Each satellite has a SpaceView-24 optical sensor, with a resolution of 1 m and a swath of 6 km at an altitude of 500 km [125]. The imager has four channels, three of which are visible (RGB), and one is panchromatic. Off-nadir imaging is possible up to angles of 30 degrees.

3.3. Hybrid-sensors (Optical and SAR) constellations

There are several examples of hybrid-sensor constellations that include both optical and SAR sensors. However, there is no currently existing constellation optimised for optical-SAR data fusion that can provide synchronous mixed-sensor data.

For example, the Airbus Defence and Space constellation [126] consists of three SAR satellites (TerraSAR-X, TanDEM-X and PAZ) and nine high-resolution optical satellites (two Pleiades, two Pleiades Neo, Vision-1 and SPOT 6 and 7).

The Korea Aerospace Research Institute (KARI) has developed and operates three optical satellites (Kompsat-2 [127], Kompsat-3 [128] and Kompsat-3A [129]) and one SAR satellite (Kompsat-5 [130]). However, this constellation is approaching its end of life, with the Kompsat-2 mission expiring in December 2022 and the other missions ending in 2023. Kompsat-5 will be followed by Kompsat-6 at the end of 2023 [131].

Sentinel-1 and Sentinel-2, developed by the European Space Agency (ESA), can also be considered an optical-SAR constellation as they both provide free and open-source optical and SAR images of the entire planet for the Copernicus program.

Finally, ICEYE and Satlantis have proposed a four-satellites constellation called Tandem4EO [132]. The two SAR imaging satellites will be placed in a sun-synchronous orbit and fly in a bistatic formation, while the two optical imaging satellites will trail behind in the same orbit.

	Planetscope	**SkySat**	**BlackSky**
N. of satellites	>130	21	15 (planned 60)
Orbit type	SSO/Inclined	SSO (SkySat 1-15) Inclined (SkySat 16-15)	SSO/Inclined
Altitude	450 – 580 km	SkySat 1-2: 600 km SkySat 3-15: 450 km SkySat 16-18: 400 km	391 – 585 km
Inclination	98°/52°	53°/Polar	42°- 53°/Polar
LTAN/LTDN	7:30 – 11:30	10:30 - 14:00	NA
Satellite mass	5.8 kg	110 kg	56 kg
Sensor Name	PS2, PS2.SD, PS2B.SD	N.A.	SpaceView-24
Spectral Bands	VNIR	PAN, VNIR	VIS
Resolution (GSD)	3.0 – 4.2 m	0.57-0.86 m (PAN) 0.75-1 m (MS)	1 m @ 500 km
Bit Depth	12-bit	12-bit	NA
Swath	PS2 and PS2.SD:25 km PSB.SD: 32.5 km @ 475 km	8 km (SkySat-1 to -2) 5.9 km (SkySat-3 to -15) 5.5 km (SkySat-16 to -21)	6 km @ 500 km
View angle	+/- 5°	+/- 30° (Standard) +/- 45° (Max)	+/- 30°
Solar panel size	$0.2\,\mathrm{m}^2$	$1.6\,\mathrm{m}^2$	NA
Tasking service	N	Y	Y
Data policy	Commercial	Commercial	Commercial

Table 3.2: Optical constellations main features (SmallSats)

	Sentinel-2	Pleiades	PRISMA	Landsat-8		Landsat-9	
N. of satellites	2	2	1	1		1	
Orbit type	SSO	SSO	SSO	SSO		SSO	
Altitude	786 km	694 km	615 km	705 km		705 km	
Inclination	98.62°	98.2°	97.87°	98.2°		98.2°	
LTAN/LTDN	10:30	10:30	10:30	NA		NA	
Satellite mass	1200 kg	940 kg	820 kg	2071 kg		2071 kg	
Sensor Name	MSI	HiRI	PRISMA	OLI	TIRS	OLI-2	TIRS-2
Spectral Bands	VNIR, SWIR	PAN, VNIR	VNIR, SWIR, PAN	VNIR, SWIR	TIR	VNIR, SWIR	TIR
Resolution (GSD)	10 – 60 m	0.7 m (PAN), 2.8 m (MS)	30 m (Hyp.), 5 m (PAN)	30 m (MS), 15 m (PAN)	100 m	30 m (MS), 15 m (PAN)	100 m
Bit Depth	12-bit	12-bit	12-bit	12-bit		14-bit	
Swath	290 km	20 km < 110 km (Mosaic)	30 km	190 km	190 km	185 km	185 km
View angle	NA	+/- 30° (standard), +/- 47° (Max)	+/- 20.7°	Nadir pointing		Nadir pointing	
Tasking service	N	Y		N		N	
Solar panel size	$7.1\,\mathrm{m}^2$	$6.9\,\mathrm{m}^2$	NA	$3.6\,\mathrm{m}^2$		NA	
Data policy	Free & open	Commercial, dual civil/military		Free and open		Free and open	

Table 3.3: Optical constellations main features

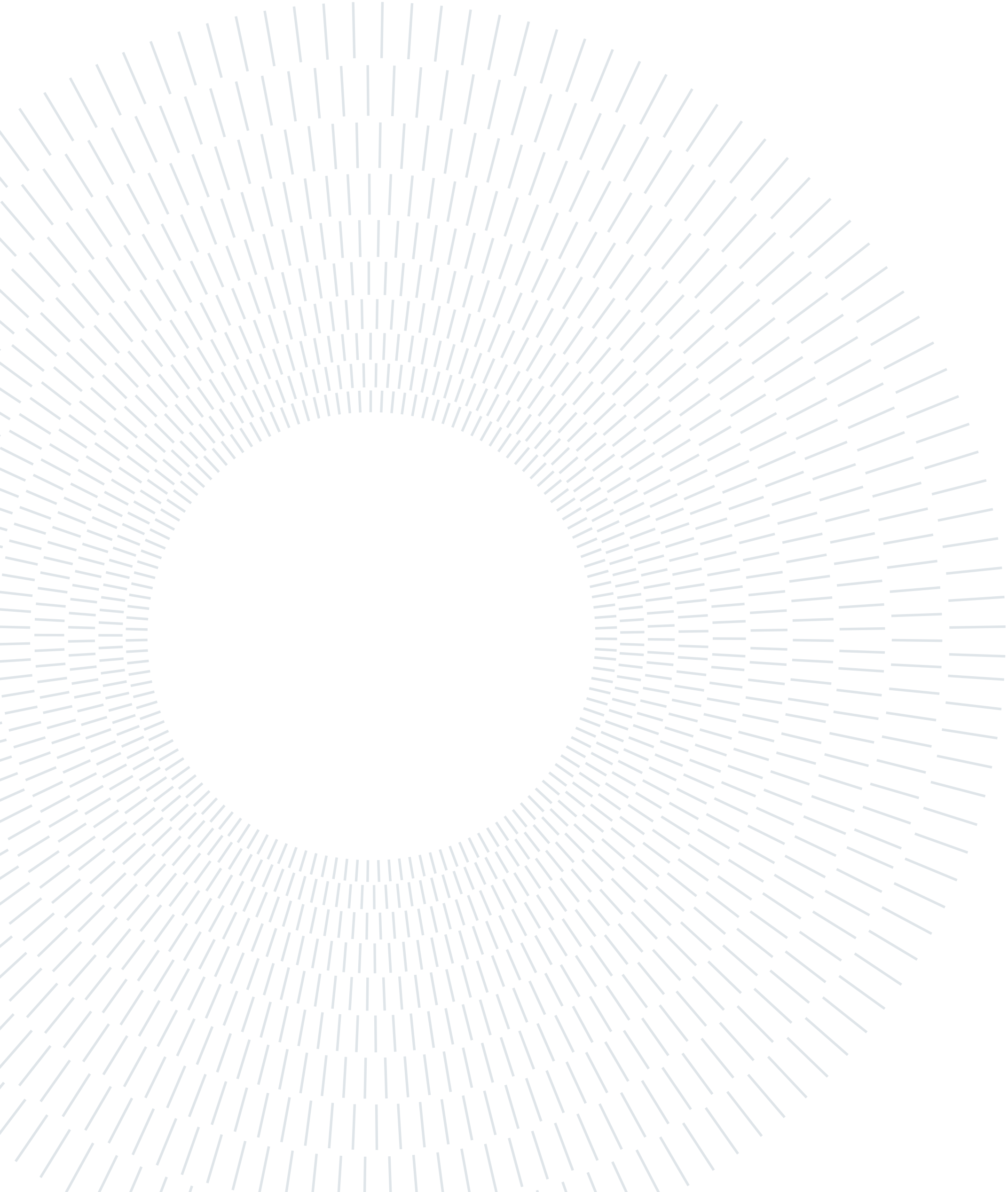

4 | Case studies

The requirements of the constellation will be derived from the analysis of two real emergency scenarios which affected the Italian territory. The two events involved emergencies related to critical infrastructures and floods, and they are the 2017 Abruzzo snowfall and the 2022 Marche flood. With their analysis, it will be possible to identify the main actors involved in the emergency response, their activities and their needs, which will be translated into user requirements. Moreover, the two events are selected because of their high severity. Therefore, the derived requirements are expected to work well even in highly critical future scenarios.

4.1. 2017 Abruzzo snowfall

During the winter of January 2017, Eastern and Central Europe experienced a period of extreme cold and heavy snowfall, with Italy's Abruzzo region particularly impacted. In this region, a total of 20 million tons of snow fell, with more than 2 meters of snowfall recorded in the medium-high altitude areas of the central Apennines. The intense snowstorms also caused widespread damage to transmission and distribution lines, resulting in blackouts affecting up to 150,000 users [133], [134]. The faults were mainly attributed to the phenomenon of so-called ice sleeves. The persistent high humidity resulted in wet snowfall (or sticky snow), which has facilitated the formation of ice sleeves on the overhead power lines, reaching a 15 kg/m overload in areas where the design criteria at most did not exceed 5 kg/m. Up to 1600 workers were employed during the event to restore the service.

4.1.1. Event timeline

The event was characterised by four distinct phases. The full timeline with the evolution of the event is summarised in Table 4.1. The first phase began on the night of January 15th-16th and affected the area surrounding the city of Chieti, resulting in the disconnection of 130,000 users (90,000 of which were due to faults on the high-voltage power lines). By the evening of January 16th, 75,000 of the disconnected users had their service restored.

The second phase occurred during the night of January 16th-17th, during which a new adverse weather event caused additional damage to the high-voltage power lines and distribution grid, primarily in the areas of Teramo and Pescara. This resulted in a total of 159,000 users being disconnected, 90,000 of which were due to faults on the high-voltage power lines. By the evening of January 17th, 72,000 of these users had their service restored.

The third phase, which took place from January 18th until the evening, affected the areas of Teramo, Pescara, and L'Aquila. A total of 101,000 users were disconnected due to further damage to the lines. Additionally, a sequence of four earthquakes with a magnitude greater than 5, with a maximum of 5.5, affected the area and slowed the restoration of the damaged lines.

The final phase was the recovery phase, which began on the evening of January 18th and concluded on January 22nd with the complete service restoration.

During this event, the W.O.L.F. system designed by RSE for ice sleeves forecasting was already available. However, no information regarding its usage has been found. Nevertheless, it is possible to utilise its events archive available on the W.O.L.F. website to identify the areas at risk during the event and their extent. As can be observed in Figure 4.1, the area at risk was extensive, spanning approximately 37 000 km^2, equivalent to approximately 12-13% of the total surface area of Italy. In addition to Abruzzo, numerous other regions of the Appennini mountains and a part of Sardinia were also at risk.

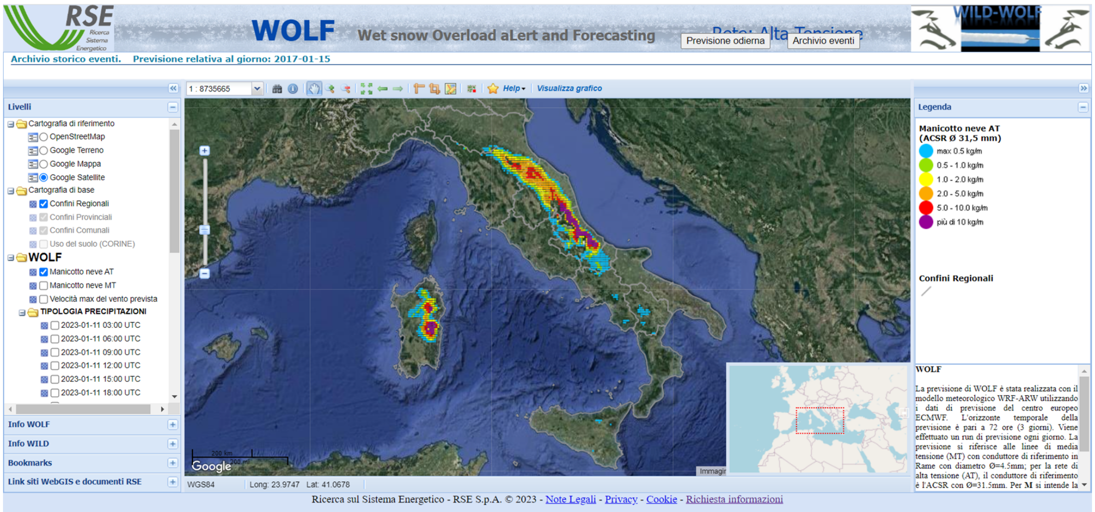

Archivio storico eventi. Previsione relativa al giorno: 2017-01-15

WOLF

La previsione di WOLF è stata realizzata con il modello meteorologico WRF-ARW utilizzando i dati di previsione del centro europeo ECMWF. L'orizzonte temporale della previsione è pari a 72 ore (3 giorni). Viene effettuato un run di previsione ogni giorno. La previsione si riferisce alle linee di media tensione (MT) con conduttore di riferimento in Rame con diametro Ø=4.5mm; per la rete di alta tensione (AT), il conduttore di riferimento è l'ACSR con Ø=31.5mm. Per **M** si intende la

Ricerca sul Sistema Energetico - RSE S.p.A. © 2023 - Note Legali - Privacy - Cookie - Richiesta informazioni

Figure 4.1: Forecast of the W.O.L.F. system by RSE for January 15th, 2017. It is possible to determine the extent of the area at risk, which encompasses not only the Abruzzo region but also Marche, Sardinia, Molise, and other regions of the Appennini mountain range.

Date	**Number of disconnections**	**Affected areas**	**Resources employed**
16 January 16:00	130,000	Chieti	300 workers; 200 operational vehicles; 50 electrical generators
16 January 20:00	55,000	Chieti	300 workers; 200 operational vehicles; 50 electrical generators
17 January 08:00	159,000	Teramo, Pescara	750 workers; 300 operational vehicles; 200 electrical generators
17 January 22:00	87,000	Teramo, Pescara	750 workers; 300 operational vehicles; 200 electrical generators
18 January 08:00	101,000	Teramo, Pescara, Chieti	1300 workers; 400 operational vehicles; 450 electrical generators
18 January 24:00	98,300	Teramo, Pescara, Chieti	1300 workers; 400 operational vehicles; 450 electrical generators
19 January 24:00	63,000	Teramo, Pescara, Chieti	1430 workers; 570 operational vehicles; 500 electrical generators
20 January 24:00	35,000	Teramo, Pescara, Chieti	1430 workers; 570 operational vehicles; 500 electrical generators
21 January 20:00	21,000	Teramo, Pescara	1600 workers; 600 operational vehicles; 600 electrical generators
22 January 07:00	14,300	Teramo	1600 workers; 600 operational vehicles; 960 electrical generators
23 January 08:30	6,500	Teramo	1600 workers; 600 operational vehicles; 960 electrical generators
24 January 10:00	3,000	Teramo	1600 workers; 600 operational vehicles; 1000 electrical generators

Table 4.1: 2017 Abruzzo snowfall timeline.

4.2. 2022 Marche flood

On 15 and 16 September 2022, the Italian region of Marche was struck by heavy rains and floods, particularly the provinces of Ancona, Pesaro and Urbino. In total, 12 people were killed, a woman is missing, 150 people were evacuated from their homes, and €2 billion in damages were caused [135]–[137]. One of the most affected municipalities was Cantiano (PU), where it was recorded the highest rainfall in the intensity of the last 10 years, with a peak of 90 mm/h between the 20:00 and 21:00 (CET) [138] and a total of 420 mm of rain accumulated between the 15:00 and the 22:30. The water level of several rivers and streams dramatically increased. In particular, the most affected drainage basins were the ones of Candigliano, Cesano, Misa, Sentino and Musone. The level of the Misa river rapidly increased from 0.21 m to 5.31 m in about an hour and a half [139].

4.2.1. Event timeline

The event timeline has been reconstructed mainly thanks to the event report by the regional Functional Center of the Civil Protection [140], and to the data obtained by the SIRMIP system (*Sistema Informativo Regionale Meteo-Idro-Pluviometrico*) [141].

On September 14th at 12.06 (GMT+2), the Functional Center, which is responsible for the Reginal warning system for hydrogeological and hydraulic risks, issued the first hydraulic criticality bulletin, in which the ordinary criticality (i.e. *yellow alert*) was defined for hydrogeological risk in the alert zones 1 and 3 for September 15th. In addition, at 13:00, a warning of adverse weather conditions due to wind has been issued for alert zones 1, 2, 3 and 5, valid for the day of the 15th. The alert zones in which the region is divided are shown in the map in Figure 4.2, and established in the *Decreto Dirigente Servizio Protezione Civile n. 136 del 28 giugno 2019 - Allegato 1* [142] .

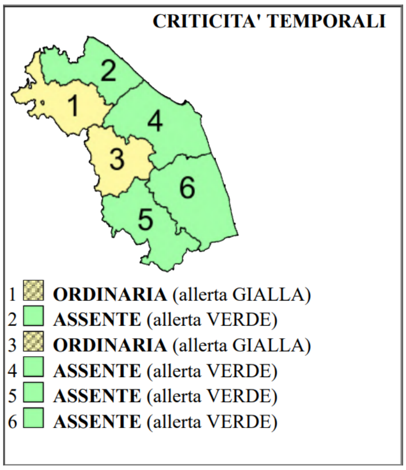

Figure 4.2: Marche region alert zones. The *yellow alert* was defined for hydrogeological risk due to storms in the alert zones 1 and 3, as reported in the bulletin of September 14th.

Because of the uncertainties related to the weather forecast models, the severity of the event was not correctly predicted. So the affected areas received only a yellow or even green alert.

Starting from the afternoon of the 15th, the rainfall began to affect the areas around Monte Catria, affecting the mountainous area of Cesano, Misa and Esino's basins. During the evening, rains moved southward and affected the area near Monte San Vicino (see the map in Figure 4.3). For example, the rainfall data from Cantiano's rain gauge are reported in Figure 4.4. The first rains are documented at about 15:45 CET, and they reached a peak of intensity of 11.43 mm/min at 20:00 and 11.32 mm/min at 22.15, as seen in Figure 4.4b. The total accumulated precipitation is shown in Figure 4.4a.

		Total accumulated precipitation [mm] 15-16 September 2022				Return period (years)			
Rain gauge	Basin	max 3H	max 6H	max 12H	max 24H	3H	6H	12H	24H
Cantiano	Biscubio	256.6	384	419	419	>1000	>1000	>1000	>1000
Monte Acuto	Cesano	248.4	343	384.2	384.4	>1000	>1000	>1000	>1000
Arcevia	Misa	94.8	117.8	128.8	129.2	>1000	>1000	910	200
Barbara	Misa	111.4	121.2	127	127.2	>1000	>1000	>1000	140
Colle	Misa	162.4	186.4	204	204	>1000	>1000	>1000	>1000
Sassoferrato	Sentino	62.8	99.8	99.8	100.4	130	600	120	30
Colleponi	Sentino	68	122	122.2	122.6	230	>1000	750	150
Monte San Vicino	Musone-Esino	108.2	120	192.8	193.6	>1000	750	>1000	>1000
Cingoli	Musone	160.4	184.6	247.2	247.6	>1000	>1000	>1000	>1000

Table 4.2: Total maximum accumulated precipitation and estimate of the return period of the recorded rainfall by some relevant rain gauges for the 2022 Marche flood event [140].

Rain levels had a similar intensity in other areas, with extreme rainfall rates that were well above 60 mm of rainfall over a three hours period and a return period that in some areas exceeded 1000 years. In Table 4.2 are reported the maximum accumulated precipitation recorded by some of the most relevant rain gauges in 3, 6, 12 and 24 hours and the rainfall return periods [140].

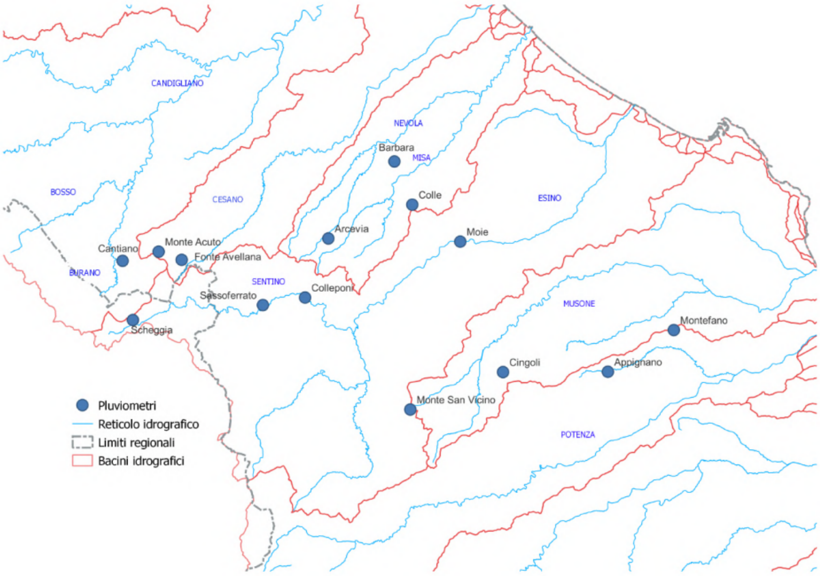

Figure 4.3: Location of a subset of rain gauges of the regional network [140].

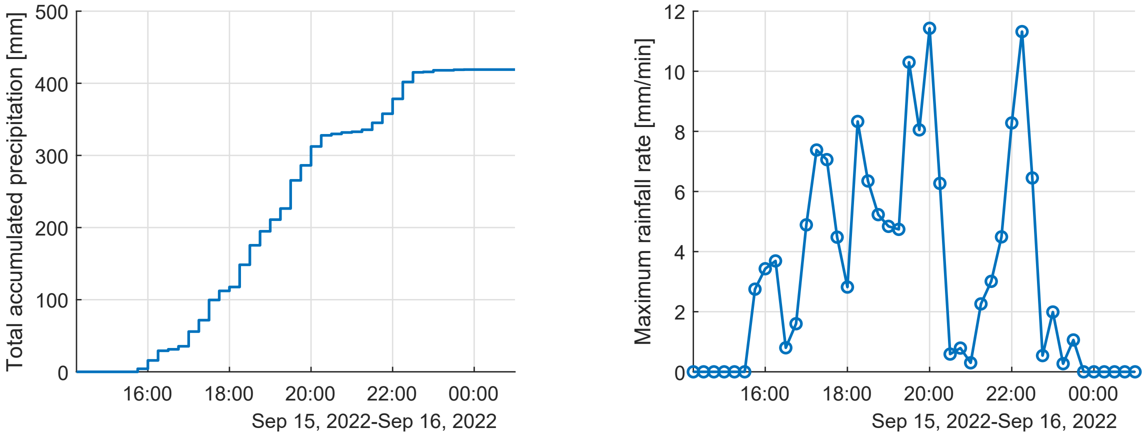

(a) Total accumulated precipitation recorded in Cantiano (PU), during the 15 and 16 September. The time of the plot is expressed in CET (GMT+2).

(b) Maximum rain rate recorded in Cantiano (PU), during the 15 and 16 September. The time of the plot is expressed in CET (GMT+2).

Figure 4.4: Total accumulated precipitation and maximum rain rate registered in Cantiano during the 15 and 16 September 2022 [141].

The heavy rainfall caused a rapid rise of hydrometric levels above the alarm threshold in the basins of the central belt of the region, causing widespread flooding. The basins most affected were those of Candigliano, Cesano, Misa, Sentino and Musone. Hydrometric levels recorded by the stream gauges belonging to the Misa's basin are illustrated in Figure 4.5. The Serra dei Conti and Pianello di Ostra's gauges were damaged by the flood wave respectively at 20:26 and 20:32 CET, while the Passo Ripe's gauge had some transmission problems of interference caused by the wave between 21:25 and 22:42 CET. In Senigallia, the Misa river overflowed, flooding a large part of the city starting from about 23:59 and receding at 05:20 of the 16th, after it reached a peak at 01:40. A summary of the event timeline is shown in Table 4.3. It is possible to notice how fast the event was, with the first floods reported just four hours after the beginning of the rainfalls. Moreover, the water level of the Misa river rapidly increased because of the flood wave, inundating the city of Senigallia in a few hours.

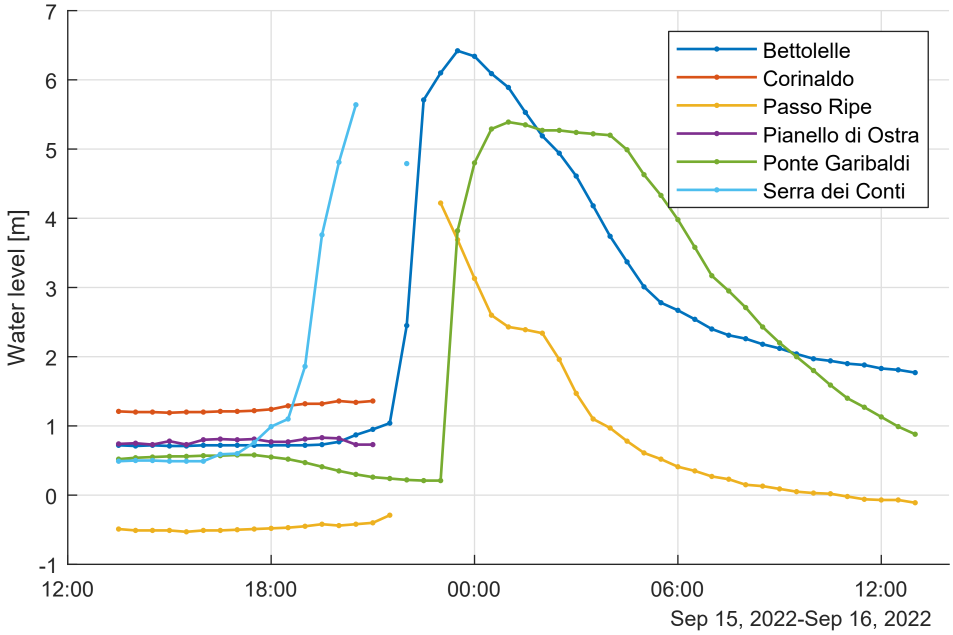

Figure 4.5: Water level of the Misa river recorded by the stream gauges of Serra de' Conti, Pianello di Ostra, Corinaldo (Nevola), Passo Ripe, Bettolelle (Misa) and Ponte Garibaldi. The time of the plot is expressed in CET (GMT+2).

2022 Marche flood	
14 September 12:06	The Functional Center issued the first hydraulic criticality bulletin.
14 September 13:00	Warning of adverse weather conditions due to wind by the Functional Center.
15 September 15:45 ca.	The rainfall began to affect the areas around Monte Catria.
15 September 16:00-19:00	The rain gauges of Fonte Avellana, Monte Acuto and Cantiano recorded 222.6 mm, 212.2 mm and 206.8 mm of rainfall over a three hours period.
15 September 20:03	First floods are reported in the area near Cantiano [143].
15 September 20:26	The stream gauge of Serra dei Conti (Misa) was damaged by the flood wave.
15 September 20:26	The Mayor of Senigallia activated the COC *Centro Operativo Comunale* [144].
15 September 21:15	The Mayor of Senigallia orders the citizens to go to the upper floors of buildings [145].
16 September 23:59	The Misa river overflows in Senigallia [146].
16 September 01:40	The Civil Protection informs that the water level of the Misa river reached its peak [145].
16 September 05:20	The Misa river began to slowly recede from Senigallia [145].

Table 4.3: 2022 Marche flood timeline.

5 | Requirements definition

The requirements of the constellation were defined after an operational analysis, which aims to identify the system's main actors, activities, goals, and interaction with each other [147]. Therefore, the operational analysis answers the question of "what system users must achieve", and it helps to define the main needs of future users without yet defining the physical system. The users' needs are then formalised in textual user requirements, which are statements of what the users want the system to do for them, and since they are written from the user's viewpoint, they are not too technical. User requirements are then translated at a more technical level into system requirements, which define the system's performance to fulfil the user requirements. The analysis is performed starting from the investigation of the case studies introduced in Chapter 4, and placing the main actors involved during the two events inside an architecture for the emergency response.

5.1. Operational analysis for critical infrastructures monitoring

The requirements for critical infrastructure monitoring are derived thanks to the analysis of the 2017 Abruzzo snowfall case study, described in Section 4.1. In this context, the Italian transmission line operator has been identified as the end-user of the system, and the entities involved in the operational architecture are the following:

- *The Italian Transmission System Operator* (TSO): it is one of the possible constellation users which could employ remotely sensed data to detect the formation of ice sleeves over the conductors of overhead power lines and evaluate the risk based on their displacement. Furthermore, it manages energy flows along the national power grid. Therefore, during a critical wet snow event, it could plan to provide an additional de-icing current over the conductors impacted by ice sleeves to counteract ice accretion. Alternatively, if it is not possible to increment the current, line sectionalising can be adopted to pre-emptively isolate a section of the line from the rest of the grid and thus minimise the impact of cable breakage on power distribution, preventing cascading failures.

- *The Italian transmission line*: it is the passive entity composed of the national high-voltage transmission lines that can be potentially damaged by the formation of ice sleeves. During the emergency, the conductors of the line can be heated to prevent or reverse the accretion of ice sleeves, or they can be sectionalised to prevent localised failures from cascading into larger widespread outages.
- *The W.O.L.F. system by R.S.E.*: it is a tool used as an early warning system, which is able to forecast cable loads caused by ice sleeves and locate the areas over the Italian territory that are most at risk. Whenever an area is marked at risk by this system, the constellation shall be automatically scheduled to sense that specific area with a higher priority.
- *The Space Segment*: it is devoted to sensing the scene with the aim of detecting ice sleeves, and it is composed of the optical and SAR satellites of the constellation.
- *The Ground Segment*: it has the main role of operating the system, and it performs four main operational activities. The first activity is managing the acquisition scheduling based on the available resources of the constellation and prioritising the areas at risk evaluated by analysing forecasts from the W.O.L.F. system. Moreover, the constellation should be quickly rescheduled once an ice sleeve has been detected to achieve an even faster sampling frequency of the phenomenon. The other activities are data collecting and storage and image processing. Indeed, Raw data downlinked from the satellites must be collected, stored, and then processed (e.g. focusing, co-registration, geocoding, atmospheric correction) to obtain the final product.

How all these entities would interact with one another is schematised in the operational architecture in Figure 5.1, which exemplifies the capability of the system to provide emergency response operations during a wet snow event.

The behaviour of all the stakeholders and the timeline of the activities performed for emergency response during a critical event are described in the operational scenario in Figure 5.2. The W.O.L.F. system provides the daily forecast of cable loads up to 72 hours in advance, and it shall be used to schedule the constellation so that the available resources are mainly focused on the areas at risk. After the sensing, the data shall be transferred to the ground segment, where they are collected, stored and processed. The processed images are used to reschedule the constellation to give higher priority to areas that are effectively affected by wet snow. In fact, the W.O.L.F. system works with forecasting

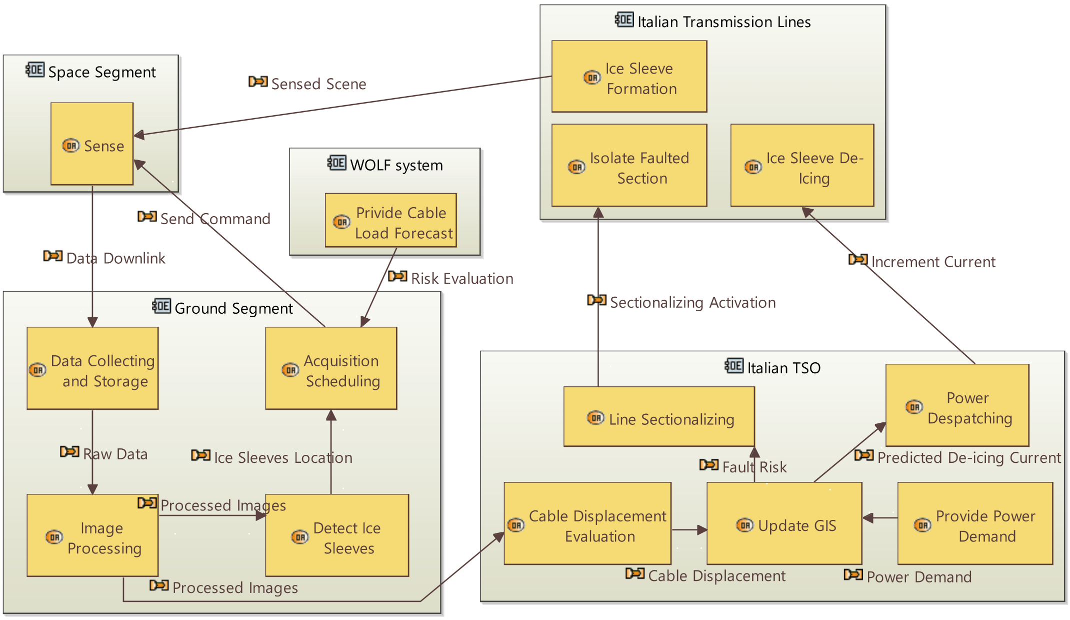

Figure 5.1: Operational architecture for ice sleeves accretion emergency response.

models with an intrinsic level of uncertainty; thus, the areas that are effectively affected by a critical event may be different from the expected ones, and remotely sensed data are used to define the real condition of the transmission lines. The processed images are sent to the TSO, which evaluates the cable displacement due to ice sleeve formation, and it can update a GIS in which the real-time situation is reported. In this way, the TSO can tamely evaluate the scenario and make decisions based on the updated situation. For example, it can decide to increment the current over the affected conductors to de-ice the sleeves or sectionalise those conductors in advance so that their breakage would not result in a blackout with negative cascade effects. The sensing of the scene is made every 3 hours. In this way, it is possible to obtain up to 6-8 acquisitions of an 18-24 hours phenomenon, which is the typical length of a wet snow event. The whole system can be seen as a closed-loop control system, in which the satellites work as a sensor that gives feedback to the TSO, which acts as the controller. The controlled system is the Italian transmission line, which gets the current increment as input by the TSO, while the output is the desired effect, i.e. the ice sleeve's de-icing or line sectionalising.

5.2. Operational analysis for flood emergency response

The operational analysis for flood emergency response is much more complex compared to the one for overhead power lines monitoring because of the higher number of actors involved and the complexity of the phenomenon. The operational architecture that ex-

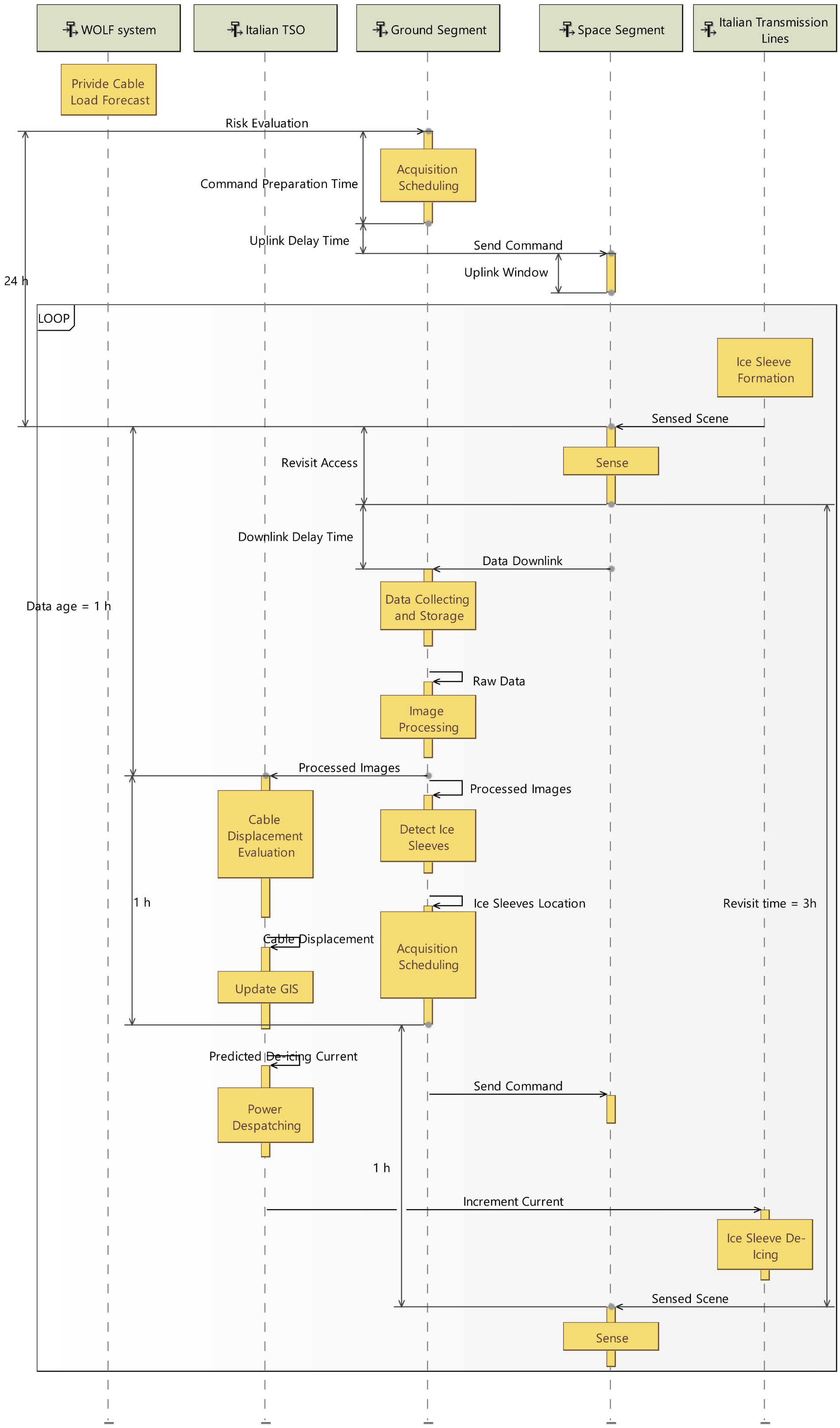

Figure 5.2: Operational scenario during an emergency due to ice sleeves accretion.

emplifies the flood emergency response capability is reported in Figure 5.3. Some of the operational entities and their activities are defined by the Civil Protection Emergency Plans [148], and they are the following:

- *The Functional Center* (Centro Funzionale Multirischi Regionale): a regional entity responsible for the weather alerting system and providing hydraulic criticality bulletins based on weather forecasting and possible risk scenarios. It accomplishes activities dedicated to forecasting, monitoring, and real-time surveillance of critical events and assessment of their effects on the territory. Thus, it operates both in a prevention phase, before the event, and in a monitoring and surveillance phase, during the event. During the monitoring and surveillance phase, its role consists of sharing information and short-term forecasts that allows confirming, updating and/or reformulating forecast scenarios according to the evolution of the event in progress. Moreover, it provides technical-scientific support to the competent authorities and operating structures responsible for emergency management. Remote sensing data can be used for this scope, together with ancillary data coming, for example, from streams and rain gauges.
- The *Operative Centre*: it is the coordination body of the Civil Protection structures during the emergency. It coordinates all the components of the Civil Protection Service, allowing the representatives of each operating function (healthcare, volunteering, telecommunications, ...) to interact directly with each other in an operating room, facilitating a collaborative decision-making process. The emergency management scheme is divided into operative functions, each one with a different competent role. Each operative function is represented in the operation room by a supervisor, pre-designated in the Civil Protection Emergency Plans. One of the most important operative functions is the technical-scientific and planning function, which coordinates all emergency management operations and performs technical support activities. It maintains the relationships between the various scientific and technical components to monitor the event and the associated risk and update the scenario based on the acquired data. The operative centre also includes a person in charge of representing the operative structures, which are, for example, the fire and rescue service (Vigili del Fuoco), the Armed Forces, the Police Forces, the structures of the National Health Service, the civil protection volunteers, the Italian Red Cross, and others. Each of them has an important operative role related to rescue and emergency response activities. For example, firefighters can help, assist and evacuate the population, while police forces can manage the traffic circulation and block roads directed to dangerous areas. Volunteers can distribute and place sandbags that

are commonly used to build a barrier that helps to stop water from getting inside vulnerable ground floor places. A multi-level organisational structure is adopted for the operative centres, based on the principle of subsidiarity, from a local level to a regional or national level, depending on the seriousness and extension of the emergency. The operative centres at different territorial levels are called: “Centro Operativo Misto” (C.C.S.), “Centro Operativo Comunale” (C.O.C.), “Centro Operativo Misto” (C.O.M.), and “Centro Operativo Regionale” (C.O.R.).

- The *District Basin Authorities*: they are public bodies that produce risk maps and identify landslide and flood hazard areas through the preparation of the PAI (Hydrogeological Plans) and PGRA (Flood Risk Management Plans). Moreover, together with the land reclamation authorities, they are responsible for managing the hydraulic structures and the opening of detention basins, which are used to accumulate water in a controlled way and protect vulnerable areas from the flood.

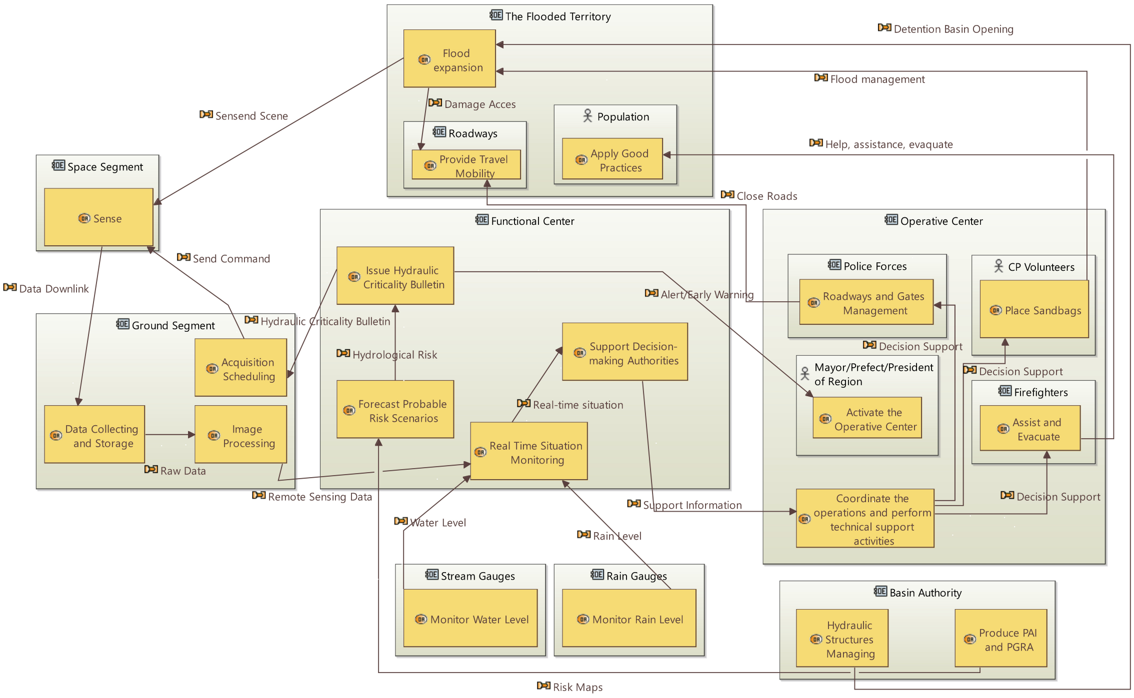

Figure 5.3: Operational architecture for flood emergency response

In this complex contest, in which many entities are involved, each one with a different role, a shared tool between them shall be used to share information and improve communication at different levels. A tool called myDEWETRA [149] has already been developed by the Italian Civil Protection with this goal. The platform includes a webGIS interface in which the situation is monitored in real-time, thanks to the employment of multiple sources, including remote sensing satellites. High revisit optical, and SAR data (also in the form of fused data) could be integrated into this platform to improve the service during an emergency.

5.3. User and system requirements

The user and system requirements for flood and critical infrastructure emergency response are reported in Tables 5.1 and 5.2. Firstly, for availability reasons, the system shall provide remotely sensed data in any condition, also during the night and with cloudy weather (UR-010). Remotely sensed data shall support the user during the emergency thanks to the following capabilities: detecting potential threats to critical infrastructure caused by ice accretion on overhead power lines (UR-020), mapping ground motion and monitoring landslides (UR-030), and performing accurate deformation measurements of transmission towers and pylons (UR-040). For this reason, SAR satellites shall be adopted (SR-010) to accomplish these tasks. Additionally, the system shall be able to identify flooded areas, map the flood extent and measure the flood depth (UR-050). These measurements can be performed both with SAR and optical data (SR-010, SR-020). Optical sensors are also adopted to provide images of high and medium-voltage towers (UR-100), identify damaged lines to perform post-disaster assessment (UR-110), and identify obstacle-free routes that can be used for emergency response (UR-120). Moreover, the system shall be able to provide synchronous optical and SAR data to improve the quality of the measurements thanks to data fusion (UR-130).

The constellation scheduling shall be done on a daily basis giving priority to the areas at risk, which are identified by the W.O.L.F. system (UR-060), and by hydraulic criticality bulletins (UR-070). In order to effectively monitor the events, the phenomena shall be monitored with a SAR sampling frequency of 3 hours (UR-080). To achieve this, 90% of the gaps between revisits shall be below 3 hours (SR-050). The coverage requirement of the SAR constellation is derived from the sizing case of the Abruzzo snowfall (which is the most demanding) and is set to 15% of the Italian territory in 12 hours (SR-030). During the event, the alert zones marked by the W.O.L.F. system represented 12-13% of the Italian territory, so the 15% coverage has been specified, adopting an extra 2-3% margin. This area shall be covered in 12 hours to detect the formation of ice sleeves in advance of possible damages. The response time of the SAR system shall be 3 hours (UR-090, SR-040) and the data age 1 hour (SR-060) to enable fast constellation rescheduling, as reported in the operational scenario in Figure 5.2. The SAR system shall also be able to provide InSAR data (SR-070) to measure small deformations of permanent scatterers, such as towers or pylons of transmission lines (UR-040), and monitor landslides that threaten critical infrastructures (UR-030). The resolution has been decided based on the state of the art of the current system and the specific needs. The SAR system and the optical systems shall have a resolution of 3 meters (SR-080, SR-090) that is enough to identify high and medium-voltage towers (UR-100), perform post-disaster assessment (UR-110), and identify obstacle-free routes that the teams of rescuers can use during the emergency response (UR-120).

It must be underlined that only some of these requirements can be verified with the optimisation tool used for this work. For example, data age and response time need to be verified with a different analysis tool. Therefore, the constellation design process results in an iterative process. The optimisation phase is the first step that allows us to find a constellation compliant with the coverage and revisit requirements while minimising the cost. After the optimisation process, a constellation shall be selected, and then the other requirements need to be verified. If some of the requirements turn out to be not compliant at a later stage of the analysis, the optimisation should be refined, or a different constellation shall be selected. Alternatively, the requirements shall be reformulated.

REQ.ID	Requirement
UR-010	The system shall be able to collect remotely sensed data in all-weather, day-and-night conditions
UR-020	The system shall be able to detect ice sleeves accretion on overhead power lines
UR-030	The system shall be able to map ground motion and monitor landslides
UR-040	The user shall be able to perform accurate deformation measurements of permanent scatterers (e.g. towers or pylons)
UR-050	The system shall be able to identify flooded areas, map their extent, and measure the flood depth
UR-060	The user shall receive remotely sensed data of the alert zones marked by the W.O.L.F. system
UR-070	The user shall receive remotely sensed data of the territory involved by a hydraulic criticality bulletin (at least yellow alert)
UR-080	The system shall be able to monitor critical events (e.g., ice sleeves formation and flood) with a sampling frequency of 3 h over the Italian territory
UR-090	Remotely sensed data shall be delivered to the user in a timely manner
UR-100	The system shall be able to provide images of high and medium voltage towers
UR-110	The system shall identify damaged lines and perform post-disaster assessment
UR-120	The system shall recognise obstacle-free routes that can be used for immediate emergency response
UR-130	The system shall provide optical and SAR synchronous fused data

Table 5.1: User requirements.

REQ.ID	Requirement	Parent reqs
SR-010	The system shall perform measurements with SAR sensors	UR-010, UR-020, UR-030, UR-040, UR-050, UR-130
SR-020	The system shall provide optical remotely sensed data	UR-050, UR-100, UR-110, UR-120, UR-130
SR-030	The SAR system shall cover 15% of the Italian territory in 12 hours	UR-060, UR-070
SR-040	The SAR system shall have a response time of 3 h over Italy	
SR-050	The 90% of the revisit time gaps shall be below 3 h over the Italian territory	UR-080
SR-060	The SAR system shall provide data with an average data age of 1 h over Italy	
SR-070	The system shall be able to provide InSAR data	UR-030, UR-040
SR-080	The SAR system shall have a resolution of 3 x 3 m (Az. x Rg.) in Stripmap mode	UR-100, UR-110, UR-120, UR-130
SR-090	The optical system shall provide VNIR images with a GSD = 3 m	UR-100, UR-110, UR-120, UR-130

Table 5.2: System requirements.

6 | Methods

6.1. High revisit mixed sensor constellation

In order to perform the constellation optimisation, some of the satellites' main characteristics shall be defined. As an assumption, each satellite has either an optical or a SAR instrument, whose main parameters are summarised in Table 6.1. In order to be compliant with the requirements, SAR satellites have a 3-meter resolution X-band planar array antenna. The swath, which depends on both the antenna beamwidth and the PRF, is 20 km in Stripmap mode, and the access angle ranges from 20° to 60°, covering both left- and right-looking directions. A SAR duty cycle of 60 seconds per orbit has been assumed for the analysis.

SAR		**Optical**	
Wavelength	3 cm (X-band)	**Spectral bands**	MS (NIR + RGB)
Polarization	Single	**Bit-depth**	12-bit
Azimuth resolution	3 m	**GSD**	3 m
Slant Rg. resolution	$<$ 3 m		
Swath	20 km	**FOV**	1.6°
Access angle	20°-60° Left and right looking	**Access angle**	<30°
Operative mode	Stipmap	**Operative mode**	Push-broom
Duty cycle	60 s/orbit		

Table 6.1: Payload parameters.

The optical sensor is equipped with a multispectral detector featuring four spectral bands, one in the near-infrared and three RGB bands. The instrument's FOV has been set to 1.6°. Therefore, the optical swath increases with the altitude of the satellite. However, if the resolution has to be maintained constant, a larger detector is required at higher altitudes. The maximum detector size, L_d, has been set to 6000 pixels, and each pixel has a size of $dp = 6\,\mu m$. Based on these assumptions, an upper boundary for the focal length, F_l, can be calculated as follows [69]:

$$F_l \tan\left(\frac{FOV}{2}\right) = \frac{L_{det}}{2}$$

that leads to a maximum focal length of $F_l = 1289\,mm$.

A GSD of 3 meters has been defined from the system requirements. However, since the GSD depends on the altitude at which the spacecraft operates, the camera's design shall be adapted based on the chosen orbit. An upper boundary for the altitude of the optical satellites has been found by using the relationship between GSD, altitude H, pixel size dp, and focal length, F_l:

$$\frac{GSD}{H} = \frac{dp}{F_l}$$

Considering the values $dp = 6\,\mu m$ and $F_l < 1289\,mm$, the maximum operative optical altitude is $H = 645\,km$. However, operating at high altitudes would require a larger focal length, increasing the instrument's cost and mass.

The maximum access angle of the optical satellites is 30°, which is a typical limit for optical imagers since higher values would introduce prospective distortions and loss of resolution due to the increasing distance from the instrument to the ground.

6.2. The optimisation tool

The optimisation process was carried out starting from a MATLAB modelling code developed during the previous works of Sartoretto [48] and Chiatante [47]. However, the code has been modified to deal with different optical-SAR constellation patterns and investigate trade-offs between the cost and the synchronous performance of the hybrid constellation. In this section, the constellation modelling tool will be described and analysed, along with its main components and assumptions. This tool is composed of three main parts:

- A function that generates the initial Keplerian elements of each satellite of the constellation, starting from the decision variables vector.
- A numerical orbit propagator that includes J_2 perturbation.
- The coverage and revisit function that computes the time instants at which each grid point representing the territory of interest is covered and revisited. Two dis-

tinct functions are used to compute respectively the SAR and the optical coverage and revisit, due to the differences in geometry between the two systems and the additional illumination constraint of the optical sensor.

6.2.1. SAR coverage and revisit function

The coverage and revisit function is used to compute the time instants at which the sensor covers or revisits the grid points with a specific latitude and longitude. Therefore, the function takes as input a matrix with the initial state of the satellites (in the form of initial Keplerian elements), propagates their position with the orbit propagator, and returns as output the time instants at which each grid point is covered or revisited. The Italian territory has been discretised in grid points with STK. In fact, from STK it is possible to obtain a matrix containing the latitudes and longitudes of each grid point representing the Italian territory, as illustrated in Figure 6.1. Two different resolutions (or point granularity) have been used; the first, with a point spacing of 8 km, is shown in Figure 6.1a, and the second one, with a spacing of 25 km, is shown in Figure 6.1b. The two grids can provide a different level of accuracy in the computation of coverage and revisit time. In this work, the 25 km grid is used for the optimisation process to reduce the computational time needed at each iteration, while the 8 km grid is used for the postprocessing of the results. This approach is called multi-fidelity and was also used in the work of Chiatante [47]

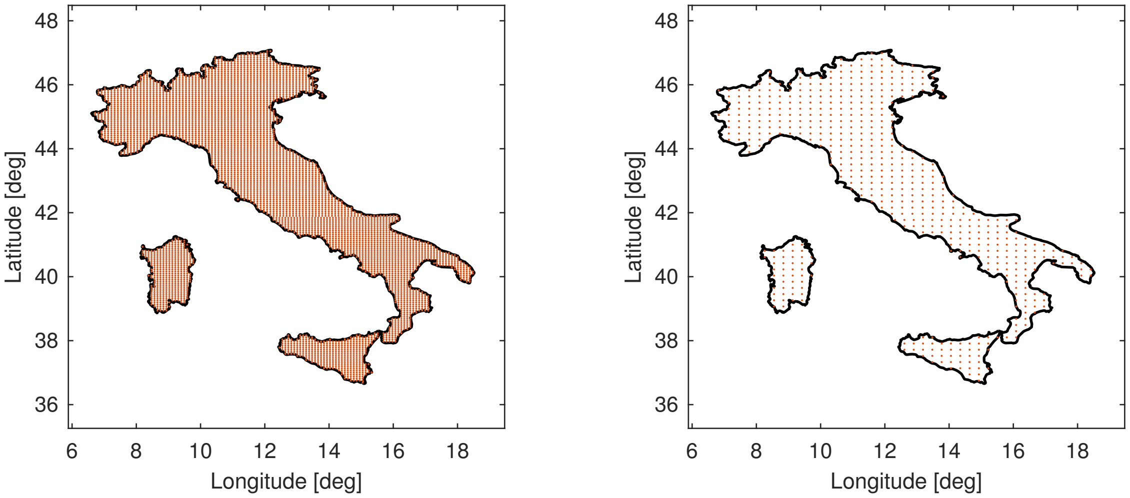

(a) Italian surface grid with 8 km spacing.

(b) Italian surface grid with 25 km spacing.

Figure 6.1: Discretised surface of Italy.

Coverage and revisit are evaluated in slightly different ways for their different definition.

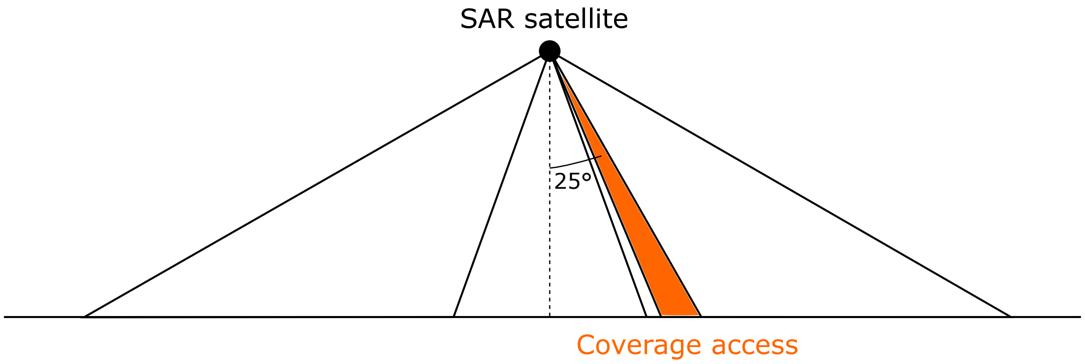

(a) Coverage geometry of the SAR instrument. A fixed look angle of 25° in the right side direction and a 20 km swath are assumed.

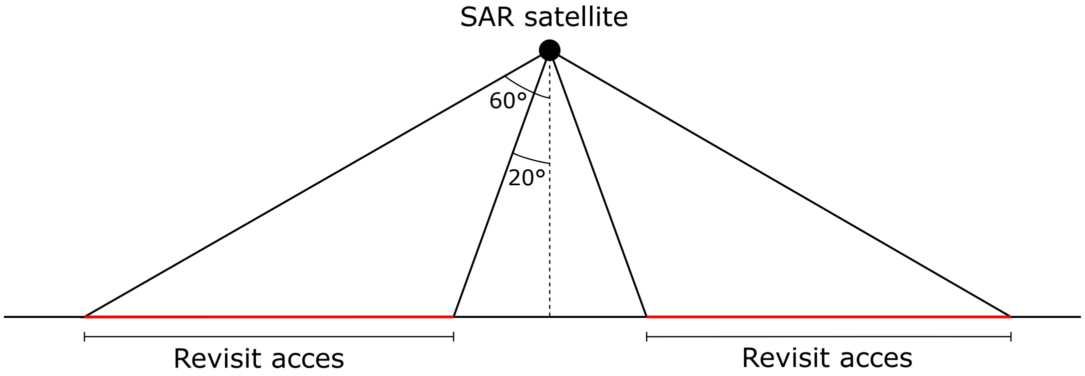

(b) Revisit geometry of the SAR instrument. An access angle between 20° and 60° is assumed, both on the left and right sides.

Figure 6.2: Revisit and coverage geometries of the SAR instrument.

In this work, coverage is evaluated assuming that the SAR instrument operates with a fixed look angle of 25° in the right side direction, considering a 20 km swath and an instrument duty cycle of 60 s per orbit. The operative mode is Stripmap, and the acquisition time is limited by the duty cycle. When a satellite passes over Italy, the instrument is consecutively switched on for 60 seconds and then turned off, limiting the maximum strip length that can be achieved. The coverage geometry for the SAR satellites is illustrated in Figure 6.2a. For revisit, an access angle between 20° and 60° is considered, both on the left and right sides, as shown in Figure 6.2b. The duty cycle is not considered for the revisit time since revisit expresses only the possibility that the instrument can potentially sense the target and not an actual acquisition.

Coverage and revisit are computed assuming a perfect sphere Earth model. After the orbit propagation, the satellite position is evaluated at each time step $t(i)$. Then, the latitude and longitude of the instrument's inner and outer swath are obtained thanks to some geometrical relationships. In this way, it is possible to obtain an acquisition rectangle that has as vertices the latitude and longitude of the inner and outer swath points evaluated at

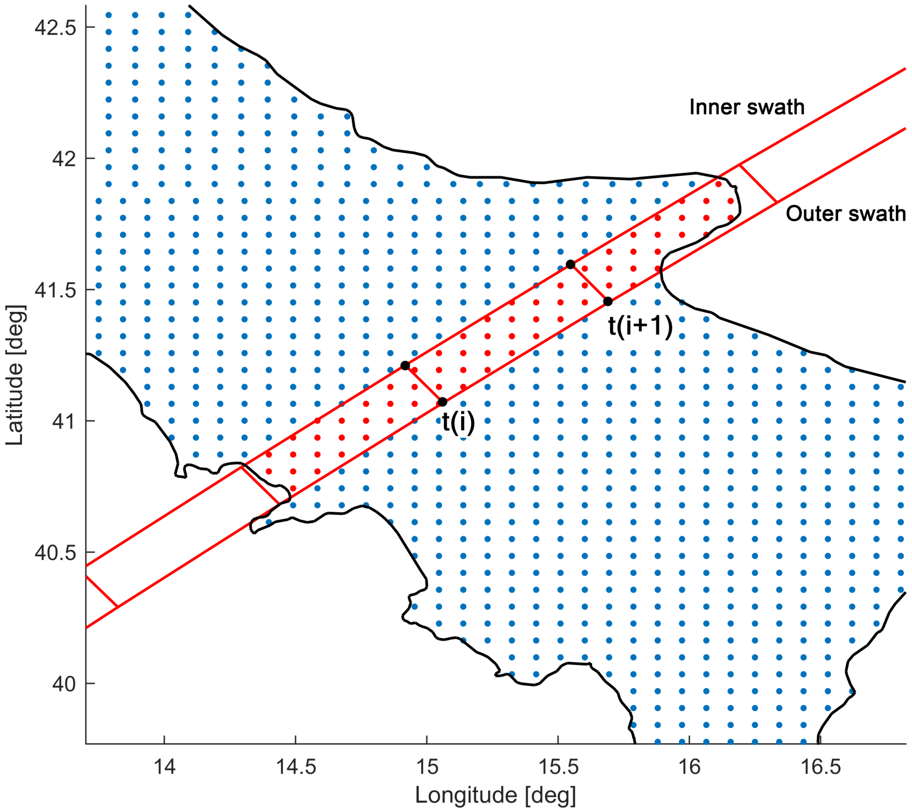

Figure 6.3: Example of SAR coverage during a pass over Italy

time $t(i)$ and $t(i+1)$, as illustrated in Figure 6.3. This procedure is done both to compute coverage and revisit, with the difference that the coverage is obtained from rectangles with a 20 km swath, while revisit is obtained from larger rectangles that represent the revisit access area. These rectangles approximate the real instrument's swath, and the evaluation accuracy increases by reducing the time step. Every time that a grid point is inside a rectangle, it is considered covered or revisited at the time instant $(t(i) + t(i+1))/2$. For each grid point, j, the revisit and coverage time instant are stored in a vector $\mathbf{t}_{rev,j}$ and $\mathbf{t}_{cov,j}$, with $j = 1, \ldots, G$, and G representing the total number of grid points. These vectors are then collected in a cell array in MATLAB.

6.2.2. Optical coverage and revisit function

The coverage and revisits of the optical instrument are computed in a very similar way to the SAR sensor. The only difference consists in the imaging geometry and in the additional illumination constraint. Moreover, the instrument duty cycle is not considered in this case, as the power consumption of optical satellites is very low, and they can be easily kept turned on during the whole overflight of Italy. The presence of clouds and smoke also influences the coverage of optical instruments; however, this factor is not considered in the analysis because of its randomness and unpredictability.

The geometry of the optical satellites is shown in Figure 6.4. Coverage and revisit access can also be identified in this case. As optical instruments have better performance when nadir pointing, coverage is computed assuming a fixed nadir-pointing direction, and the instrument's field of view is 1.6°. However, the sensor can also be pointed off-nadir, and an access angle of +/- 30° is assumed for revisits. Larger look angles would produce prospective distortions and would reduce the resolution as the target distance increases with the look angle.

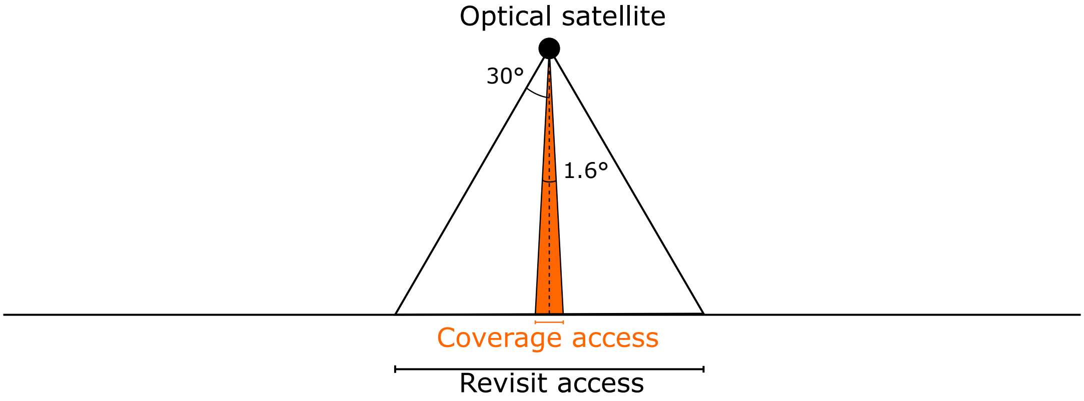

Figure 6.4: Revisit and coverage geometry of the optical instrument.

The instrument footprint is approximated by rectangles in the same way as the SAR instrument. However, a grid point inside a rectangle is considered covered or revisited only if Sun's elevation at that latitude and longitude is between 10° and 80°. This range has been assumed considering the employment of a VNIR multispectral system. In fact, the range depends on the instrument typology and its design, so it can vary. For example, thermal infrared cameras are more affected by direct sunlight with respect to visible cameras, but they can also operate without light. Moreover, the required illumination condition depends not only on the detector but also on the total amount of light that is collected by the instrument, thus on its aperture and exposure time.

6.2.3. Modelling tool validation

The MATLAB modelling tool has been validated through a comparison with the STK software. A numerical propagator that includes J_2 perturbation was employed in STK for consistency. The coverage for a SAR satellite is compared in Figure 6.5, while the coverage of an optical satellite is compared in Figure 6.6. SAR coverage resulted slightly overestimated in the MATLAB tool by approximately 4.4%. The optical coverage resulted instead underestimated in MATLAB by -0.5%. This could be due to the spherical Earth model adopted and to the sensor swath approximation adopted.

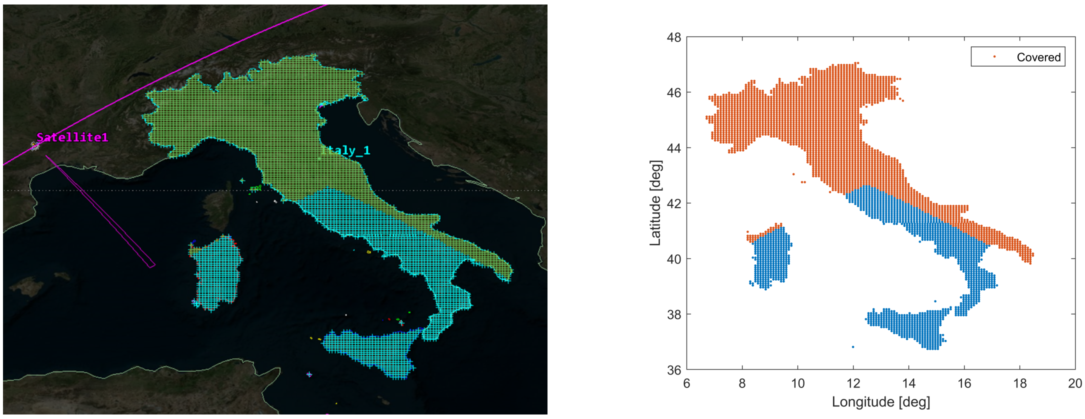

(a) SAR coverage obtained in STK. (b) SAR coverage obtained in MATLAB.

Figure 6.5: Comparison between the SAR coverage obtained in STK and MATLAB.

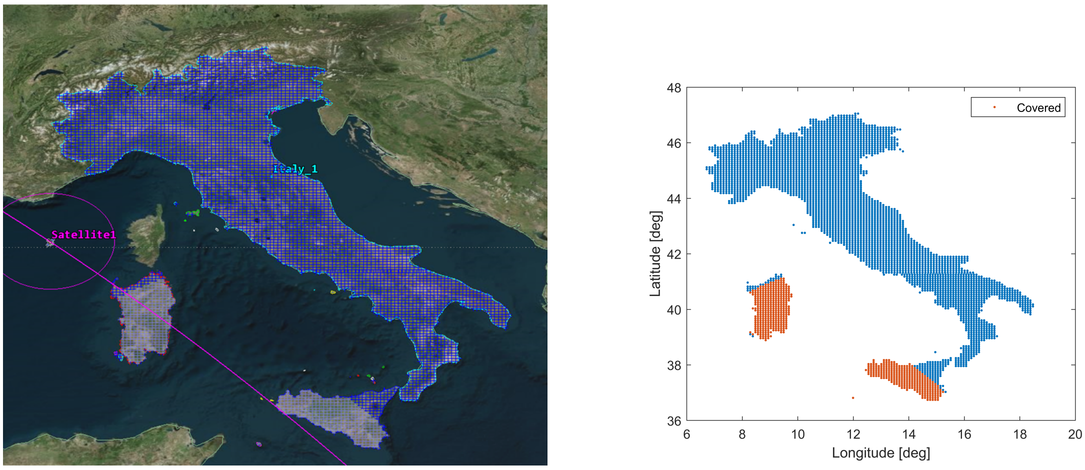

(a) Optical coverage obtained in STK. (b) Optical coverage obtained in MATLAB.

Figure 6.6: Comparison between the optical coverage obtained in STK and MATLAB.

Moreover, the revisit time instants of a SAR satellite are also compared. For example, the revisits over a random grid point are reported in Table 6.2. The differences between the revisit instants are within a 10 s interval, which was the time step adopted for the simulation. It is possible to notice that the MATLAB tool gave an additional revisit than STK. In this case, the grid point was near the border of the satellite access area; therefore, it was included in MATLAB but excluded in STK.

STK revisits	MATLAB revisits
20 Dec 2022 20:03:19	20 Dec 2022 20:03:20 (+1 s)
21 Dec 2022 21:42:55	21 Dec 2022 21:43:00 (+5 s)
22 Dec 2022 21:22:30	22 Dec 2022 21:22:30 (+0 s)
	23 Dec 2022 02:20:20
23 Dec 2022 21:02:05	23 Dec 2022 21:02:10 (+5 s)
24 Dec 2022 02:00:00	24 Dec 2022 02:00:00 (+0 s)
24 Dec 2022 20:41:41	24 Dec 2022 20:41:40 (-1 s)
25 Dec 2022 01:39:36	25 Dec 2022 01:39:40 (+4 s)

Table 6.2: SAR revisit times validation.

6.3. Mixed sensor optical-SAR constellation figures of merit

So far, the research problem regarding the design of mixed sensor constellations has only been analysed in the work of Chiatante [47], so the standard figures of merit for this kind of system have not yet been consolidated. Additionally, the conventional coverage and revisit time metrics used for standard constellations cannot be applied in this case due to the unique nature of the problem.

The fundamental concept behind a mixed sensor constellation is that the optical and SAR acquisitions should be taken within a very short time interval to enhance the reliability of the data and reduce temporal decorrelation. To achieve highly synchronous fused data, Chiatante [47] introduced a requirement for the maximum time interval between optical and SAR measurements over the same location, which he set at 60 seconds. For simplicity, we will refer to this time requirement as the *synchronicity time*. Conceptually, the synchronicity time can either be imposed as an input if the user requests a specific value, or can become an objective function to minimise, allowing the designer to study its impact on the cost of the system and other performance parameters, as done in this thesis. In fact, different levels of synchronicity may be requested by the user depending on the application.

If the same location is revisited by both sensors within the synchronicity time, this constitutes a *data fusion opportunity*, meaning that the system can potentially acquire highly synchronous data of that location. In this work, the time interval between data fusion opportunities is proposed as the first figure of merit for the performance analysis of a mixed sensor constellation. The second one is the surface of the territory of interest synchronously covered by the mixed optical-SAR sensors. These two performance parameters are referred to as the synchronous revisit time and the synchronous coverage and are further explained below.

6.3.1. The mixed sensor synchronous revisit time

The synchronous revisit time represents the system's ability to revisit a location with the two SAR and optical sensors within the synchronicity time. In other words, the synchronous revisit time is defined as the time interval between two consecutive data fusion opportunities. To better understand this concept, a possible timeline of optical and SAR revisits is shown in Figure 6.7. In the example, SAR revisits A, C, and D constitute a data fusion opportunity with optical revisits 1, 2, and 4, respectively, because the time intervals between them (ΔT_1, ΔT_2, ΔT_4) fall within the synchronicity time. Conversely, optical revisit 3 and SAR revisit D cannot form a data fusion opportunity because the time elapsed between them (ΔT_3) exceeds the synchronicity time. Thus, the synchronous revisit times are the time spans between revisits C and 1 (ΔT_1^{syn}), and 4 and C (ΔT_2^{syn}). It is worth noting that the synchronous revisit time is the time interval between two revisit pairs; hence it involves four revisits (two SAR and two optical). However, it will be computed as the time span between the second and fourth revisits, representing the moment when the fused data is effectively available. In this work, the average synchronous revisit time over the Italian territory will be analysed, which is computed by averaging the synchronous revisit times for each grid point of the territory of interest and then

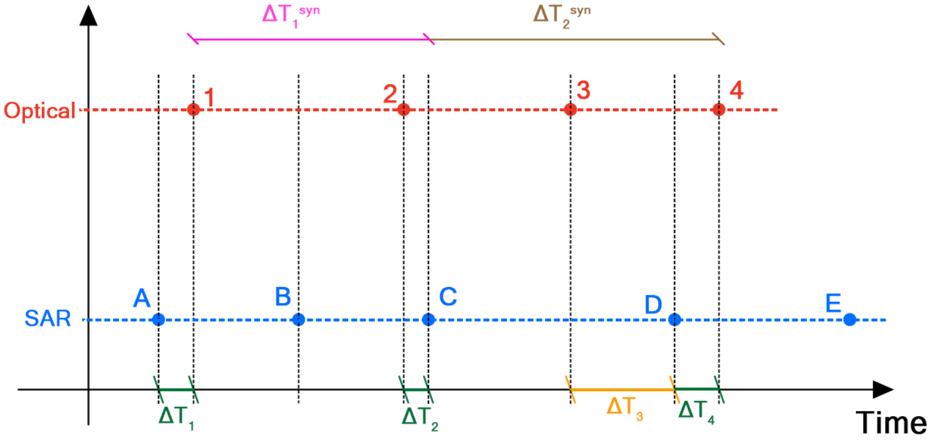

Figure 6.7: An example of SAR and optical revisits timeline. Three data fusion opportunities are potentially available, exploiting the optical revisits 1, 2, 4 (in red) with the SAR acquisitions A, C, and D (in blue). The synchronous revisit times are ΔT_1^{syn} and ΔT_2^{syn}

averaging again among all the grid points.

6.3.2. The mixed sensor synchronous coverage

The synchronous coverage is a parameter that defines the area of the territory of interest covered by the optical and SAR sensors within the synchronicity time. For this work, the daily synchronous coverage over Italy is computed, i.e. the surface of the Italian territory synchronously covered in one day.

This parameter indicates the surface that synchronous data can effectively cover, and it is influenced by the swath of the instruments, the orbital configuration, the duty cycle of the instruments, and the observation schedule. In this study, a fixed look angle is assumed for both instruments. However, this assumption is a limitation since the look angle is variable and scheduled by the operator in a real-case scenario. However, the scheduling is influenced by many factors and needs to be optimised as well, so it is quite complex to model. Therefore, the daily synchronous coverage analysed in this work can be considered an underestimated indicator of the real performance of the system, which could be actually improved by optimal scheduling.

Synchronous coverage is a new performance parameter introduced in this work. Therefore, the modelling tool previously developed by Chiatante was updated for its evaluation. The upgrade enables first to compute the time instant at which the grid points are covered by the optical instrument. Later, the optical coverage time instants are compared with the SAR coverage time instants. Hence, whenever a grid point is covered by both the optical sensor and the SAR sensor in a sufficiently short time interval (i.e. within the synchronicity time), the grid point is considered synchronously covered. In this work, the synchronous daily coverage is computed, which is the area of interest that is synchronously covered by the two sensors in 24 hours.

6.4. Problem modelling and mathematical formulation

Once the conceptual definition of the problem has been defined, the second step is devoted to the modelling and mathematical formulation of the optimisation problem [103]. That is to say, the real-world problem, with its requirements and constraints (both natural or imposed), is translated into objective functions, equality and inequality constraints, and decision variables. Therefore, the main steps for a complete formulation are:

- Characterisation of the *decision variables* and their domain.
- Definition of equality and inequality *constraints*, and definition of the parameter space (or decision space).
- Statement of the *objective functions* and their main characteristics.

The selection of the specific optimisation algorithm should be justified by the level of complexity of the problem. For instance, simpler problems can be solved with classical methods, while complex problems may require metaheuristics algorithms. In the case of constellation optimisation, the problem is rather complex since it involves both discrete and continuous decision variables, nonlinear and non-differentiable objective functions obtained by numerical integration, and nonlinear inequality constraints. Therefore, EAs are particularly suitable for these kinds of problems thanks to their flexibility. In this work, two EAs have been investigated: the NSGA-II variation included in MATLAB (i.e. the MATLAB function `gamultiobj`) and the MOEA/D algorithm. The two algorithms have been tested with a benchmark problem, i.e. the optimisation of a simple SAR constellation. As shown in Figure 6.8, the NSGA-II gave better results than MOEA/D since it tends to preserve population diversity and returns results distributed uniformly. This is because NSGA-II includes a diversity maintenance mechanism, while MOEA/D does not, so it tends to fall into local optima [45]. For this reason, only the MATLAB function `gamultiobj` will be used to optimise the optical-SAR constellation.

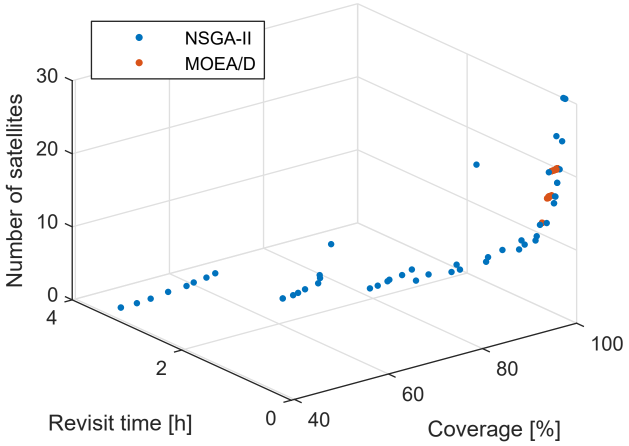

Figure 6.8: Comparison between the NSGA-II and MOEA/D algorithms in a benchmark problem. MOEA/D tends to converge toward local optima, while NSGA-II gives more uniform results and preserves diversity.

6.4.1. Constellation patterns, decision variables and domain

The optical and SAR instruments have distinct geometries, as the SAR operates as a side-looking instrument while the optical instruments are nadir-pointing. This difference is illustrated in Figure 6.9. It can be noticed that if both instruments were to be mounted on the same spacecraft, the overlapping access angle would only be 10° on both the left and right sides. Therefore, different geometries would be desirable to achieve a larger overlapping area; for example, the geometry in Figure 6.10a could be obtained thanks to a shift in the ground track between the optical and SAR satellite passage. Alternatively, the optical satellite could be positioned at a higher altitude to include a larger SAR access area, as shown in Figure 6.10b. Moreover, the optical satellites have an additional illumination constraint, i.e. the solar elevation angle over the scene.

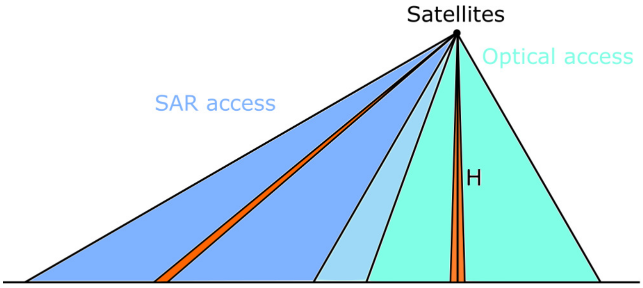

Figure 6.9: Comparison between the optical and SAR geometry. Only the left side of the SAR access angle is sketched for symmetry.

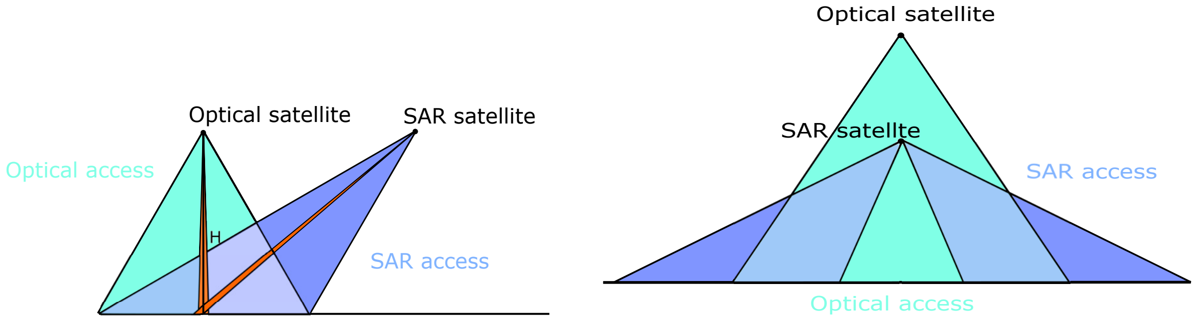

(a) The left side of the SAR access cone is overlapped with the optical one thanks to a shift in ground track.

(b) The optical satellite is at a higher altitude, so its access cone incorporates a larger portion of the access cone of the SAR.

Figure 6.10: Comparison between two different acquisition geometries.

Considering these geometries and constraints, three possible orbital patterns have been proposed:

1. Walker with Sun-synchronous orbits (or Walker SSO)

2. Walker with generally inclined orbits (or Walker inclined)
3. SAR with inclined orbits and optical with Sun-synchronous orbits (or hybrid inclined-SSO)

The first two patterns exploit a RAAN shift and an altitude difference between the optical and SAR sensor, trying to achieve a favourable acquisition geometry between the two sensors, as sketched in Figure 6.10. The third pattern employs optical satellites on SSO to take advantage of the good illumination conditions, while the SAR satellites are on generally inclined orbits to maximise the SAR coverage and revisit. Furthermore, Walker constellation patterns have been employed to simplify the problem and reduce the number of decision variables, thus shrinking the parameter space.

Walker with Sun-synchronous orbits (Walker SSO)

In the Walker constellation pattern with Sun-synchronous orbits, the optical-SAR constellation is composed of two similar Walker constellations (one optical and one SAR), both on Sun-synchronous orbits. The number of planes is the same for the two constellations, but they differ for a slight shift in RAAN. Moreover, they also have a different semi-major axis, inclinations and number of satellites per plane. An example with a 10° RAAN difference is given in Figure 6.11.

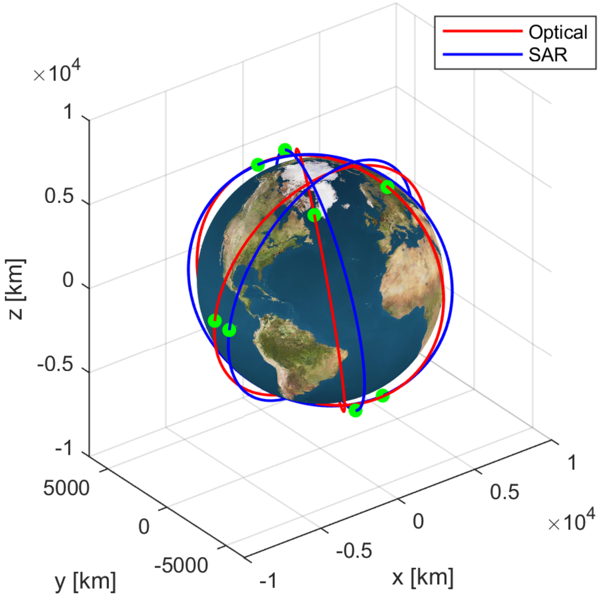

Figure 6.11: Example of a Walker constellation with Sun-synchronous orbits.

SAR and optical satellites belonging to adjacent planes are assumed to be launched together, but four manoeuvres are needed:

1. Change of altitude
2. Change of plane
3. Change of inclination
4. Orbital phasing

The change of plane manoeuvre is usually the most expensive. However, it could also be performed by exploiting the RAAN precession rate due to Earth's oblateness, but the required time could be high.

Repeating ground tracks are also exploited for their characteristics and also for reducing the decision space. Once the repeat cycle is fixed (i.e. the values of m and k), the semi-major axis, a and inclination, i, are computed by solving the system obtained from Equations (2.4) and (2.5):

$$\begin{cases} \dfrac{m}{k} = \dfrac{\omega_\oplus - \dot{\Omega}}{n + \dot{\omega} + \dot{M}_0} \\ i = \cos\left(-\dfrac{2\dot{\Omega}_{SSO} a^{7/2}(1-e^2)^2}{3R_\oplus^2 J_2 \sqrt{\mu}}\right) \end{cases}$$

For the optimisation, all the Sun-synchronous orbits for $m \in [1, 40]$ and $k \in [1, 613]$ that observe the altitude constraint are computed and stored in a matrix, as in the work of Sartoretto [48] and Chiatante [47]. In fact, there are only a finite number of SSOs with repeating ground tracks with these characteristics. In total, 312 possible orbits between 450 km and 645 km (i.e. the optical operative range) of altitude are present, and 166 orbits between 450 km and 550 km (i.e. the SAR operative range). Moreover, m and k are selected to be coprime to avoid redundancies. These orbits are stored in two matrices M_{SAR} and M_{opt} for the SAR and optical satellites. As an example, the first six rows of M_{opt} are reported in Table 6.3

For this constellation pattern, the decision variable vector is formalised as follows:

$$\boldsymbol{x} = [S_{SAR},\ S_{opt},\ P,\ F_{SAR},\ F_{opt},\ \text{index SSO}_{SAR},\ \text{index SSO}_{opt},\ \Delta\Omega,\ t_{syn}]$$

The subscript SAR and opt are used to distinguish between variables relative to the SAR and optical constellation. The parameters S_{SAR} and S_{opt} are the number of satellites for each of the P planes. F_{SAR} and F_{opt} are the Walker phasing parameters of the two

m	k	a [km]	i [deg]
1	15	6944.2	97.66
3	46	6843.2	97.27
4	59	7022.4	97.96
4	61	6868.1	97.36
5	74	7006.6	97.90
5	76	6883.1	97.42

Table 6.3: First seven rows of M_{opt} representing Sun-synchronous orbits with repeating ground tracks between 450 km and 645 km

constellations. The repeating cycle is determined by index SSO$_{SAR}$ and index SSO$_{opt}$, that identifies a row of M_{opt} and M_{SAR}. $\Delta\Omega$ is the relative RAAN shift between the optical and SAR planes, such that $\Omega_{opt} = \Omega_{SAR} + \Delta\Omega$. Finally, t_{syn} is the synchronicity time.

A lower and an upper boundary have been defined for the optimisation, such that:

$$\mathbf{lb} = [2, 2, 3, 1, 1, 1, 1, -15^\circ, 60\,\mathrm{s}]$$
$$\mathbf{ub} = [5, 5, 5, 4, 4, 166, 312, 15^\circ, 900\,\mathrm{s}]$$

With this pattern, the first seven decision variables are integer, while the last two are real.

Walker with generally inclined orbits (Walker inclined)

This configuration is similar to the previous one, with the only difference being that orbits with free inclinations are used instead of Sun-synchronous orbits, as shown as an example in Figure 6.12. Even in this case, optical and SAR satellites belonging to adjacent planes are assumed to be launched together. Even with this pattern, change of altitude, change of plane, change of inclination and orbital phasing manoeuvres are needed. For this particular configuration, the decision variables are formalised in the vector:

$$\boldsymbol{x} = [S_{SAR},\, S_{opt},\, P,\, F_{SAR},\, F_{opt},\, index_{mk},\, i_{SAR},\, a_{opt},\, \Delta\Omega,\, t_{syn}]$$

The variable $index_{mk}$ determines the repeating cycle of the SAR ground track. In fact, $index_{mk}$ is an integer value that selects the row of a matrix containing different combinations of m and k, with $m \in [1, 25]$ and $k \in [1, 383]$. The matrix contains only coprime values of m and k, avoiding redundancies. The variables i_{SAR} and a_{SAR} are the inclination and the altitude of the SAR satellites, respectively. The inclination of the optical

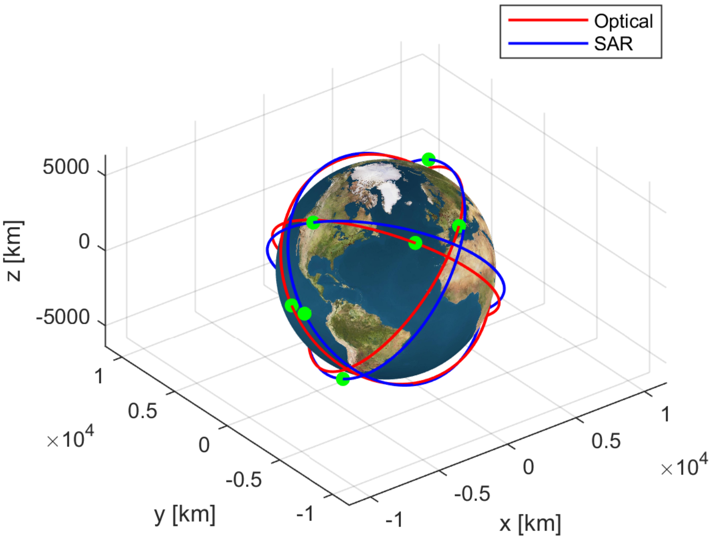

Figure 6.12: Example of a Walker constellation with inclined orbits.

satellites is imposed in such a way that they have orbits with the same nodal precession as the SAR satellites. The other decision variables are the same introduced with the Walker pattern with Sun-synchronous orbits. Even in this case, a lower and an upper boundary are defined:

$$\mathbf{lb} = [2, 2, 3, 1, 1, 1, 40^\circ, 450\,\mathrm{km}, -15^\circ, 60\,\mathrm{s}]$$

$$\mathbf{ub} = [5, 5, 5, 4, 4, 108, 89^\circ, 645\,\mathrm{km}, 15^\circ, 900\,\mathrm{s}]$$

With this pattern, the first six decision variables are integers, while the last four are real.

Hybrid inclined-SSO

In this case, the SAR constellation is a Walker with inclined planes, while the optical constellation is placed in Sun-synchronous orbits. This pattern is selected because SAR satellites on inclined orbits can provide better coverage over Italy. In contrast, optical satellites can take advantage of Sun-synchronous orbits because of the good illumination conditions. In particular, only SSOs with LTAN ranging from 8:30 to 11:00 and from 13:00 to 15:30 are considered to ensure optimal lighting conditions. In this case, optical and SAR satellites cannot be deployed with the same launcher. An example of a constellation with this pattern is shown in Figure 6.13. The decision variables are defined as follows:

$$\boldsymbol{x} = [S_{SAR},\, P_{SAR},\, F_{SAR},\, S_{opt},\, P_{opt},\, F_{opt},\, index_{mk},\, i_{SAR},\, \text{index SSO}_{opt},\, t_{syn}]$$

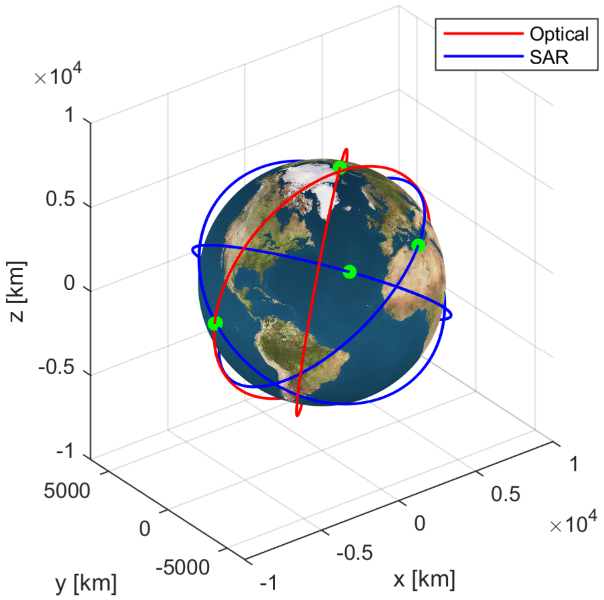

Figure 6.13: Example of a constellation in which SAR satellites are on Walker inclined orbits, while optical satellites are on Sun-synchronous orbits.

With this pattern, the number of optical and SAR planes will be different. Moreover, the SAR constellation is a Walker Delta, while the optical constellation is a modified Walker in which the planes are evenly spaced in the two LTAN ranges 8.30-11.00 and 13.00-15.30. Repeating ground tracks are also exploited.

The lower and upper boundaries are, in this case:

$$\mathbf{lb} = [2, 2, 1, 1, 2, 2, 1, 40^\circ, 1, 60\,\mathrm{s}]$$
$$\mathbf{ub} = [9, 4, 3, 9, 4, 3, 108, 89^\circ, 312, 900\,\mathrm{s}]$$

With this last pattern, the only real variables are i_{SAR} and the t_{syn}, while the others are integers.

6.4.2. Constraints

For the optimisation process, some constraints are used to reduce the decision space and avoid non-feasible solutions. The first constraint is related to the Walker phasing parameter, F:

$$F \leq P - 1$$

This constraint is observed both for the SAR and the optical constellations, and it is expressed as a linear constraint since both F and P are decision variables of the problems.

For the Walker inclined and Walker SSO configurations, a higher altitude for the optical satellites with respect to the SAR is imposed as a nonlinear constraint. In this way, optical satellites could cover a larger area of the globe, and thus also the Italian territory, possibly improving the data fusion performance. The semi-major axis is computed by the repeat cycle, m and k, and the orbit inclination, thanks to Equations (2.2), (2.4) and (2.5). The only exception is the semi-major axis of the optical satellites with inclined orbits, which is directly expressed as the decision variable x_8. Therefore, the constraint is:

$$a_{SAR} + 10\,\mathrm{km} \leq a_{opt} \leq a_{SAR} + 100\,\mathrm{km}$$

in which a maximum altitude difference of 100 km is assumed to limit the propellant required for orbit raising, as the SAR and optical satellites are assumed to be launched together. A minimum difference of 10 km is imposed to avoid intersecting planes that could increment the probability of self-collisions. This altitude constraint will not be observed for the hybrid inclined-SSO pattern since satellites are launched on planes with completely different inclinations. Moreover, the altitudes of the satellites are bounded by the constraints:

$$\begin{aligned} 450\,\mathrm{km} \leq & a_{SAR} \leq 550\,\mathrm{km} \\ 450\,\mathrm{km} \leq & a_{opt} \leq 645\,\mathrm{km} \end{aligned}$$

Additional constraints are related to the coverage in time and the revisit time of the SAR satellites. These constraints are derived from the system requirements of the constellation and are enforced by means of nonlinear constraints. Therefore, a 15% coverage of the Italian surface in 12 hours is imposed:

$$cov_{SAR} \geq 15\%$$

The computation of the coverage is made by evaluating the grid points that are covered in a 12-hour interval. However, the analysis period will be longer than 12 hours. Therefore, coverage is evaluated many times for each of the 12-hour intervals of the simulation, namely the 0-12 hours period, the 12-24 hours period and so on. In the end, the mean among the obtained coverage values is computed to obtain an overall coverage estimate for the analysis period.

The revisit time is constrained such that 90% of the SAR revisits are within 3 h:

$$rev_{90\%} \leq 3\ \mathrm{h}$$

in which $rev_{90\%}$ is the SAR 90th percentile revisit time. Finally, the SAR mean revisit time is constrained in a similar way:

$$\overline{rev} \leq 3 \text{ h}$$

Coverage and revisit are computed thanks to the coverage and revisit function described in Section 6.2.1, which gives as output the time instants at which each grid point is covered or revisited. The last three constraints related to SAR coverage and revisit are imposed as nonlinear constraints.

6.4.3. Objective functions

Five objective functions are evaluated during the analysis: the number of satellites, the launch cost, the synchronous mean revisit time, the synchronous daily coverage and the synchronicity time. Synchronous coverage and revisit are evaluated over the Italian territory. These parameters are chosen because they are the most representative of the system's cost and performance. In fact, at this stage of the design, it is important to have only a few simple performance indices, so a wide spectrum of candidate solutions can be obtained. The evaluation of other performance parameters, such as the response time, would lead to an increased computational complexity that is unnecessary at the beginning of the design. Therefore, these aspects should be investigated in a more advanced phase of the design process.

The first objective function is one of the main cost drivers, i.e. the total number of optical and SAR satellites:

$$f_1(\boldsymbol{x}) = T_{opt} + T_{SAR}$$

The second objective function is the launch cost. In this work, it is approximated in this way:

$$f_2(\boldsymbol{x}) = C \cdot N_{lnch}$$

in which N_{lnch} is the total number of launches required for the deployment, and C is the cost of a single launch, which is considered constant. In order to determine the number of launches, the launcher capacity, both in terms of mass and volume, shall be evaluated. In this work, the Vega-C launcher is selected, and a maximum capacity of $V = 9$ microsatellites [150] and a maximum launcher's payload mass $m_{max} = 2200$ kg for inclined orbit and $m_{max} = 2000kg$ for Sun-synchronous orbits are considered [151]. In order to assess the mass capacity more accurately, the performance map of Vega-C should be employed, evaluating the capacity at the specific orbit altitude and inclination.

However, since the target orbits have a bounded altitude between 450 km and 550 km, the maximum launcher's payload mass has been approximated as a constant. For the Walker inclined and the Walker SSO patterns, the number of launches is computed as follows:

$$N_{lnch} = P \cdot \text{ceil}\left(\max\left(\frac{S_{SAR}+S_{opt}}{V},\ \frac{m_{tot}}{m_{max}}\right)\right)$$

in which the total launch mass m_{tot} is the sum of the masses of each satellite.

For the hybrid inclined-SSO pattern, the total number of launches is computed as:

$$N_{lnch} = P_{SAR} \cdot \text{ceil}\left(\max\left(\frac{S_{SAR}}{V},\ \frac{m_{tot}}{m_{max}}\right)\right) + P_{opt} \cdot \text{ceil}\left(\max\left(\frac{S_{opt}}{V},\ \frac{m_{tot}}{m_{max}}\right)\right)$$

If the launcher is loaded below the full capacity, one launch per plane will be used. Otherwise, more than one launch is needed to deploy a plane. The mass of a single satellite m is the sum of the dry mass and the propellant mass:

$$m = m_{dry} + m_{prop}$$

The station-keeping propellant needed for altitude maintenance is considered since the orbital decay due to drag shall be counteracted. A two-burn Hohmann transfer is considered to estimate the required delta-V needed for station keeping. This manoeuvre is performed every 30 days over the operative life of the satellite of 5 years. Thus 60 manoeuvres are done in total. The semi-major axis rate of decay due to drag depends on the satellite's area cross-section, A, the mass, m, the drag coefficient, C_D and the air density, ρ:

$$\frac{da}{dt} = -\frac{AC_D}{m}\rho\sqrt{\mu a} \tag{6.1}$$

in which air density is estimated by an exponential air density model. The semi-major axis at the end of the 30 days, a_f, is obtained by numerically integrating Equation (6.1), and then the total delta-V needed for station keeping is:

$$\Delta V_{stkeep} = 60\left[\left(\sqrt{\frac{2\mu}{a_f} - \frac{2\mu}{a_n + a_f}} - \sqrt{\frac{\mu}{a_f}}\right) + \left(\sqrt{\frac{\mu}{a_n}} - \sqrt{\frac{2\mu}{a_n} - \frac{2\mu}{a_n + a_f}}\right)\right]$$

In addition, the delta-V required for de-orbit is computed. In fact, to be compliant with the ESA's space debris mitigation requirements, the spacecraft shall re-enter after 25 years from the end of the mission. However, since the SAR satellites are placed at an altitude below 550 km, they will naturally decay within this time span. This aspect has been verified with the ESA's DRAMA software, supposing the end of the mission on

1st January 2030. On the contrary, a mitigation strategy is needed for optical satellites orbiting at an altitude that is higher than 550 km. In this case, the perigee altitude is lowered to $r_{p,f} = 510$ km, and the disposal orbit is obtained with a single impulsive burn, with delta-V:

$$\Delta V_{EOL} = \sqrt{\frac{\mu}{a_n}} - \sqrt{\frac{2\mu}{a_n} - \frac{2\mu}{a_n + r_{p,f}}}$$

If optical and SAR satellites are launched together (i.e. when both are on SSO or generally inclined orbits), the delta-V needed by the optical satellites to transfer from the initial orbit to the final is computed. Three manoeuvres are assumed: a Hohmann transfer to rise the semi-major axis, a change of inclination and a change of plane. However, the last one can be obtained without using propellant, exploiting the differential effect due to the Earth's oblateness on the node. However, this possibility should be better assessed in terms of transfer time in a further stage of the design. The delta-V required for orbit transfer is assumed as follows:

$$\Delta V_{opt} = |\Delta V_1| + |\Delta V_2|$$

in which ΔV_1 is the delta-V required for the Hohmann transfer:

$$\Delta V_1 = \left[\left(\sqrt{\frac{2\mu}{a_{SAR}} - \frac{2\mu}{a_{opt} + a_{SAR}}} - \sqrt{\frac{\mu}{a_{SAR}}} \right) + \left(\sqrt{\frac{\mu}{a_{opt}}} - \sqrt{\frac{2\mu}{a_{opt}} - \frac{2\mu}{a_{opt} + a_{SAR}}} \right) \right]$$

and ΔV_2 is the delta-V required for the change of inclination:

$$\Delta V_2 = 2\sqrt{\frac{\mu}{a_{opt}}} \sin\left(\frac{i_{opt} - i_{SAR}}{2} \right)$$

The delta-V required for orbit phasing has not been addressed, as its entity depends on the deployment strategy and the period of the phasing orbit. The total required propellant mass is computed from the total delta-V, ΔV_{tot}, with the Tsiolkovsky equation:

$$m_{prop} = m_{dry} \left(e^{\frac{\Delta V_{tot}}{I_{sp} g_0}} - 1 \right)$$

in which I_{sp} is the specific impulse and g_0 is is standard gravity.

The last three objective functions are related to the synchronous performance of the hybrid optical-SAR constellation. They are the synchronous mean revisit time, the synchronous daily coverage and the synchronicity time:

$$\begin{aligned} f_3(\mathbf{x}) &= rev_{syn} \\ f_4(\mathbf{x}) &= (-1)\, cov_{syn} \\ f_5(\mathbf{x}) &= t_{syn} \end{aligned}$$

The synchronous revisit is obtained by comparing the revisit time instants of the two systems for each grid point. In this way, it is possible to create a new vector of the synchronous revisits that collects the time instants in which the grid points are revisited within the synchronicity time. The synchronous mean revisit time is computed by averaging the time gap between the synchronous revisits among all the grid points. The synchronous daily coverage is computed by evaluating the grid points covered within the synchronicity time during the 24 hours. If the analysis period is longer than 24 hours, the synchronous daily coverage for each day of the simulation is evaluated, and then the mean among all synchronous daily coverage values of each day is computed. Finally, all the objective functions are collected in the objective vector:

$$\mathbf{F}(\boldsymbol{x}) = \begin{bmatrix} f_1(\boldsymbol{x}) & f_2(\boldsymbol{x}) & f_3(\boldsymbol{x}) & f_4(\boldsymbol{x}) & f_5(\boldsymbol{x}) \end{bmatrix}$$

6.5. Discussion on uncertanties

The problem related to the uncertainties of the optimisation process can be divided into two main categories, including:

- Uncertainties in the modelling tool: this concerns the uncertainties associated with the mathematical models used to represent the system, such as the uncertainty of the orbital propagation model and the uncertainty of the coverage and revisit calculation model.
- Uncertainties related to the optimisation algorithm adopted.

As far as the orbit propagator is concerned, the errors derive from the perturbation model adopted and from the numerical integration error. However, the numerical error can be easily mitigated by imposing a small tolerance of the ordinary differential equation (ODE) solver. Moreover, analytical or semi-analytical propagators can also be implemented, but they are far less accurate than numerical ones [53]. On the contrary, an accurate perturbation model can be slightly more difficult to implement. In the altitude ranges investigated in this thesis, the predominant perturbation is the acceleration due to Earth's oblateness J_2. In fact, at $H \approx 500\,\text{km}$ the main accelerations are [152]:

- Acceleration due to Earth's oblateness J_2: $a_p \approx 10^{-2} g_0$.
- Higher-order accelerations due to Earth's oblateness: $a_p < 10^{-5} g_0$.
- Accelerations due to solar and lunar gravity: $a_p < 10^{-7} g_0$.
- Solar radiation pressure (SRP): depending on the area-to-mass ratio, $a_p \approx 10^{-9} g_0$.
- Drag: depending on the area-to-mass ratio, $a_p \approx 10^{-9} g_0$.

Moreover, each perturbative force can have secular and/or periodic effects. In particular, long-term secular variations are generated by even zonal harmonics, SRP, drag and third-body perturbations of the Sun and Moon [53]. However, these effects will be neglected as the analysis period will be short, and only J_2 perturbation is included as it is the most relevant. Another source of uncertainties derives from the coverage and revisit model. For example, uncertainties could arise from the instrument model that has been implemented. This aspect has been investigated in this thesis since the adopted model was validated through STK. In addition, coverage can be influenced by the grid spacing, the simulation time step and the time span employed for the analysis. More accurate models are computationally expensive and can significantly slow down the optimisation process. Nevertheless, since the proposed tool should serve at the early stages of the design, an approximated model can be very beneficial to explore a larger number of candidate solutions. Therefore, a more accurate model could be implemented at a second stage to refine the results and better evaluate the performance of the selected constellations.

Uncertainty can also arise from the adopted optimisation algorithm. Evolutionary algorithms are flexible tools that allow addressing complex problems such as constellation design, which involves both real and integers decision variables, nonlinear and non-differentiable objective functions obtained by numerical integration, and nonlinear inequality constraints. However, evolutionary algorithms offer a stochastic search approach and do not guarantee convergence to the global optimum. In fact, different runs of the algorithm can lead to different solutions. To face this problem, a greater number of iterations can allow us to explore more solutions and give better results. However, an excessive number of iterations may cause high utilisation of temporal and computational resources. Alternatively, the search space can be reduced thanks to some constraints. Moreover, different evolutionary algorithms can be explored and tested with benchmark problems, as done in this thesis with the NSGA-II and the MOEA/D. The quality of a set of solutions could also be addressed with metrics such as the hypervolume [153], which indicates the convergence and diversity of the solution set.

All these uncertainties source contribute to the total optimisation uncertainty. For example, if the coverage is overestimated, this could result in underestimating the required number of satellites. Vice versa, if the coverage is underestimated, the obtained constellation would be oversized to respect the requirements. However, the overall uncertainty associated with the optimisation problem should be further investigated by analysing the sensitivity of the results to different settings.

6.6. Workstation and optimisation time

The optimisation has been performed with a 16 cores workstation with the specifics shown in Table 6.4. Regarding the setting of the genetic algorithm, the population size is set to 750 individuals and the maximum number of iterations to 50. The optimisation time is equal to 24 hours for the Sun-synchronous Wlaker pattern, 30 hours for the Walker inclined pattern, and 44 hours for the hybrid inclined-SSO pattern.

OS	Ubuntu 18.04
CPU	Intel(R) Xeon(R) Gold 5217 @ 3.00 GHz
Cores	Physical 16 / Logical 32
Gpu	2xNvidia RTX6000
VRAM	2x24 GB
RAM	442 GB

Table 6.4: Workstation specifics.

6.7. Summary of optimisation input

The main input for the optimisation is reported in Table 6.5. Coverage and revisits are evaluated over the Italian territory.

Variable	**Value**
Simulation period	5 days
Time step	10 s
Starting day of simulation	21 Sep. 2022
SAR coverage	<15% in 12 h
SAR mean revisit time	< 3 h
SAR 90th percentile revisit time	< 3 h
Grid spacing	25 km
SAR satellite's dry mass	160 kg
SAR satellite's operational lifecycle	5 years
SAR satellite's specific impulse	230 s
SAR satellite's area cross-section	$1.1\,\mathrm{m}^2$
SAR duty cycle	60 s
SAR swath	20 km
SAR access angles	20°-60° (left- and right-looking)
SAR altitude range	450-550 km
Optical satellite's dry mass	145 kg
Optical satellite's operational lifecycle	5 years
Optical satellite's specific impulse	230 s
Optical satellite's area cross-section	$0.7\,\mathrm{m}^2$
Illumination constraint	SZA = [10°, 80°]
Optical FOV	1.6°
Optical FOR	+/- 30°
Optical altitude range	450-645 km
Launch cost	37 M$ per launch
Launch capacity	9 satellites
Maximum launch mass	Inclined obits: 2200 kg SSO orbits: 2000 kg
Territory of interest	Italy

Table 6.5: Optimisation inputs

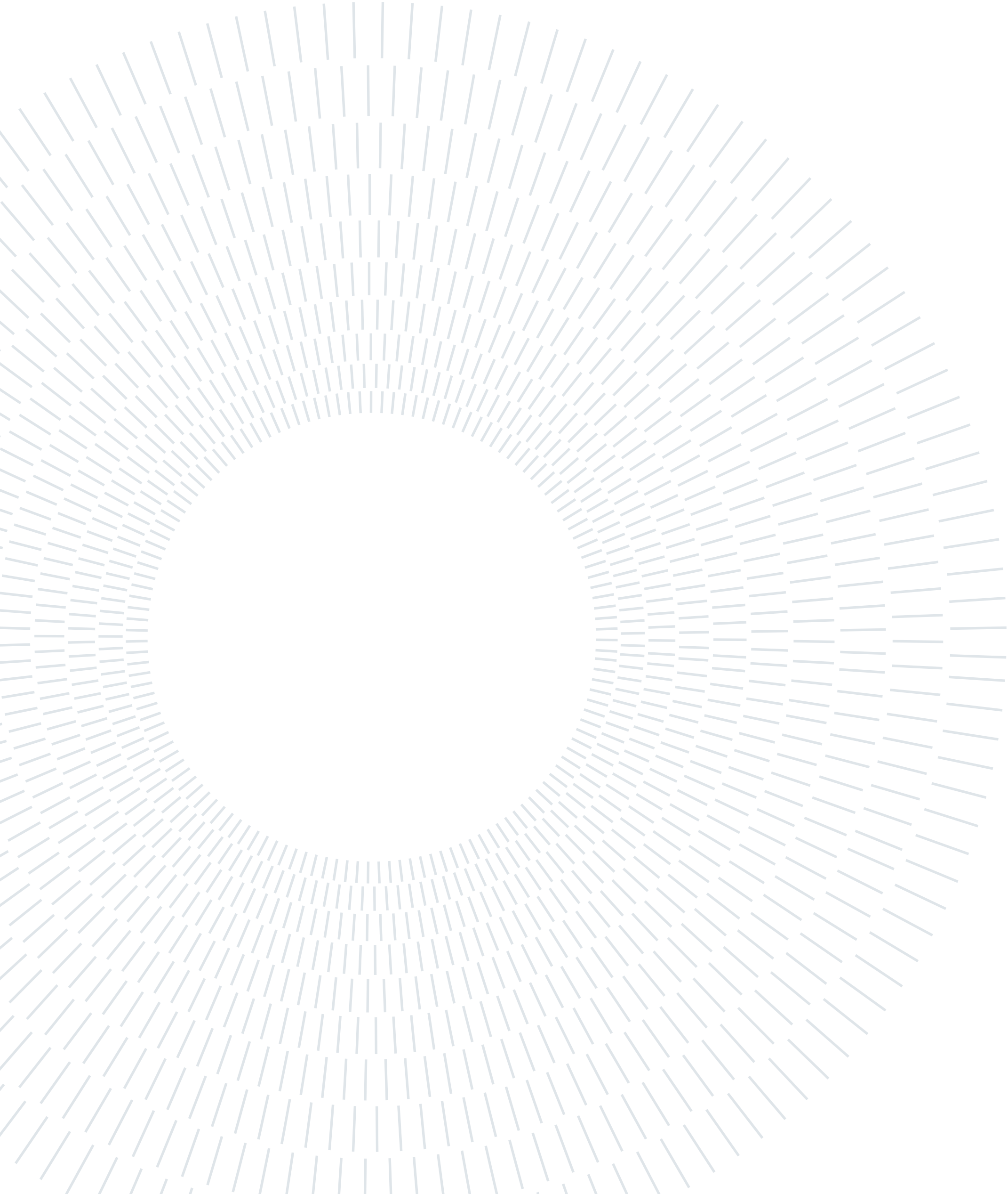

7 | Results

In this chapter, the results obtained from the optimisation process are reported. The optimisation has been carried out by evaluating the performance of the constellation on the territory of interest, namely the Italian territory. The three different orbital patterns will be presented and discussed: Walker inclined, Walker SSO, and hybrid inclined-SSO. The optimisation has been performed by discretising the territory of interest in grid points with a spacing of 25 km, and the state of each satellite is evaluated with a time step of 10 s. The starting day of the simulation is September 21, 2022, and the simulation period is 5 days. In order to perform post-processing, the candidate solutions are again evaluated by implementing a more refined grid with 8 km spacing and the time step is reduced to 5 s. Moreover, the simulation period is increased to 15 days. At the end of this chapter, five designs will be selected and analysed in more detail.

7.1. Generally inclined orbits (Walker inclined)

The set of nondominated solutions (or Pareto front) generated by the optimisation process with generally inclined orbits is shown in Figure 7.1. In total, 263 solutions have been generated. In order to visualise the five-dimensional objective space, two 3D scatter plots are used, each representing four dimensions. The left scatter plot in Figure 7.1 illustrates the total number of satellites (f_1), the launch cost (f_2), the synchronous mean revisit time (f_3), and the synchronicity time (f_5). In the right scatter plot, the synchronous revisit time is substituted by the daily synchronous coverage (f_4). It is possible to notice how the number of satellites and the synchronicity time has an impact on both the synchronous revisit time and the synchronous coverage. Moreover, larger and more performing constellations also require a higher launch cost.

The trade-off between the total number of satellites (i.e. the sum of SAR plus optical satellites) and the synchronous performance is also reported in Figure 7.2. In particular, in Figure 7.2a is shown the relation between the number of satellites and the synchronous mean revisit time, while in Figure 7.2b is illustrated the compromise between the number of satellites and the synchronous coverage. Both the synchronous mean revisit time and

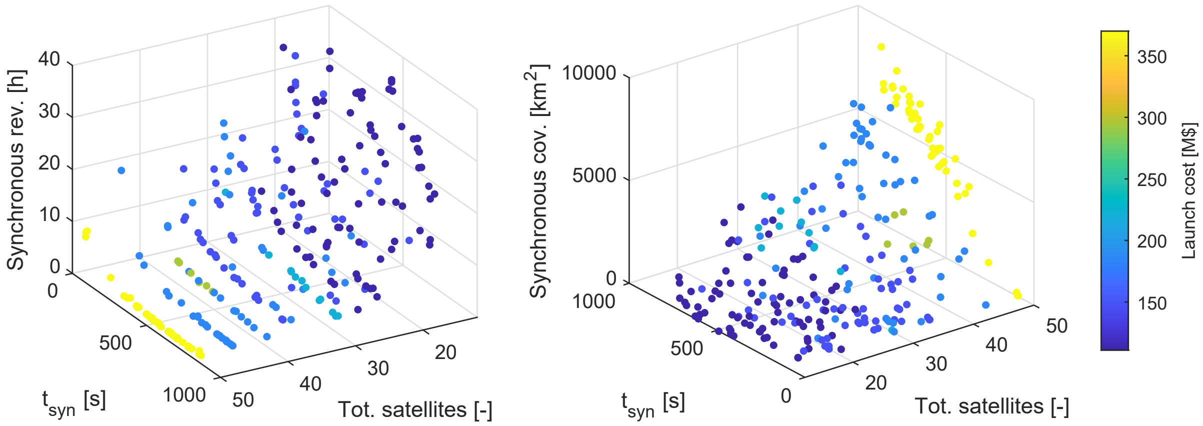

Figure 7.1: Pareto front of the hybrid optical-SAR constellation designs with Walker inclined pattern. The left scatter plot illustrates the total number of satellites (f_1), the launch cost (f_2), the synchronous mean revisit time (f_3), and the synchronicity time (f_5). The right scatter plot has on the z-axis the daily synchronous coverage (f_4) in place of the synchronous mean revisit time.

the synchronous coverage improve with a higher number of satellites since a larger constellation implies more frequent revisits and more extended coverage. It is also possible to notice how the synchronicity time t_{syn} strongly influences the synchronous coverage and revisit. This is because achieving a SAR and an optical acquisition within a very short time interval is more unlikely than having them within a more extended period.

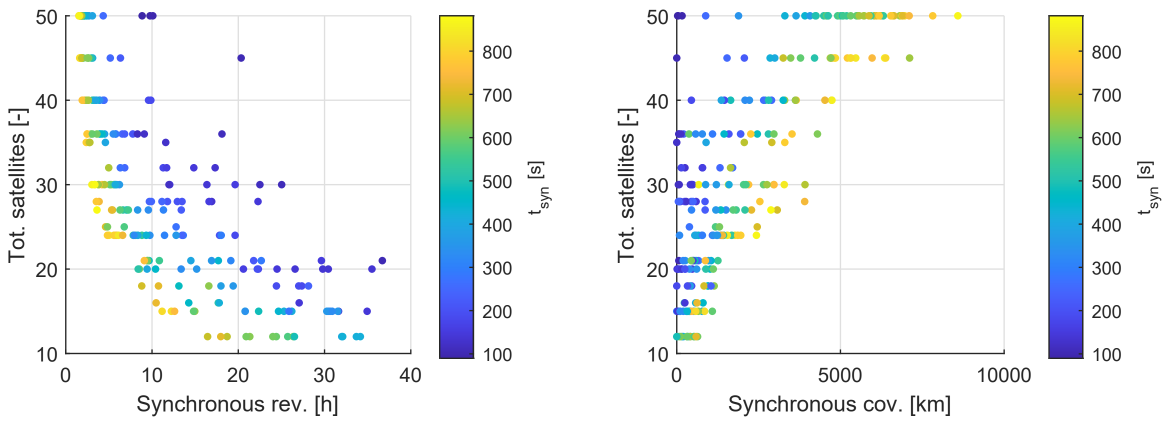

(a) Trade-off between the number of satellites, the synchronous mean revisit time and the synchronicity time).

(b) Trade-off between the number of satellites, the synchronous daily coverage and the synchronicity time.

Figure 7.2: Trade-off between the total number of satellites and synchronous performance (Walker inclined).

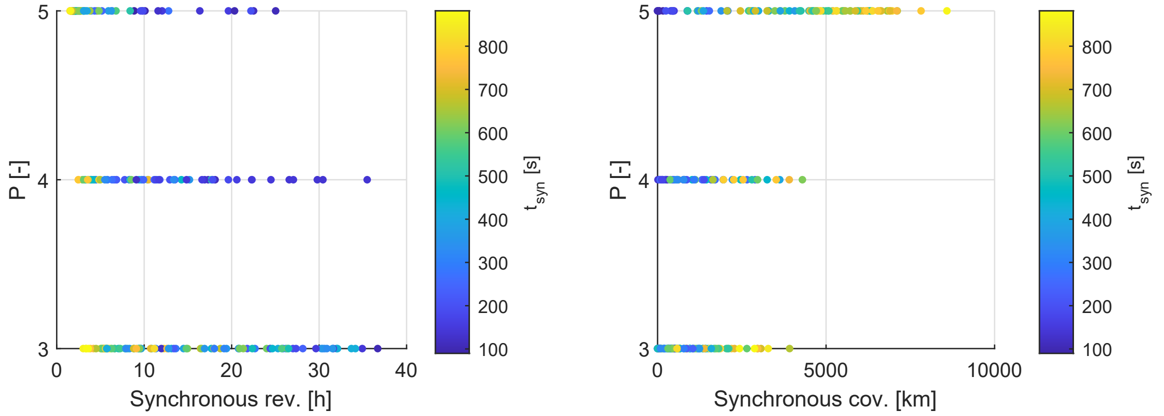

(a) Trade-off between the number of planes, synchronous mean revisit time and synchronicity time.

(b) Trade-off between the number of planes, synchronous daily coverage and synchronicity time.

Figure 7.3: Trade-off between the number of planes and the synchronous performance (Walker inclined).

The trade-off between the number of planes and the synchronous performance is reported in Figure 7.3. We recall that the variable P represents only the number of either optical or SAR planes and that the optical and SAR sub-constellations have an equal number of planes. Therefore, the total number of planes of the full optical-SAR constellation is actually $2P$. In Figure 7.3a is shown the relationship between the number of planes, the synchronous mean revisit time and synchronicity time. On the contrary, in Figure 7.3b, the synchronous daily coverage is analysed. Constellations with a higher number of planes can achieve both better synchronous coverage and revisit. However, the launch cost is mostly related to the number of planes, as reported in Figure 7.4, and solutions with fewer planes are the most cost-effective. Moreover, launch cost also depends on the number of satellites, as two launches per plane would be required if the launcher capacity is saturated. These results are valid for the Vega-C launcher, but different results would be obtained assuming a different launcher.

Some of the constellation parameters that are peculiar to this kind of constellation pattern are also investigated, namely the RAAN shift $\Delta\Omega$, and the altitude ratio between the optical and SAR orbits. It can be noticed from the histogram in Figure 7.5a that the majority of optimal solutions have a RAAN shift between -8.5° and -7.5°, while there are only two solutions in the range of -4° and 4°. Therefore, a RAAN shift between the optical and SAR planes seems to be favourable in terms of synchronous performance since the selection mechanism of the genetic algorithm tends to prefer solutions with this characteristic. However, it is essential to mention that achieving this RAAN difference

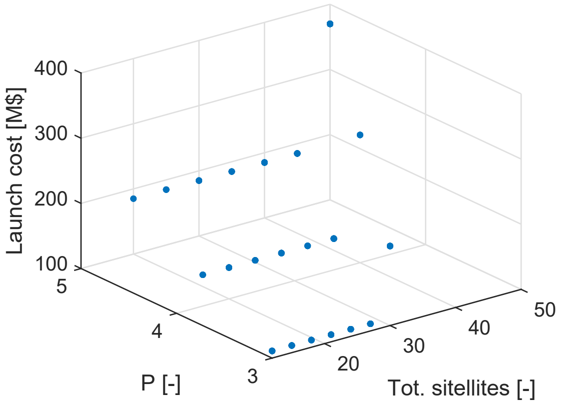

Figure 7.4: Launch cost as a function of the number of planes and the number of satellites (Walker inclined).

comes with a high cost regarding the required delta-V or transfer time, depending on the deployment strategy adopted. This cost has not been considered in this work; therefore, the feasibility of the change of plane manoeuvre should be better assessed in a more advanced design phase.

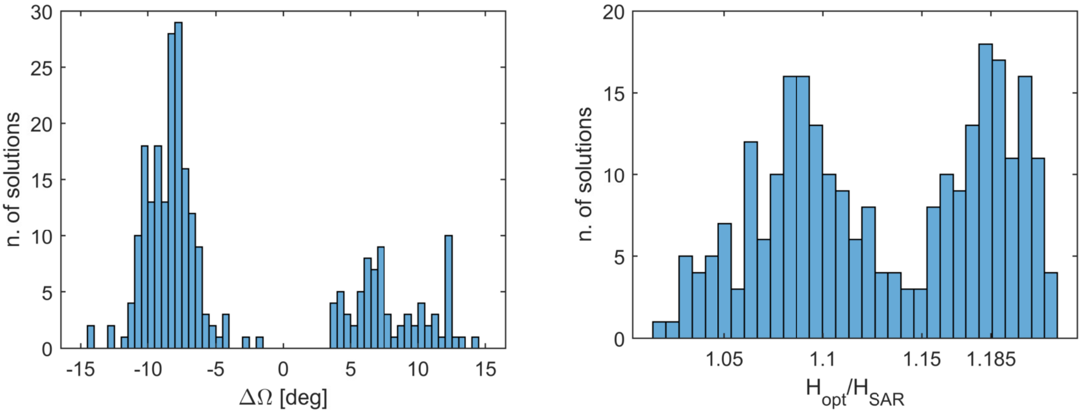

(a) Histogram representing the distribution of RAAN shift between optical and SAR planes.

(b) Histogram representing the the distribution of altitude ratio between the optical and SAR orbits.

Figure 7.5: Histograms representing the distribution of RAAN shift and altitude ratio between the optical and SAR orbits (Walker inclined).

In Figure 7.5b, it is shown the number of solutions for different optical-SAR altitude ratios (H_{opt}/H_{SAR}). When $H_{opt}/H_{SAR} \approx 1.185$, the access swath of the optical satellites and the lateral access swath of the SAR satellites assume the same value, maximising the overlapped area. This ratio is derived from the relationship:

$$2H_{opt}\tan\left(\frac{FOR}{2}\right) = H_{SAR}\left(\tan\theta_i^{max} - \tan\theta_i^{min}\right)$$

where $FOR = 60^\circ$ is the optical field of regard, $\theta_i^{max} = 60^\circ$, and $\theta_i^{min} = 20^\circ$ are the maximum and maximum SAR access angles. It is possible to notice from Figure 7.5b how this particular ratio seems favourable since many solutions close to this value have been obtained. However, solutions with smaller altitude differences are also present, particularly when the ratio is near 1.08-1.09. Designs with a smaller altitude difference can be preferred because they require less propellant for the orbital raising. However, if the altitudes of the optical and SAR constellations become too similar, the probability of self-collisions can increment.

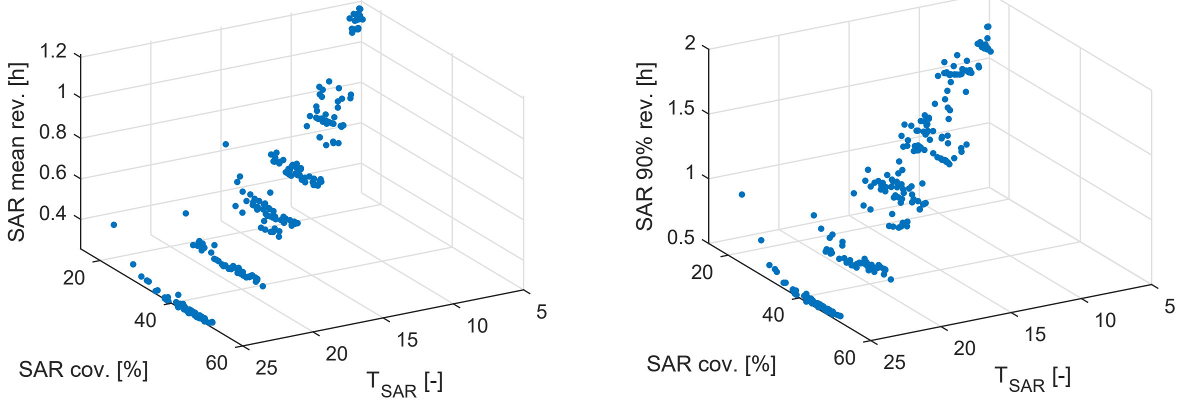

(a) SAR mean revisit time as a function of the SAR coverage in 12 h and the number of SAR satellites.

(b) SAR 90th percentile revisit time as a function of the SAR coverage in 12 h and the number of SAR satellites.

Figure 7.6: Scatter plots of the SAR performance vs number of SAR satellites (Walker inclined).

The performances of the SAR constellation as a function of the number of SAR satellites are reported in Figure 7.6. It is important to recall that the SAR performances were imposed as optimisation constraints, so they are not objective functions of the problem. Therefore, even if the scatter plots in Figure 7.6 could resemble the representation of a Pareto front, it cannot be considered as an actual Pareto front. However, the synchronous performances are related to the performances of the SAR constellation, and also the cost drivers depend on the number of SAR satellites. In other words, the objective functions also depend on the SAR constellation performanc and cost. Figure 7.6a shows the SAR mean revisit time as a function of the SAR coverage in 12 h and the number of SAR satellites. Figure 7.6b shows the SAR 90th percentile revisit time as a function of the

SAR coverage in 12 h and the number of SAR satellites.

The frequency of SAR inclinations among the solutions is investigated in Figure 7.7. Most of the designs have inclinations between 46° and 56°. This result is in line with the research of Chiatante [47] and Sartoretto [48], which also studied the coverage problem over the Italian territory. Indeed, it is possible to minimise the number of satellites by placing them in orbit with an inclination a few degrees higher than the latitude of the target of interest [47], [55].

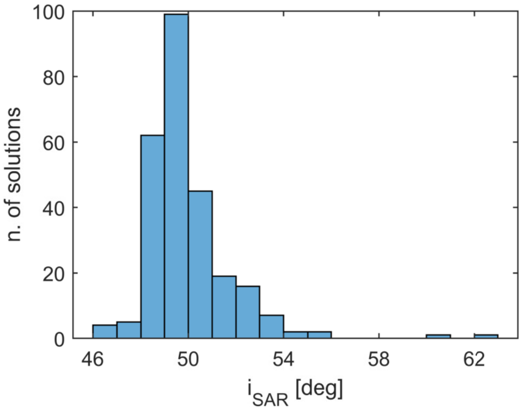

Figure 7.7: Histogram representing the distribution of SAR inclinations (Walker inclined).

7.2. Sun-syncrhonous orbits (Walker SSO)

The Pareto set generated by the optimisation process with Sun-synchronous orbits is shown in Figure 7.8. Even in this case, 263 solutions have been generated. Similar trade-offs can be observed between the number of satellites, the synchronicity time, the synchronous mean revisit time, the synchronous daily coverage and the launch cost. Nevertheless, in this case, the performances are generally worse than those in Figure 7.1, relatives to the Walker inclined case.

In Figure 7.9a is shown the relation between the number of satellites and the synchronous mean revisit time, such that a larger constellation implies a lower synchronous revisit. In Figure 7.9b is illustrated the compromise between the number of satellites and the synchronous coverage, showing that synchronous coverage increases with the number of satellites. In this case, synchronicity time t_{syn} strongly influences the synchronous mean revisit time, but seems to have a weaker impact on the synchronous coverage.

The trade-off between the number of planes and the synchronous performance is reported in Figure 7.10. It is possible to notice that only orbits with $P = 4$ or $P = 5$ are found. However, constellations with $P = 5$ achieve better synchronous coverage and revisit time

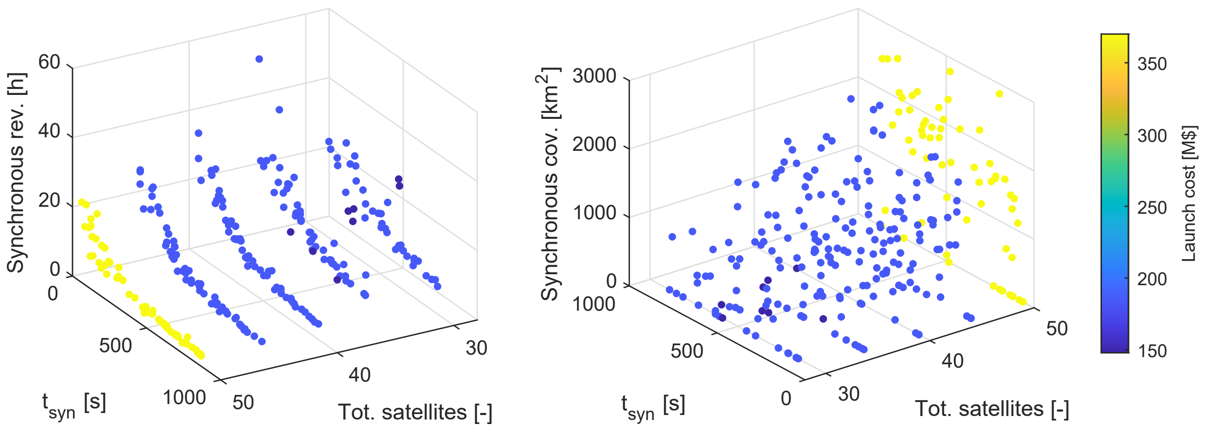

Figure 7.8: Pareto front of the hybrid optical-SAR constellation designs with Sun-synchronous orbits. The left scatter plot illustrates the total number of satellites (f_1), the launch cost (f_2), the synchronous mean revisit time (f_3), and the synchronicity time (f_5). The right scatter plot has on the z-axis the daily synchronous coverage (f_4) in place of the synchronous mean revisit time.

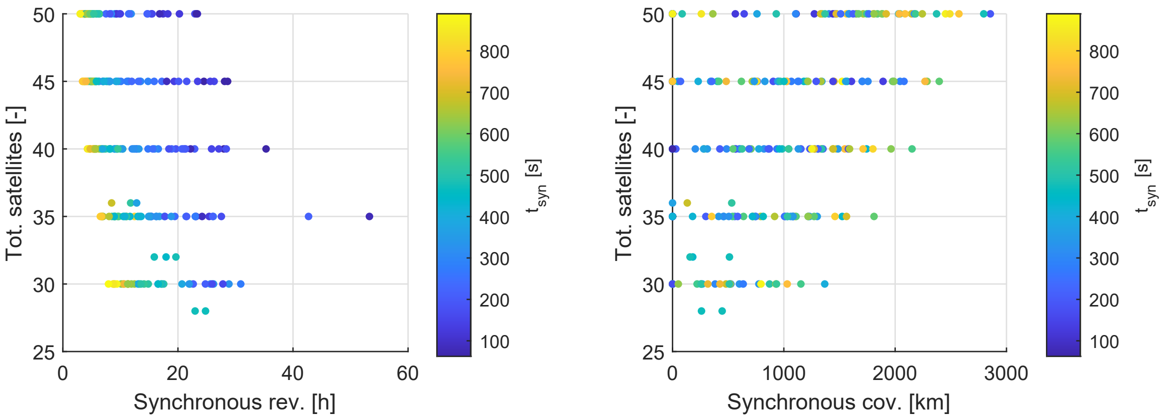

(a) Trade-off between the number of satellites, the synchronous mean revisit time and the synchronicity time.

(b) Trade-off between the number of satellites, the synchronous daily coverage and the synchronicity time.

Figure 7.9: Trade-off between the total number of satellites and synchronous performance (Walker SSO).

than constellations with $P = 4$. The trade-off between launch cost, number of planes and number of satellites is reported in Figure 7.11. In this case, launch costs are higher than inclined orbits because at least four launches are needed.

The RAAN shift between the optical and SAR planes, $\Delta\Omega$, seems favourable also in this case. In fact, as shown in Figure 7.12a, the majority of optimal solutions have a RAAN shift between -5° and -4°, while there are only two solutions in the range of -2° and 2°.

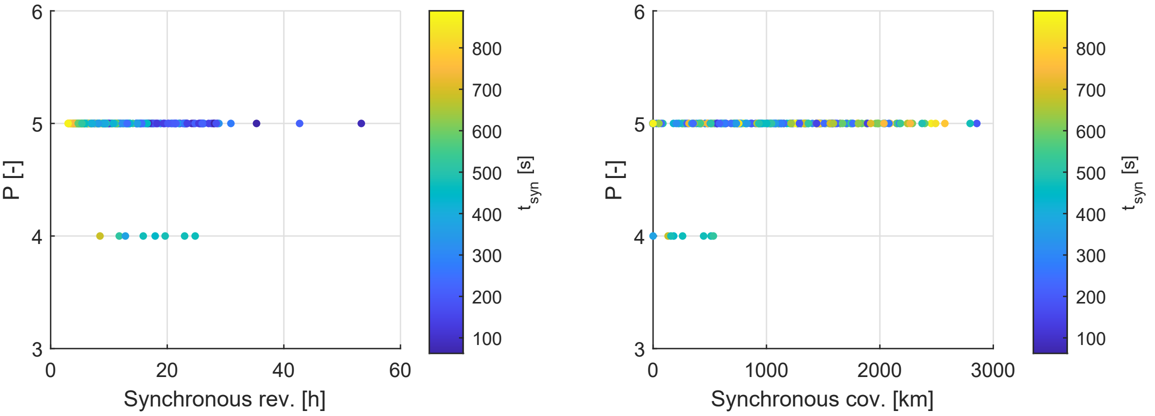

(a) Trade-off between the number of planes, synchronous mean revisit time and synchronicity time.

(b) Trade-off between the number of planes, synchronous daily coverage and synchronicity time.

Figure 7.10: Trade-off between the number of planes and the synchronous performance (Walker SSO).

On the contrary, the distribution of altitude ratios, H_{opt}/H_{SAR}, is more uniform than the Walker inclined pattern, as shown in Figure 7.12b.

The performances of the SAR constellation as a function of the number of SAR satellites are reported in Figure 7.13. To be compliant with the constraints, the Sun-synchronous orbits require a higher number of SAR satellites than the inclined orbits. Hence, only solutions with 5 satellites on 4 planes, or 4 to 5 satellites on 5 planes, have been found. On the contrary, in the inclined case solutions with only three SAR planes exist.

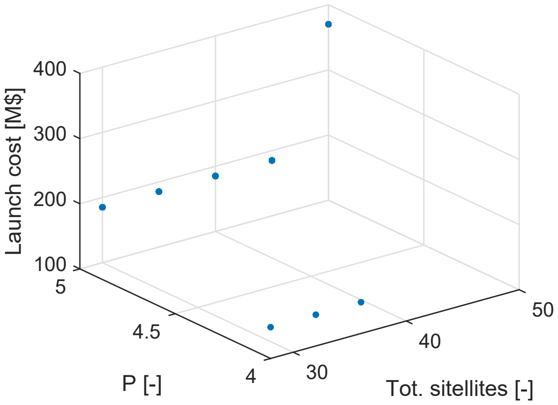

Figure 7.11: Launch cost as a function of the number of planes and the number of satellites (Walker SSO).

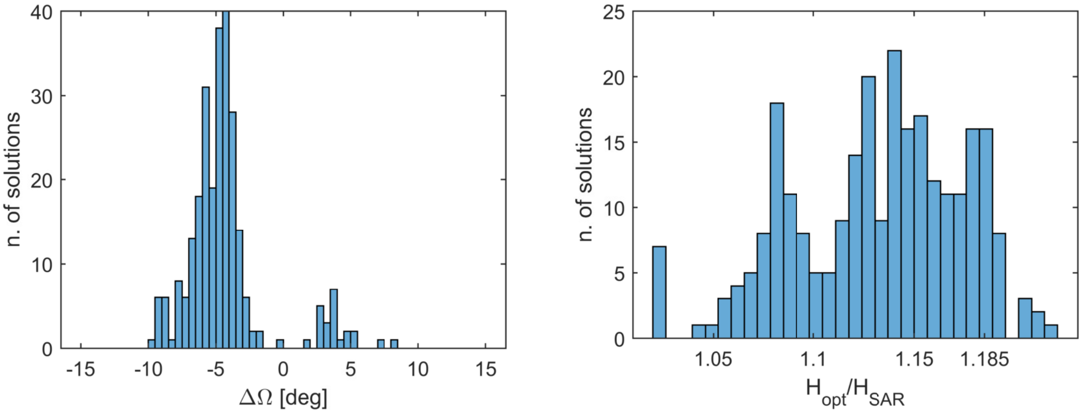

(a) Histogram representing the distribution of RAAN shift between optical and SAR planes.

(b) Histogram representing the the distribution of altitude ratio between the optical and SAR orbits.

Figure 7.12: Histograms representing the distribution of RAAN shift and altitude ratio between the optical and SAR orbits (Walker SSO).

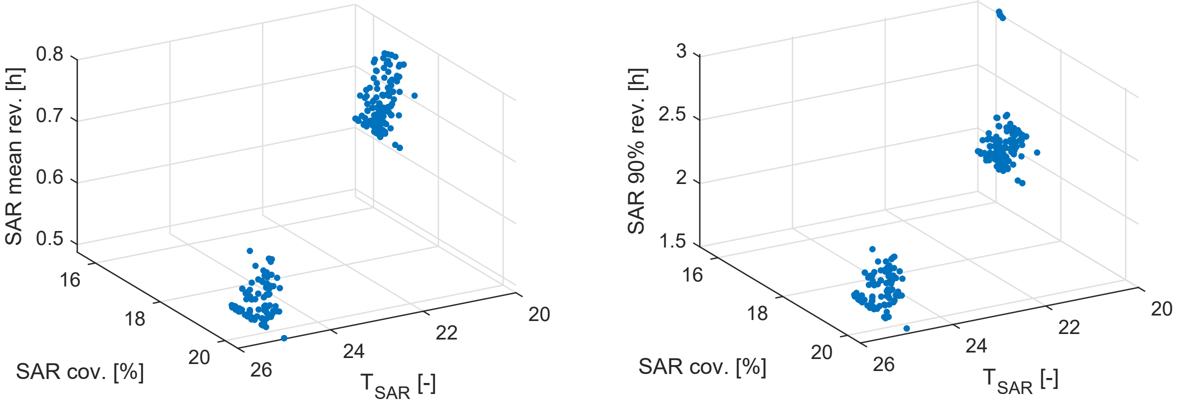

(a) SAR mean revisit time as a function of the SAR coverage in 12 h and the number of SAR satellites (Walker SSO).

(b) SAR 90th percentile revisit time as a function of the SAR coverage in 12 h and the number of SAR satellites.

Figure 7.13: Scatter plots of the SAR performance vs number of SAR satellites (Walker SSO).

7.3. Hybrid inclined-SSO orbits

The Pareto set generated by the optimisation process with optical satellites on Sun-synchronous orbits and SAR satellites on generally inclined orbits is shown in Figure 7.14. The total number of generated solutions is 263. The compromises observed in the previous two cases are also confirmed with this constellation pattern. However, the best synchronous performance remains the one found in the first case shown in Figure 7.1. Nevertheless, the optical satellites placed on SSO orbits can be more valuable for their ability to provide observations with consistent illumination conditions during the time.

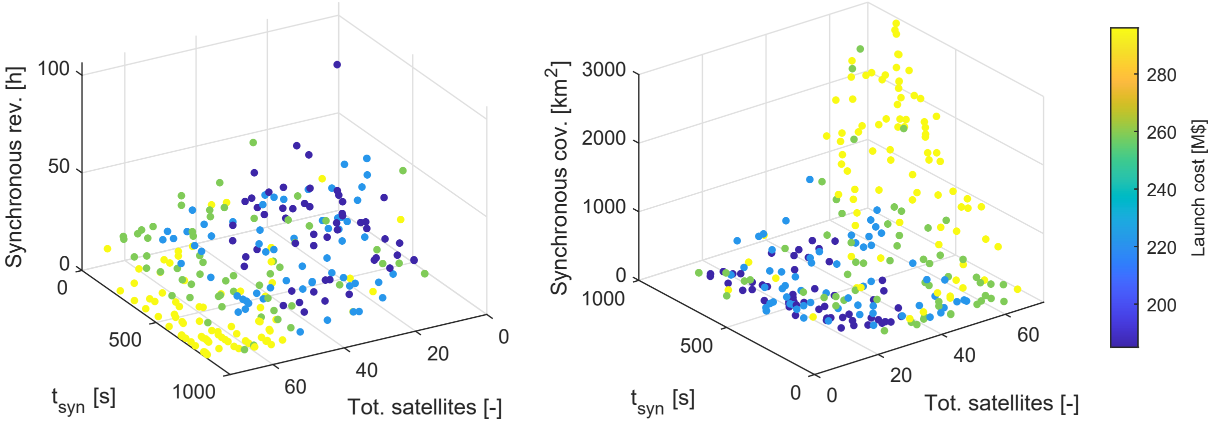

Figure 7.14: Pareto front of the constellation designs with optical satellites on Sun-synchronous orbits and SAR on generally inclined orbits. The left scatter plot illustrates the total number of satellites (f_1), the launch cost (f_2), the synchronous mean revisit time (f_3), and the synchronicity time (f_5). The right scatter plot has on the z-axis the daily synchronous coverage (f_4) in place of the synchronous mean revisit time.

The relationship between the number of satellites and synchronous performance is similar to the ones shown with the previous two configurations, as shown in Figure 7.15. In Figure 7.15a is shown the relation between the number of satellites and the synchronous mean revisit time, such that a larger constellation implies a lower synchronous revisit. In Figure 7.15b is illustrated the compromise between the number of satellites and the synchronous coverage. Synchronous coverage increases with the number of satellites. The synchronicity time t_{syn} influences both the synchronous mean revisit time and the synchronous daily coverage, such that a longer syncrhonicity time enable more frequent revisits and a wider coverage.

The trade-off between the number of planes and the synchronous performance is reported in Figure 7.16. As already found in the previous cases, the solutions with a higher number of planes can provide a better synchronous revisit time and synchronous coverage. The

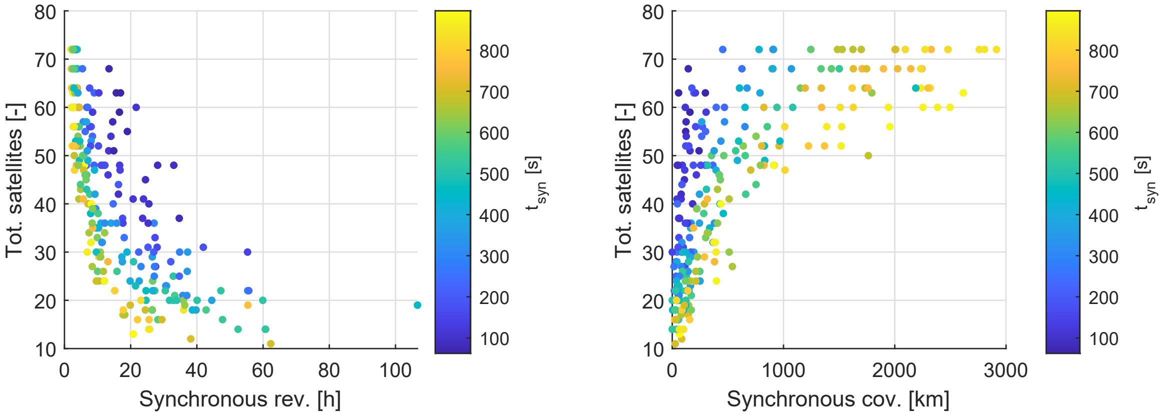

(a) Trade-off between the number of satellites, the synchronous mean revisit time and the synchronicity time.

(b) Trade-off between the number of satellites, the synchronous daily coverage and the synchronicity time.

Figure 7.15: Trade-off between the total number of satellites and synchronous performance (hybrid inclined-SSO).

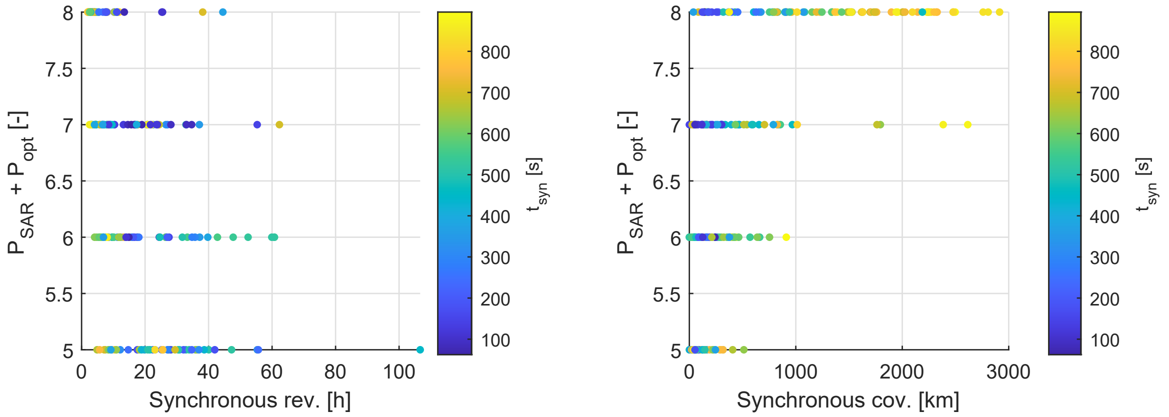

(a) Trade-off between the number of planes, synchronous mean revisit time and synchronicity time.

(b) Trade-off between the number of planes, synchronous daily coverage and synchronicity time.

Figure 7.16: Trade-off between the number of planes and the synchronous performance (hybrid inclined-SSO).

trade-off between launch cost, number of planes and number of satellites is reported in Figure 7.17. In this case, the launch cost depends only on the number of planes and not on the number of satellites because one launch per plane is exploited, so the launcher capacity is never saturated in the solutions.

Finally, the performances of the SAR constellation as a function of the number of SAR satellites are reported in Figure 7.18. The plot also shows a high diversity of solutions because a wider domain is considered compared to the previous cases. In fact, solutions with up to 36 SAR satellites were considered in this case.

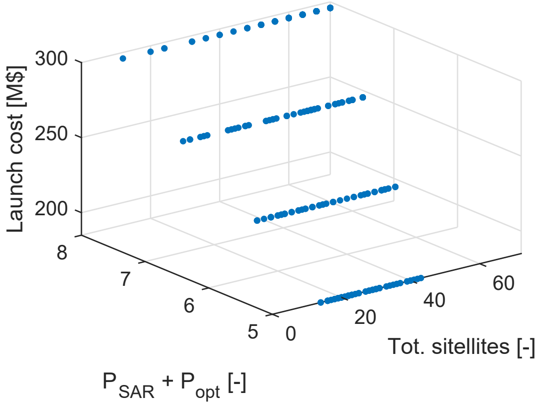

Figure 7.17: Launch cost as a function of the number of planes and the number of satellites (hybrid inclined-SSO).

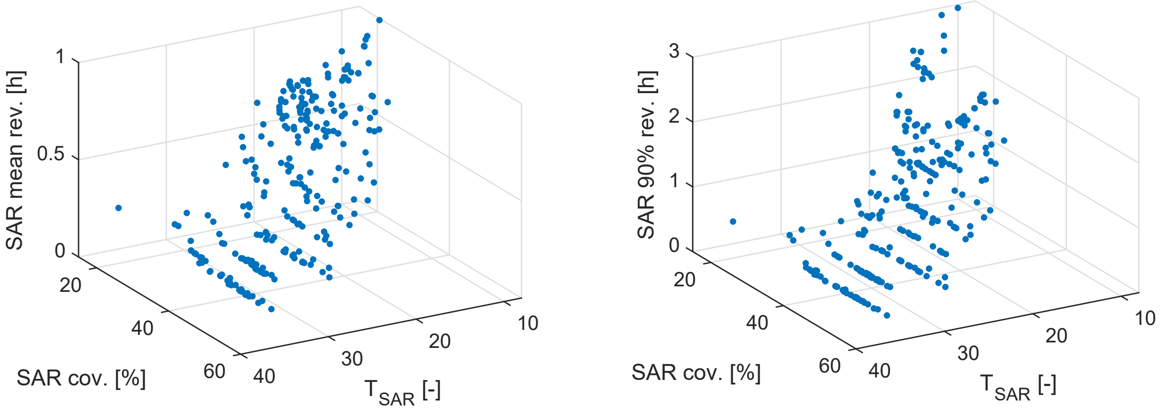

(a) SAR mean revisit time as a function of the SAR coverage in 12 h and the number of SAR satellites.

(b) SAR 90th percentile revisit time as a function of the SAR coverage in 12 h and the number of SAR satellites (hybrid inclined-SSO).

Figure 7.18: Scatter plots of the SAR performance vs number of SAR satellites (hybrid inclined-SSO).

7.4. Selected constellations

Five constellations have been selected for the final comparison between the three orbital configurations. Two different selection approaches are proposed: a performance-driven and a cost-driven selection approach. With the first method, the desired performances are imposed by the designer so that the most affordable option that respects the desired performance is selected. On the contrary, with the second approach, the constellation is selected based on the desired cost.

7.4.1. Performance-driven selection

With the performance-driven selection, the performance of the constellation is imposed, and the most affordable option with the given performance is selected. It can be challenging to define what is the most affordable solution; however, in our case, the constellation with the smaller number of satellites is selected. With an equal number of satellites, the lowest launch cost is considered. With an equal number of satellites and launch costs, the lowest RAAN shift between optical and SAR satellites is considered (only with the Walker inclined and Walker SSO patterns). As an example, three constellations with the following performance are selected:

- Mean synchronous revisit time < 12 h.
- Synchronoicity time < 180 s.

Orbital pattern	Sensor	T	P	F	i	H
Walker inclined	SAR	20	4	3	50.31°	531.9 km
	Opt.	12	4	3	50.31°	597.7 km
Walker SSO	SAR	25	5	2	97.93°	543.0 km
	Opt.	25	5	4	97.57°	636.4 km
Hybrid inclined-SSO	SAR	32	4	2	51.64°	469.4 km
	Opt.	16	4	3	97.82°	608.9 km

Table 7.1: Main parameters of the constellations selected with a performance-driven approach.

This is quite a demanding performance; however, less demanding performance can also be considered based on the specific needs. The three selected constellations belong to one of the three configurations, namely Walker inclined, Walker SSO, and hybrid inclined-SSO. The main parameters of the three constellations are reported in Table 7.1. The Walker inclined configuration meets the desired performance with the smallest number of satellites. On the contrary, the Walker SSO configuration needs the largest number of satellites and planes.

The three configurations are shown in Figure 7.19. The RAAN shift $\Delta\Omega$ for the Walker inclined, and the Walker SSO is 8.1° and -7.0°, respectively. Instead, the optical satellites of the Hybrid inclined-SSO configuration are placed on orbits with LTAN at 9:20, 10:10, 13:50, and 14:40.

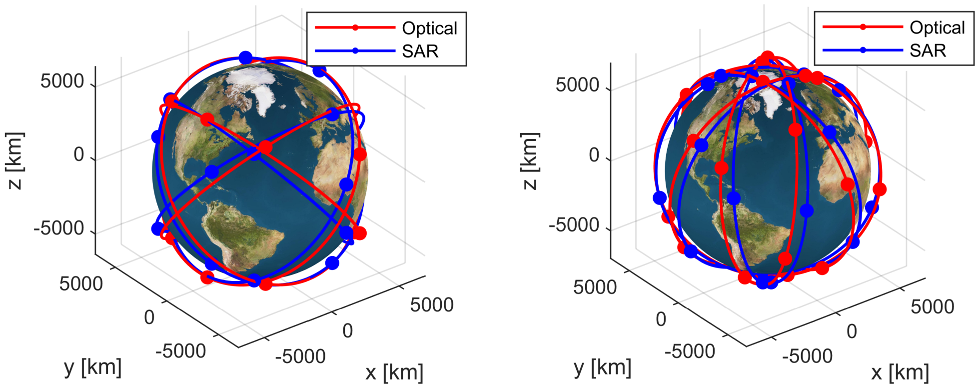

(a) Walker inclined orbital pattern.

(b) Walker SSO orbital pattern.

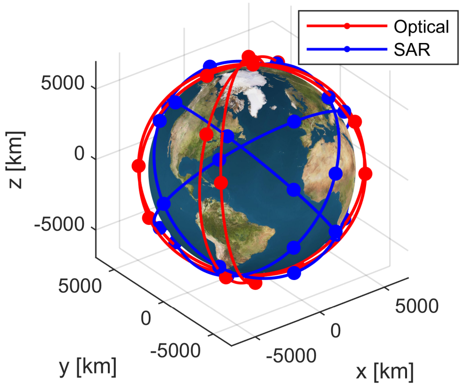

(c) Orbital pattern with SAR satellites on generally inclined orbits and optical satellites on Sun-synchronous orbits.

Figure 7.19: Constellations selected with a performance-driven apporach.

In Figure 7.20 it is shown the performances related to the synchronous mean revisit time as a function of the synchronicity time. The analysis has been done over the equinoxes and solstices, adopting a simulation period of 14 days and the starting days of the simulation: 13 March 2026, 14 June 2026, 16 September 2026, and 14 December 2026.

In Figures 7.20a, 7.20c and 7.20e is shown the synchronous revisit time as a function of different synchronicity times in the 1-30 minutes rages. The three patterns have similar performances for small values of the synchronicity time because of the selection method.

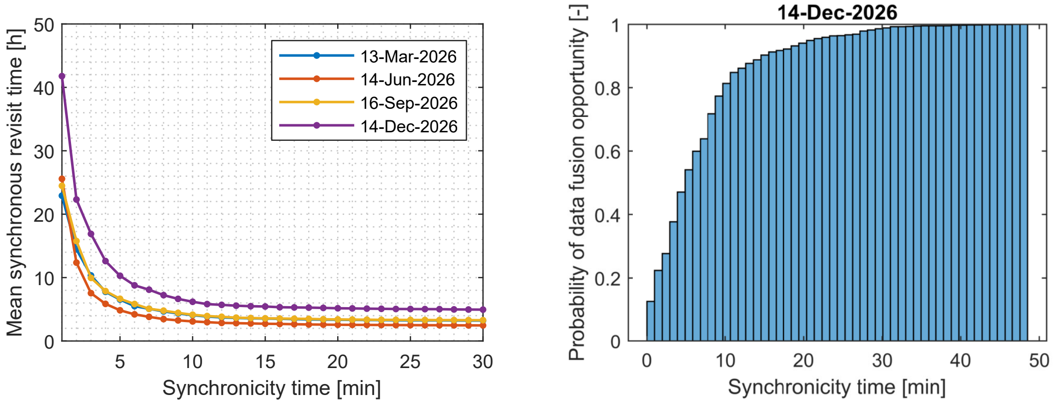

(a) Synchronous mean revisit time vs synchronicity time (Walker inclined).

(b) Comulative distribution function of data fusion opportunities as a function of the synchronicity time (Walker inclined).

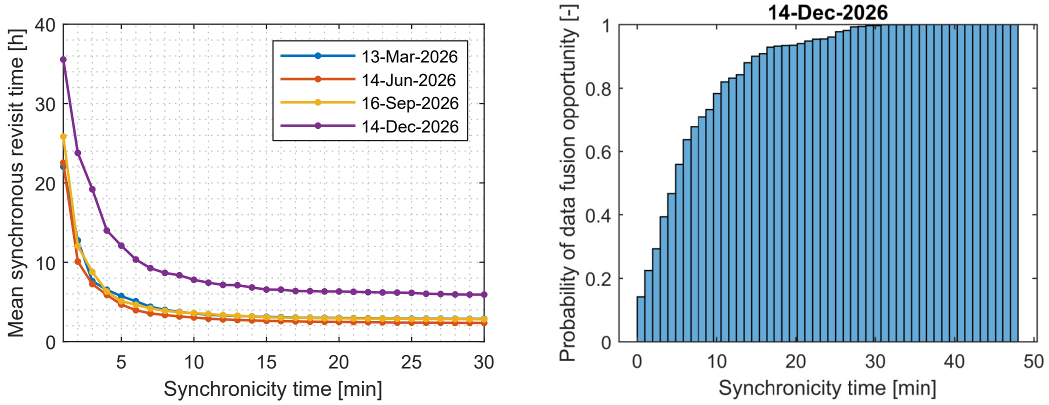

(c) Synchronous mean revisit time vs synchronicity time (Walker SSO).

(d) Comulative distribution function of data fusion opportunities as a function of the synchronicity time (Walker SSO).

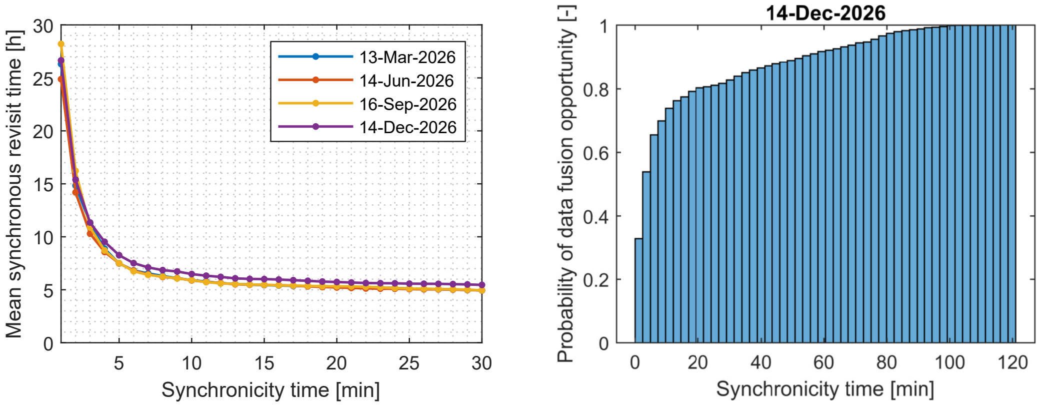

(e) Synchronous mean revisit time vs synchronicity time (hybrid inclined-SSO).

(f) Comulative distribution function of data fusion opportunities as a function of the synchronicity time (hybrid inclined-SSO).

Figure 7.20: Synchronous revisit performances as a function of the synchronicity time of the constellations selected with a performance-driven apporach.

However, for higher values of synchronicity time, the hybrid inclined-SSO pattern has slightly higher values of synchronous revisit time because the optical constellation is limited by the fact that can acquire images only at 9:20, 10:10, 13:50, and 14:40, i.e. the values of the LTAN. It is also possible to notice the influence of the seasonality on the results; In general, the performance during the summer solstice is the best, while the performance during the winter solstice is the worst, simply because of the higher number of light hours during summer. For the same reason, the synchronous revisit times during the equinoxes are generally in the middle. Nevertheless, the hybrid inclined-SSO pattern shown in Figure 7.20e gives the most consistent results over the four seasons, with only a slight performance deterioration during winter. This is because the smart selection of LTAN ranges for the optical satellites ensures good illumination conditions over the four seasons. Furthermore, a kind of horizontal asymptote can be observed when the synchronicity time tends to the SAR mean revisit time. This happens because, for every optical revisit, it is very likely to have a SAR revisit that is within the SAR revisit time. Moreover, it can be noticed that even if the three constellations are optimised for a very short synchronicity time that is lower than 3 minutes, it is possible to achieve more frequent revisits by relaxing the synchronicity requirement. This is also shown in the three histograms in Figures 7.20b, 7.20d and 7.20f, in which is reported the cumulative distribution function of the data fusion opportunities as a function of different synchronicity time requirements. These histograms show that it is more likely to have a mixed optical-SAR revisit within a long time interval than having them in a short one. The winter solstice is taken as an example for the analysis in Figures 7.20b, 7.20d and 7.20f since there is little variability among the seasons.

The synchronous coverage is analysed in Figure 7.21. Two different time scales of synchronicity time are analysed, namely the 1-30 minutes interval and the 1-24 hours interval. In Figures 7.21a, 7.21c and 7.21e it is shown the synchronous daily coverage as a function of different synchronicity times in the 1-30 minutes rages, while in Figures 7.21a, 7.21c and 7.21e the 1-24 hours interval is considered. The synchronous coverage of the Walker SSO pattern shown in Figures 7.21c and 7.21d is the worst among the three constellation patterns. On the contrary, the Walker inclined in Figures 7.21a and 7.21b can generally provide the best coverage. Nevertheless, the hybrid inclined-SSO pattern shown in Figures 7.21e and 7.21f provides almost constant performances during the seasons, with only a slightly lower synchronous coverage during the winter solstice. On the contrary, the other patterns experience more seasonal effects, especially the Walker SSO (Figures 7.21c and 7.21d).

It can be noticed that the synchronous coverage is very small, in particular for small

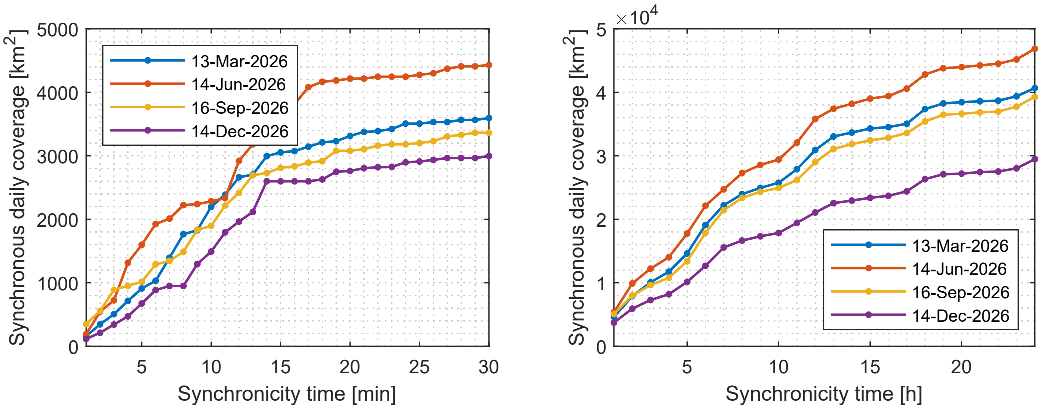

(a) Walker inclined pattern and $t_{syn} \in [1, 30]$ minutes.

(b) Walker inclined pattern and $t_{syn} \in [1, 24]$ hours.

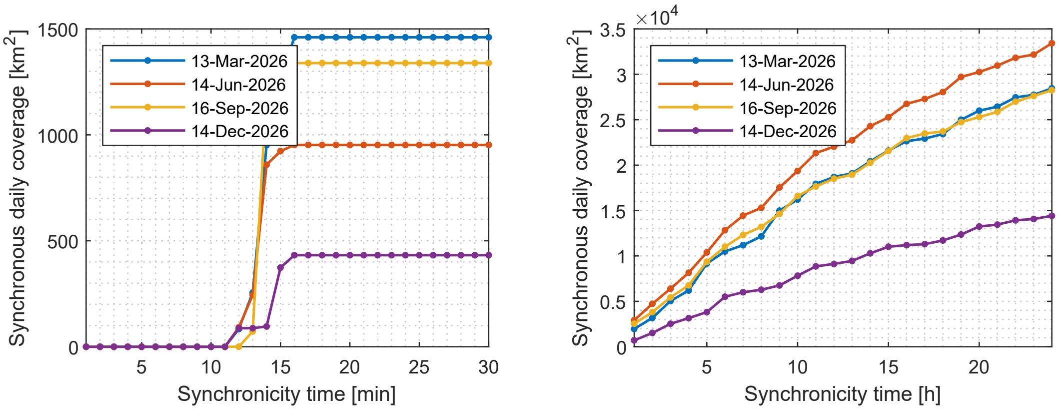

(c) Walker SSO pattern and $t_{syn} \in [1, 30]$ minutes.

(d) Walker SSO pattern and $t_{syn} \in [1, 24]$ hours.

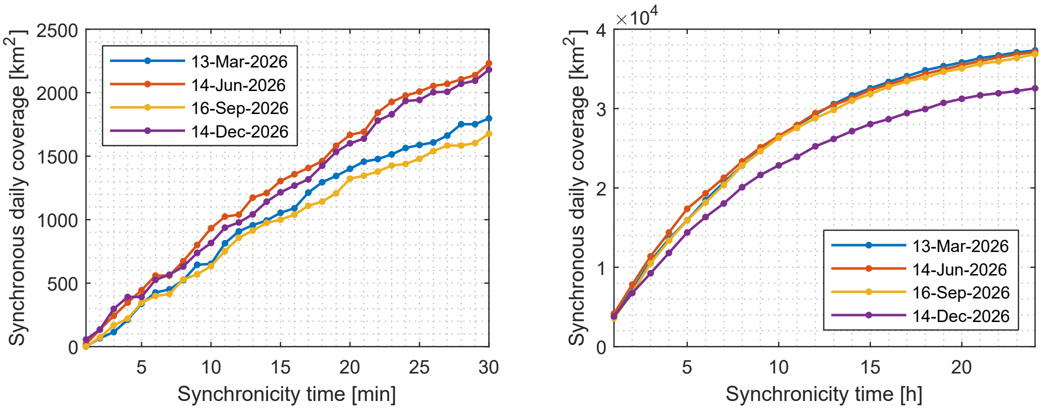

(e) Hybrid inclined-SSO pattern and $t_{syn} \in [1, 30]$ minutes.

(f) Hybrid inclined-SSO pattern and $t_{syn} \in [1, 24]$ hours.

Figure 7.21: Synchronous daily coverage as a function of the synchronicity time of the constellations selected with a performance-driven appoach.

values of synchronicity time. However, this coverage tends to be underestimated for the way in which it is obtained, as it supposes that the instruments work with a fixed look angle. In a real case scenario, this is not true since the constellation is scheduled, and the constellation resources are optimised to maximise the coverage.

The cost and performance over Italy of the selected constellations are summarised in Table 7.2.

	Walker inclined	**Walker SSO**	**Hybrid inclined-SSO**
T_{SAR}	20	25	32
T_{opt}	12	25	16
P_{SAR}	4	5	4
P_{opt}	4	5	4
Launch mass	1181 kg	1503 kg	1200 kg (SAR), 841 kg (opt.)
# Launches	4	5	8
SAR mean revisit time	19 min	16.5 min	13.3 min
SAR 90th percentile revisit time	36 min	32.5 min	22.8 min
SAR coverage in 12 h	36.4%	35.5%	44.8%
Synchronous revisit time (at $t_{syn} = 3$ min)	7.5–16.9 h	7.3–19.2 h	10.3–11.3 h
Synchronous coverage (at $t_{syn} = 3$ min)	342–888 km	0 km	114–297 km
Synchronous coverage (at $t_{syn} = 3$ h)	7286–12 225 km	2528–6393 km	9246–11 382 km

Table 7.2: Summary of performance and cost drivers of the constellations selected with a preference-driven approach.

7.4.2. Cost-driven selection

With this approach, the constellation is selected starting from the definition of the desired cost drivers. As an example, two constellations with the following cost drivers are selected:

- Total number of satellites = 12.
- Minimum launch cost.
- Minimum RAAN shift ($\Delta\Omega$) if Walker inclined configuration.

Only two constellations are selected in this case, namely, one Walker inclined and one hybrid inclined-SSO. In fact, no Walker SSO constellation with the desired cost has been found since they are all more expensive.

Orbital pattern	Sensor	T	P	F	i	H
Walker inclined	SAR	6	3	1	48.75°	519.5 km
	Opt.	6	3	1	48.75°	567.0 km
Hybrid inclined-SSO	SAR	8	4	1	49.77°	463.4 km
	Opt.	4	4	3	97.76°	594.2 km

Table 7.3: Main parameters of the constellations selected with a cost-driven approach.

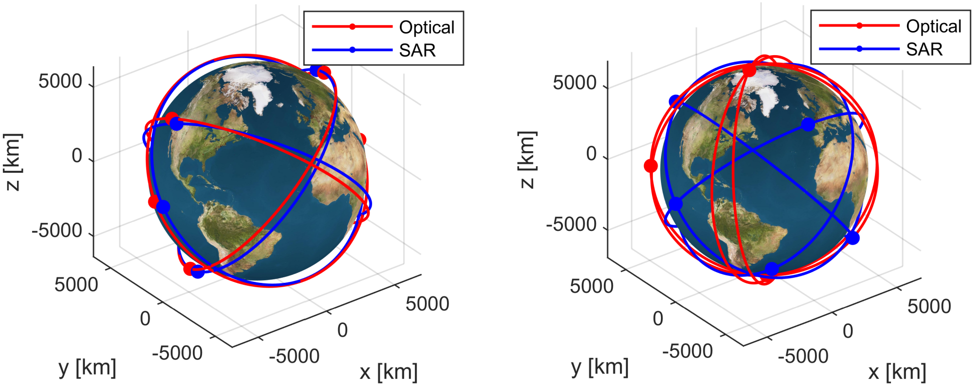

(a) Orbital pattern with generally inclined Walker.

(b) Orbital pattern with SAR satellites on generally inclined orbits, and optical satellites on Sun-synchronous orbits.

Figure 7.22: Constellations selected with a cost-driven apporach.

The main parameters of the two constellations are reported in Table 7.3. In addition, The RAAN shift $\Delta\Omega$ for the Walker inclined configuration is -6.3°, while the optical satellites of the Hybrid inclined-SSO configuration are placed on orbits with LTAN at 9:20, 10:10, 13:50, and 14:40. The two constellations are shown in Figure 7.22

In Figure 7.23 it is shown the performances related to the synchronous mean revisit time as a function of the synchronicity time. The analysis has been done over the two equinoxes and solstices, adopting a simulation period of 14 days and the starting days of the simulation: 13 March 2026, 14 June 2026, 16 September 2026, and 14 December 2026. The Walker inclined pattern in Figure 7.23a gives better synchronous performances than the hybrid inclined-SSO Figure 7.23c for every value of synchronicity time. Therefore, given an equal number of satellites, the Walker inclined pattern provides the best synchronous revisit. The two constellations were optimised for a synchronicity time of approximately 10 minutes; however, a higher probability of data fusion opportunities can be obtained by relaxing the synchronicity time requirement, as shown in Figures 7.23b and 7.23d.

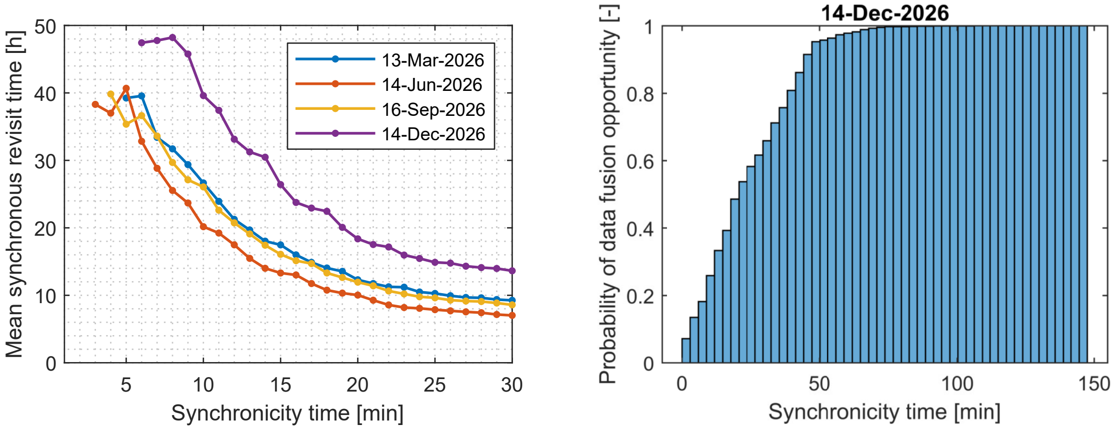

(a) Synchronous mean revisit time vs synchronicity time (Walker inclined).

(b) Comulative distribution function of data fusion opportunities as a function of the synchronicity time (Walker inclined).

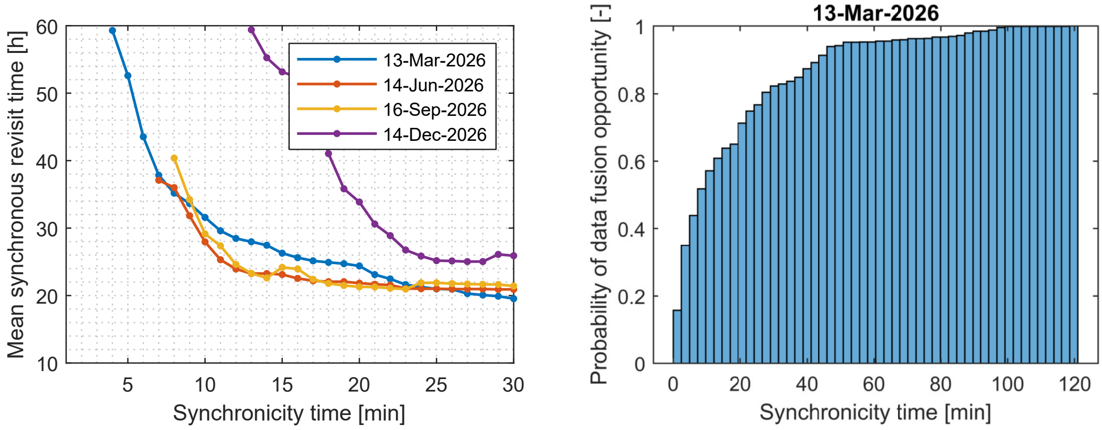

(c) Synchronous mean revisit time vs synchronicity time (hybrid inclined-SSO).

(d) Comulative distribution function of data fusion opportunities as a function of the synchronicity time (hybrid inclined-SSO).

Figure 7.23: Synchronous revisit performances as a function of the synchronicity time of the constellations selected with a cost-driven approach.

The synchronous coverage values of the two constellations are shown in Figure 7.24. Again, the Walker inclined configuration in Figures 7.24a and 7.24b gives the best results compared to the hybrid inclined-SSO in Figures 7.24c and 7.24d in every range of synchronicity time. Nevertheless, the hybrid-SSO configuration can obtain the most consistent performance during the seasons, thanks to the optical satellites placed in SSO.

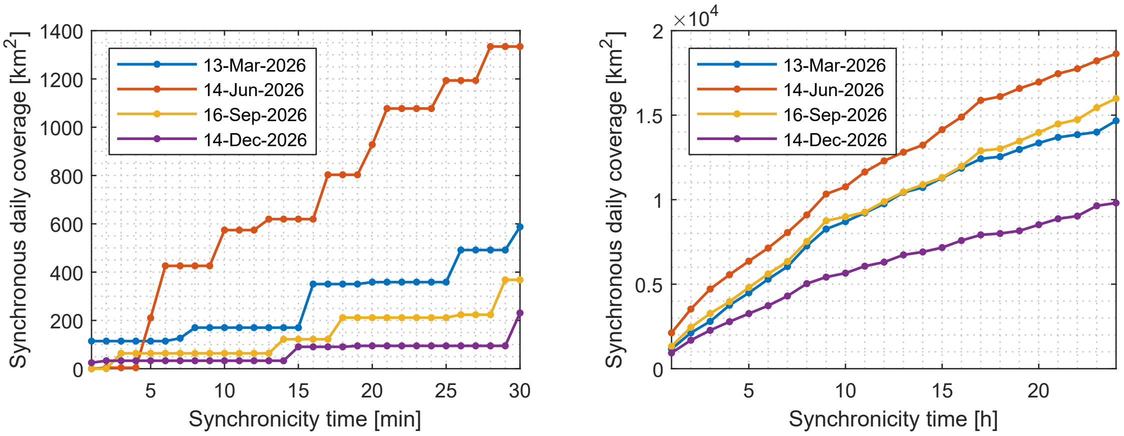

(a) Walker inclined pattern. $t_{syn} \in [1, 30]$ minutes.

(b) Walker inclined pattern. $t_{syn} \in [1, 24]$ hours.

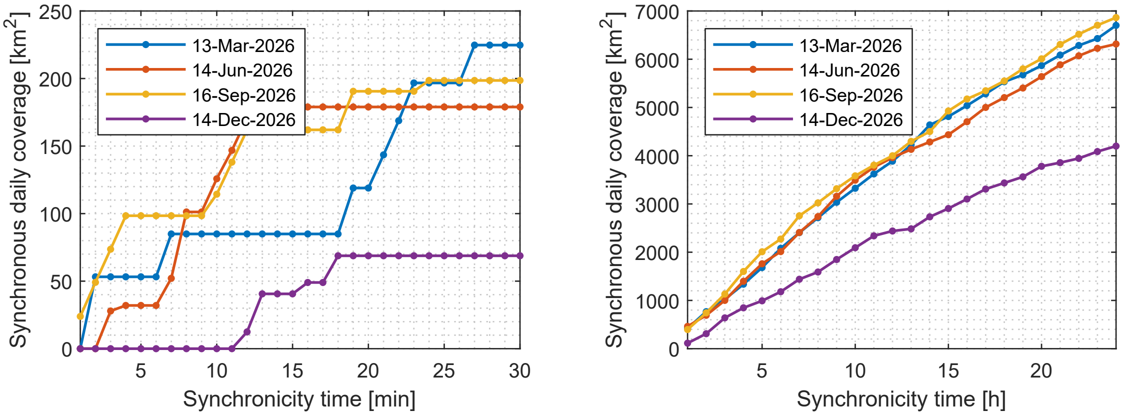

(c) Hybrid inclined-SSO pattern. $t_{syn} \in [1, 30]$ minutes.

(d) Hybrid inclined-SSO pattern. $t_{syn} \in [1, 24]$ hours.

Figure 7.24: Synchronous daily coverage as a function of the synchronicity time of the constellations selected with a cost-driven approach.

The cost and performance over Italy of the selected constellations are summarised in Table 7.4. It can be noticed that the launch mass is very low, in particular for the hybrid inclined-SSO; therefore different launch strategies could be considered, for example employing a smaller and cheaper launcher than the Vega-C. Deployment of redundant spacecraft could also be considered for reliability considerations.

	Walker inclined	**Hybrid inclined-SSO**
T_{SAR}	6	8
T_{opt}	6	4
P_{SAR}	3	4
P_{opt}	3	4
Launch mass	590 kg	301 kg (SAR), 147 kg (opt.)
# Launches	3	8
SAR mean revisit time	66.8 min	52.3 min
SAR 90th percentile revisit time	99.4 min	97.8 min
SAR coverage in 12 h	17.6%	17.2%
Synchronous revisit time (at $t_{syn} = 30\,\text{min}$)	7.0–13.6 h	19.5–26.0 h
Synchronous coverage (at $t_{syn} = 30\,\text{min}$)	231–1334 km	68.8–224.8 km
Synchronous coverage (at $t_{syn} = 3\,\text{h}$)	2272–4714 km	639–1132 km

Table 7.4: Summary of performance and cost drivers of the constellations selected with a cost-driven approach.

8 | Conclusions and future developments

This thesis aimed to address the design problem of a constellation of small optical and SAR satellites to support Italian decision-makers during flood emergency response and monitor critical infrastructures during fast critical events such as ice sleeves formation on overhead power lines.

In order to develop the user and system requirements, two case studies related to emergency response, namely the 2017 Abruzzo snowfall and the 2022 Marche flood in Italy, were analysed. The stakeholders involved in emergency response were identified and placed in a possible operational architecture that includes Earth observation data for timely and effective emergency response. The derived system requirements were used as input for the design process, imposing a 15% coverage of the Italian territory in 12 hours and a revisit time of 3 hours.

Additionally, the peculiar problem of synchronous mixed sensor constellations was investigated. For this category of constellations, the time interval between an optical and a SAR acquisition should be short enough to guarantee good optical-SAR fused data and reduce the temporal decorrelation between the two acquisitions. New figures of merits are proposed for this kind of constellation. Specifically, the synchronicity time is employed as a metric that indicates the required time interval between an optical and a SAR acquisition for data fusion. Additionally, the synchronous revisit measures the time gap between data fusion opportunities, i.e. mixed-sensor acquisitions within the synchronicity time. The synchronous coverage instead represents the surface of the territory of interest sensed by the two instruments within the synchronicity time. These new figures of merits allow the designer to better define the performance of the constellation, even addressing different requirements on the time interval between the two mixed acquisitions.

The constellation design was then formalised as a multi-objective optimisation problem. Moreover, some of the most important sources of uncertainties were addressed. In particular, the coverage and revisit model was validated with STK, and two optimisation algorithms were tested, namely a variation of NSGA-II included in MATLAB and the MOEA/D. The first algorithm was selected for the final optimisation because it better preserves population diversity. However, the uncertainties of the proposed tool should be further investigated in future works to quantify how different optimisation settings can influence the obtained results.

The Pareto set of optimal designs that maximise the synchronous performance and minimise the cost was found. Trade-offs between the objectives were analysed, showing how the synchronicity time impacts the constellation cost, synchronous revisit and coverage. The optimisation of the hybrid constellation was carried out in a single step, differently from the two-step approach of previous research [47]. Moreover, three different constellation patterns are explored: a constellation with optical and SAR satellites on generally inclined orbits, one with optical and SAR satellites on Sun-synchronous orbits and a final one with optical satellites on Sun-synchronous orbits and SAR satellites on inclined orbits. The first pattern with both sensors on generally inclined orbits gives the best results over Italy. In fact, with this pattern, it is possible to meet the desired performance with the lowest number of satellites or achieve the best performance at a fixed cost. However, the feasibility of this pattern should be better addressed, as it requires a change of plane manoeuvre that can be too expensive to obtain. Moreover, this pattern shows variable performance among the seasons. On the contrary, placing optical satellites on Sun-synchronous orbits makes it possible to have a more consistent performance during the year. Furthermore, different configurations or even asymmetric patterns are possible and could be explored in future works.

Additionally, the coverage problem of optical and SAR satellites should be further researched. This work evaluated the coverage by assuming a fixed instrument look-angle and SAR satellites operating in Stripmap mode. This approximation tends to underestimate the actual coverage obtainable by both instruments. Indeed, in a real-case scenario, satellites operate with a variable direction of the line-of-sight, optimised based on the available resources. Moreover, SAR satellites can also employ different acquisition modes, such as ScanSAR and Spotlight, and not only Stripmap. These modes are exploited based on the requested needs. For example, if a wider area must be observed, ScanSAR mode can be adopted at the cost of a lower resolution. On the contrary, Spotlight mode is employed when higher resolution data are needed, at the cost of a lower coverage. Furthermore, the SAR duty cycle was simplistically taken into account; in fact, the satellites were considered to be turned on consecutively for 60 seconds when passing over Italy, but in a real mission, the satellite can optimally exploit the available power alternately turning on and off the sensors when needed, avoiding redundant observations. A different modelling tool supported by an optimal scheduler could be used to address the actual coverage capability of the constellation and find relations between the real coverage and the one obtained with the proposed tool of this thesis.

Overall, this work proposes an optimisation tool that could be adopted in a preliminary phase of the design process. It enables the designer to relate the desired performance of a mixed sensor system with a rough cost estimation. In this way, the designer can explore trade-offs and select optimal solutions based on their needs. Moreover, several iterations can be done by progressively reducing the search space and thus refining the results based on the desired performance and cost. Nevertheless, other figures of merit, such as the ground station visibility, data age, response time, and the instrument duty cycle, should be addressed in the following design stage.

Finally, it is worth mentioning that during the preliminary stages of the design, the system is still not completely defined. Therefore, some system parameters were assumed for the optimisation (e.g. spacecraft mass, instrument swath, duty cycle), but they can undergo modifications derived by different trades. For example, the instrument characteristics, like the SAR swath, can still be subjected to many compromises. A wider instrument swath would lead to an increased coverage capability and a reduced number of required satellites. However, a more complex instrument implies increased development costs and spacecraft mass. At the same time, fewer satellites lead to a decreased revisit time. The proposed code can be employed to study these trades, but several runs with different inputs are needed. Employing more advanced computational tools, such as high-performance computing (HPC), could reduce the running time by solving many problems in parallel. Moreover, HPC can enable the employment of more precise models. However, this would lead again to an increased computational cost. Therefore, the increasing availability of HPC opens new questions about their employment and how they can be efficiently exploited in the constellation design problem.

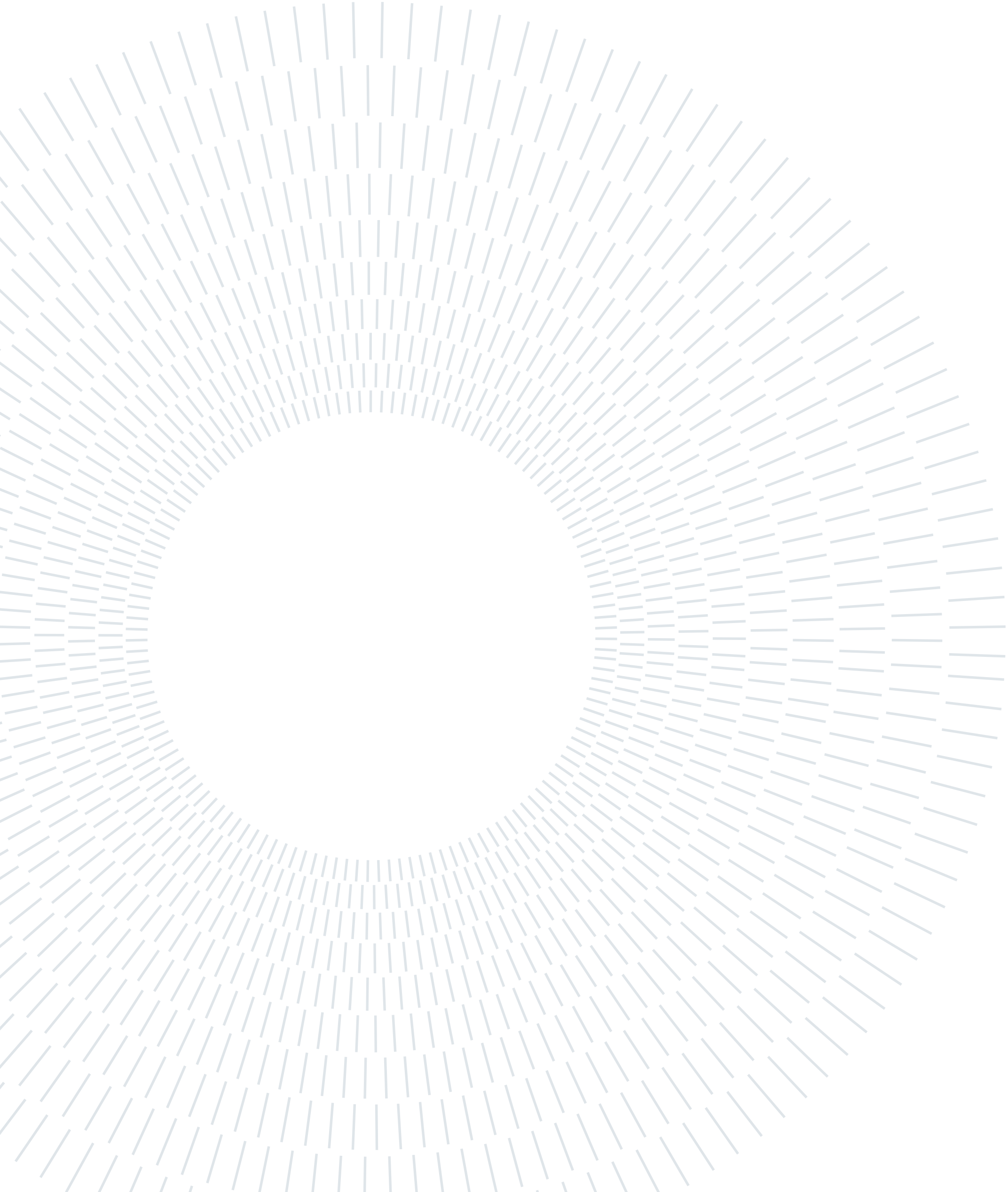

Bibliography

[1] *Newcomers Earth Observation Guide | ESA Business Applications*. [Online]. Available: `https://business.esa.int/newcomers-earth-observation-guide` (visited on 03/08/2023).

[2] M. Dalla Mura, S. Prasad, F. Pacifici, P. Gamba, J. Chanussot, and J. A. Benediktsson, "Challenges and Opportunities of Multimodality and Data Fusion in Remote Sensing," *Proceedings of the IEEE*, vol. 103, no. 9, pp. 1585–1601, Sep. 2015, ISSN: 1558-2256. DOI: `10.1109/JPROC.2015.2462751`.

[3] Surrey Satellite Technology LTD., *Applications of Earth Observation*. [Online]. Available: `https://www.ukspace.org/wp-content/uploads/2019/05/The-many-uses-of-Earth-Observation-data.pdf`.

[4] H.-O. Pörtner, D. Roberts, H. Adams, *et al.*, *Climate Change 2022: Impacts, Adaptation and Vulnerability* (Technical Summary). Cambridge, UK and New York, USA: Cambridge University Press, 2022, pp. 37–118, ISBN: 9781009325844.

[5] L. d. O. Pereira, C. d. C. Freitas, S. J. S. Sant'Anna, D. Lu, and E. F. Moran, "Optical and radar data integration for land use and land cover mapping in the brazilian amazon," *GIScience & remote sensing*, vol. 50, no. 3, pp. 301–321, 2013.

[6] T. T. Nguyen, T. D. Pham, C. T. Nguyen, J. Delfos, R. Archibald, K. B. Dang, N. B. Hoang, W. Guo, and H. H. Ngo, "A novel intelligence approach based active and ensemble learning for agricultural soil organic carbon prediction using multispectral and sar data fusion," *Science of The Total Environment*, vol. 804, p. 150 187, 2022.

[7] H. Laurila, M. Karjalainen, J. Kleemola, and J. Hyyppä, "Cereal yield modeling in finland using optical and radar remote sensing," *Remote sensing*, vol. 2, no. 9, pp. 2185–2239, 2010.

[8] F. Dell'Acqua and P. Gamba, "Remote sensing and earthquake damage assessment: Experiences, limits, and perspectives," *Proceedings of the IEEE*, vol. 100, no. 10, pp. 2876–2890, 2012.

[9] Z. Lu, D. Dzurisin, H.-S. Jung, J. Zhang, and Y. Zhang, “Radar image and data fusion for natural hazards characterisation,” *International Journal of Image and Data Fusion*, vol. 1, no. 3, pp. 217–242, 2010.

[10] U. I. Ahmed, B. Rabus, and M. F. Beg, “Sar and optical image fusion for urban infrastructure detection and monitoring,” in *Remote Sensing Technologies and Applications in Urban Environments V*, SPIE, vol. 11535, 2020, pp. 104–116.

[11] D. Polli and F. Dell’Acqua, “Fusion of optical and sar data for seismic vulnerability mapping of buildings,” *Optical remote sensing: advances in signal processing and exploitation techniques*, pp. 329–341, 2011.

[12] *ESA budget by domain 2023*, en. [Online]. Available: `https://www.esa.int/ESA_Multimedia/Images/2023/01/ESA_budget_by_domain_2023` (visited on 03/07/2023).

[13] *About Copernicus | Copernicus.* [Online]. Available: `https://www.copernicus.eu/en/about-copernicus` (visited on 03/07/2023).

[14] *Investimento 4.2: Osservazione della Terra - OpenPNRR*, it. [Online]. Available: `https://openpnrr.it/misure/52` (visited on 03/07/2023).

[15] F. Greco, *Iride, al via il consorzio che svilupperà soluzioni per la costellazione di satelliti*, it, Nov. 2022. [Online]. Available: `https://www.ilsole24ore.com/art/iride-via-consorzio-che-sviluppera-soluzioni-la-costellazione-satelliti-AEHsUIEC` (visited on 03/07/2023).

[16] *Esa-star Publication.* [Online]. Available: `https://esastar-publication-ext.sso.esa.int/ESATenderActions/details/43565` (visited on 03/08/2023).

[17] J. Wertz, *Orbit & constellation design & management, second printing ed. el segundo*, 2009.

[18] R. D. Luders, “Satellite networks for continuous zonal coverage,” *ARS Journal*, vol. 31, no. 2, pp. 179–184, 1961.

[19] L. Rider, “Analytic design of satellite constellations for zonal earth coverage using inclined circular orbits,” *Journal of the Astronautical Sciences*, vol. 34, pp. 31–64, 1986.

[20] D. C. Beste, “Design of satellite constellations for optimal continuous coverage,” *IEEE Transactions on Aerospace and Electronic Systems*, no. 3, pp. 466–473, 1978.

[21] J. Walker, “Some circular orbit patterns providing continuous whole earth coverage,” *Journal of the British Interplanetary Society*, vol. 24, pp. 369–384, 1971.

[22] J. G. Walker, “Continuous whole-earth coverage by circular-orbit satellite patterns,” Royal Aircraft Establishment Farnborough (United Kingdom), Tech. Rep., 1977.

[23] J. G. Walker, "Satellite constellations," *Journal of the British Interplanetary Society*, vol. 37, p. 559, 1984.

[24] J. E. Draim, "Three-and four-satellite continuous-coverage constellations," *Journal of Guidance, Control, and Dynamics*, vol. 8, no. 6, pp. 725–730, 1985.

[25] J. E. Draim, "A common-period four-satellite continuous global coverage constellation," *Journal of Guidance, Control, and Dynamics*, vol. 10, no. 5, pp. 492–499, 1987.

[26] Y. Ulybyshev, "Satellite constellation design for complex coverage," *Journal of Spacecraft and Rockets*, vol. 45, no. 4, pp. 843–849, 2008.

[27] N. Hitomi and D. Selva, "Constellation optimization using an evolutionary algorithm with a variable-length chromosome," in *2018 IEEE Aerospace Conference*, IEEE, 2018, pp. 1–12.

[28] E. Frayssinhes, "Investigating new satellite constellation geometries with genetic algorithms," in *Astrodynamics Conference*, 1996, p. 3636.

[29] W. A. Crossley and E. A. Williams, "Simulated annealing and genetic algorithm approaches for discontinuous coverage satellite constellation design," *Engineering Optimization+ A35*, vol. 32, no. 3, pp. 353–371, 2000.

[30] T. Ely, W. Crossley, and E. Williams, "Satellite constellation design for zonal coverage using genetic algorithms," *The journal of the Astronautical Sciences*, vol. 47, no. 3, pp. 207–228, 1999.

[31] W. Mason, V. Coverstone-Carroll, and J. Hartmann, "Optimal earth orbiting satellite constellations via a pareto genetic algorithm," in *AIAA/AAS Astrodynamics Specialist Conference and Exhibit*, 1998, p. 4381.

[32] W. A. Crossley, "Optimization for aerospace conceptual design through the use of genetic algorithms," in *Proceedings of the First NASA/DoD Workshop on Evolvable Hardware*, IEEE, 1999, pp. 200–207.

[33] E. A. Williams, W. A. Crossley, and T. J. Lang, "Average and maximum revisit time trade studies for satellite constellations using a multiobjective genetic algorithm," *The Journal of the astronautical sciences*, vol. 49, no. 3, pp. 385–400, 2001.

[34] M. Asvial, R. Tafazolli, and B. Evans, "Non-geo satellite constellation design with satellite diversity using genetic algorithm," in *20th AIAA International Communication Satellite Systems Conference and Exhibit*, 2002, p. 2018.

[35] M. P. Ferringer and D. B. Spencer, "Satellite constellation design tradeoffs using multiple-objective evolutionary computation," *Journal of spacecraft and rockets*, vol. 43, no. 6, pp. 1404–1411, 2006.

[36] L. Wang, Y. Wang, K. Chen, and H. Zhang, "Optimization of regional coverage reconnaissance satellite constellation by nsga-ii algorithm," in *2008 International Conference on Information and Automation*, IEEE, 2008, pp. 1111–1116.

[37] T. Savitri, Y. Kim, S. Jo, and H. Bang, "Satellite constellation orbit design optimization with combined genetic algorithm and semianalytical approach," *International Journal of Aerospace Engineering*, vol. 2017, 2017.

[38] D. Yan, P. You, C. Liu, S. Yong, and D. Guan, "Constellation multi-objective optimization design based on qos and network stability in leo satellite broadband networks," *KSII Transactions on Internet and Information Systems (TIIS)*, vol. 13, no. 3, pp. 1260–1283, 2019.

[39] D. Yan, C. Liu, P. You, and S. Yong, "Multi-objective optimization design of extended walker constellation for global coverage services," in *2016 2nd IEEE International Conference on Computer and Communications (ICCC)*, IEEE, 2016, pp. 1309–1313.

[40] K. Machii, K. Chiba, and Y. Kawakatsu, "Feedback-circulating optimum design for perceiving constellation principle of regional observation satellites," in *2021 IEEE Symposium Series on Computational Intelligence (SSCI)*, IEEE, 2021, pp. 1–8.

[41] C. M. Deccia, D. N. Wiese, and R. S. Nerem, "Using a multiobjective genetic algorithm to design satellite constellations for recovering earth system mass change," *Remote Sensing*, vol. 14, no. 14, p. 3340, 2022.

[42] P. M. Reed, J. B. Kollat, M. P. Ferringer, and T. G. Thompson, "Parallel evolutionary multi-objective optimization on large, heterogeneous clusters: An applications perspective," *Journal of Aerospace Computing, Information, and Communication*, vol. 5, no. 11, pp. 460–478, 2008.

[43] W. R. Whittecar and M. P. Ferringer, "Global coverage constellation design exploration using evolutionary algorithms," in *AIAA/AAS Astrodynamics Specialist Conference*, 2014, p. 4159.

[44] H. Yi, W. Lei, F. Wenju, Z. Haitao, L. Tao, X. Beizhen, and C. Ruizhi, "Leo navigation augmentation constellation design with the multi-objective optimization approaches," *Chinese Journal of Aeronautics*, vol. 34, no. 4, pp. 265–278, 2021.

[45] X. Xu, Z. Ju, and J. Luo, "Design of constellations for gnss reflectometry mission using the multiobjective evolutionary algorithms," *IEEE Transactions on Geoscience and Remote Sensing*, vol. 60, pp. 1–15, 2022.

[46] J. Hu, H. Huang, L. Yang, and Y. Zhu, "A multi-objective optimization framework of constellation design for emergency observation," en, *Advances in Space Research*, vol. 67, no. 1, pp. 531–545, Jan. 2021, ISSN: 02731177. DOI: `10.1016/j.asr.2020.`

09.031. [Online]. Available: `https://linkinghub.elsevier.com/retrieve/pii/S0273117720306785` (visited on 12/14/2022).

[47] C. Chiatante, "High revisit mixed optical-sar microsatellite constellations: A multiobjective genetic algorithm optimisation design approach in an agriculture emergency use case," Supervisors: Camilla Colombo and L. Soli, M.Sc. Thesis, Politecnico di Milano, Faculty of Industrial Engineering, Department of Aerospace Science and Technologies, Thales Alenia Space S.p.A, 2022.

[48] V. Sartoretto, "Precision farming and sustainability: Optimisation of a radar microsatellites constellation for italian agriculture," Supervisors: Camilla Colombo, Luca Soli, Franco Bernelli Zazzera, M.Sc. Thesis, Politecnico di Milano, Faculty of Industrial Engineering, Department of Aerospace Science and Technologies, Thales Alenia Space S.p.A, 2021.

[49] *Find Pareto front of multiple fitness functions using genetic algorithm - MATLAB gamultiobj - MathWorks Italia*. [Online]. Available: `https://it.mathworks.com/help/gads/gamultiobj.html` (visited on 03/26/2023).

[50] Q. Zhang and H. Li, "MOEA/D: A multiobjective evolutionary algorithm based on decomposition," *IEEE Transactions on evolutionary computation*, vol. 11, no. 6, pp. 712–731, 2007.

[51] S. Huang, "Multi-phase mission analysis and design for satellite constellations with low-thrust propulsion," Under sup. of C. Colombo, Ph.D. dissertation, Politecnico di Milano, 2021.

[52] I. S. Sanad, "Reduction of earth observation system response time using relay satellite constellations," Ph.D. dissertation, University of British Columbia, 2020.

[53] D. A. Vallado, *Fundamentals of astrodynamics and applications*. Springer Science & Business Media, 2001, vol. 12.

[54] J. R. Wertz, D. F. Everett, and J. J. Puschell, *Space mission engineering: the new SMAD*. Microcosm Press, 2011.

[55] J. R. Wertz, "Assessment of smallsat utility and the need for dedicated, low-cost, responsive small satellite launch," in *8th Responsive Space Conference. Los Angeles, CA, March*, 2010, pp. 8–11.

[56] M. Padoan, "Methods for assessing the coverage performance of satellite constellations," Supervisors: Camilla Colombo, Arnaud Boutonnet, M.Sc. Thesis, Politecnico di Milano, Master in Space Engineering, 2021.

[57] A. Flores, K. Herndon, R. Thapa, and E. Cherrington, "Synthetic Aperture Radar (SAR) Handbook: Comprehensive Methodologies for Forest Monitoring and Biomass Estimation," en, Tech. Rep., 2019, Publisher: NASA. DOI: `10.25966/NR2C-S697`.

[Online]. Available: `https://gis1.servirglobal.net/TrainingMaterials/SAR/SARHB_FullRes.pdf` (visited on 08/04/2022).

[58] A. Moreira, P. Prats-Iraola, M. Younis, G. Krieger, I. Hajnsek, and K. P. Papathanassiou, “A tutorial on synthetic aperture radar,” *IEEE Geoscience and Remote Sensing Magazine*, vol. 1, no. 1, pp. 6–43, Mar. 2013, Conference Name: IEEE Geoscience and Remote Sensing Magazine, ISSN: 2168-6831. DOI: `10.1109/MGRS.2013.2248301`.

[59] I. H. Woodhouse, *Introduction to microwave remote sensing*, en. Boca Raton: Taylor&Francis, 2006, ISBN: 978-0-415-27123-3.

[60] ESA, *Biomass*, en. [Online]. Available: `https://www.esa.int/Applications/Observing_the_Earth/FutureEO/Biomass` (visited on 10/25/2022).

[61] eoPortal, *Biomass*. [Online]. Available: `https://www.eoportal.org/satellite-missions/biomass#eop-quick-facts-section` (visited on 10/25/2022).

[62] Airbus, *Airbus Defence and Space signs contract to build Biomass – the European Space Agency’s forest mission | Airbus*, en, Section: Company, May 2016. [Online]. Available: `https://www.airbus.com/en/newsroom/press-releases/2016-05-airbus-defence-and-space-signs-contract-to-build-biomass-the` (visited on 10/25/2022).

[63] A. Freeman, W. T. Johnson, B. e. a. Huneycutt, R. Jordan, S. Hensley, P. Siqueira, and J. Curlander, “The "Myth" of the minimum SAR antenna area constraint,” *IEEE Transactions on Geoscience and Remote Sensing*, vol. 38, no. 1, pp. 320–324, 2000.

[64] I. Douidar, M. Safy, and A. Saleh, “Frequency analysis of sar system design for small satellite,” in *IOP Conference Series: Materials Science and Engineering*, IOP Publishing, vol. 1172, 2021, p. 012 013.

[65] A. Garcia Mondejar, “Feasibility study on sar systems on small satellites,” 2009.

[66] A. Ferretti, C. Prati, and F. Rocca, “Permanent scatterers in sar interferometry,” *IEEE Transactions on geoscience and remote sensing*, vol. 39, no. 1, pp. 8–20, 2001.

[67] S.-E. Qian, *Hyperspectral satellites and system design*. CRC Press, 2020.

[68] K. Gulzar, *Camera design for pico and nano satellite applications*, 2010.

[69] D. Carr, *How To Calculate Field of View In Photography*, en-US, Mar. 2016. [Online]. Available: `https://shuttermuse.com/calculate-field-of-view-camera-lens/` (visited on 04/16/2023).

[70] L. Alessandrini, S. Bastia, P. Bertuccioli, *et al.*, *Civil protection in italy. basic training in civil protection*, 2022.

[71] "WMO atlas of mortality and economic losses from weather, climate and water extremes (1970–2019)," World Meteorological Organization (WMO), Tech. Rep., 2021.

[72] B. Bednar-Friedl, R. Biesbroek, D. Schmidt, *et al.*, "Europe," in *Climate Change 2022: Impacts, Adaptation and Vulnerability. Contribution of Working Group II to the Sixth Assessment Report of the Intergovernmental Panel on Climate Change*, H. O. Pörtner, D. C. Roberts, M. Tignor, *et al.*, Eds. Cambridge, UK and New York, USA: Cambridge University Press, 2022, pp. 1817–1927, ISBN: 9781009325844. DOI: `10.1017/9781009325844.015.1817`.

[73] "Dissesto idrogeologico in italia: Pericolosità e indicatori di rischio," Istituto Superiore per la Protezione e la Ricerca Ambientale (ISPRA), Tech. Rep., 2021.

[74] S. K. Kuntla, "An era of Sentinels in flood management: Potential of Sentinel-1, -2, and -3 satellites for effective flood management," en, *Open Geosciences*, vol. 13, no. 1, pp. 1616–1642, Dec. 2021, ISSN: 2391-5447. DOI: `10.1515/geo-2020-0325`. [Online]. Available: `https://www.degruyter.com/document/doi/10.1515/geo-2020-0325/html` (visited on 11/18/2022).

[75] V. Klemas, "Remote Sensing of Floods and Flood-Prone Areas: An Overview," en, *Journal of Coastal Research*, vol. 314, pp. 1005–1013, Jul. 2015, ISSN: 0749-0208, 1551-5036. DOI: `10.2112/JCOASTRES-D-14-00160.1`. [Online]. Available: `http://www.bioone.org/doi/10.2112/JCOASTRES-D-14-00160.1` (visited on 11/18/2022).

[76] K. Irwin, D. Beaulne, A. Braun, and G. Fotopoulos, "Fusion of sar, optical imagery and airborne lidar for surface water detection," *Remote Sensing*, vol. 9, no. 9, p. 890, 2017.

[77] M. Bruch, V. Münch, M. Aichinger, M. Kuhn, M. Weymann, and G. Schmid, "Power blackout risks - risk management options," *Emerging Risk Initiative – Position Paper*, Nov. 2011, CRO Forum. [Online]. Available: `https://www.preventionweb.net/files/24128_powerblackoutrisks1.pdf`.

[78] *Le reti ad alta, media e bassa tensione in Italia.* [Online]. Available: `https://www.energia-lowcost.com/le-reti-ad-alta-media-e-bassa-tensione-in-italia-differenze-e-tensioni-voltaggi-tipici-in-kv/`.

[79] E. G. Petrova, "Natural Factors of Accidents at Power Transmission Line," en, *IDRiM Journal*, vol. 12, no. 1, Oct. 2022, ISSN: 2185-8322. DOI: `10.5595/001c.38749`. [Online]. Available: `https://www.idrimjournal.com/article/38749-natural-factors-of-accidents-at-power-transmission-line` (visited on 12/30/2022).

[80] P. Bonelli, M. Lacavalla, P. Marcacci, G. Mariani, and G. Stella, "Wet snow hazard for power lines: A forecast and alert system applied in Italy," en, *Natural Hazards and Earth System Sciences*, vol. 11, no. 9, pp. 2419–2431, Sep. 2011, ISSN: 1684-9981. DOI: `10.5194/nhess-11-2419-2011`. [Online]. Available: `https://nhess.copernicus.org/articles/11/2419/2011/` (visited on 12/30/2022).

[81] M. Lacavalla, P. Marcacci, and A. Frigerio, "Forecasting and monitoring wet-snow sleeve on overhead power lines in Italy," en, in *2015 IEEE Workshop on Environmental, Energy, and Structural Monitoring Systems (EESMS) Proceedings*, Trento, Italy: IEEE, Jul. 2015, pp. 78–83, ISBN: 978-1-4799-8215-8. DOI: `10.1109/EESMS.2015.7175856`. [Online]. Available: `http://ieeexplore.ieee.org/document/7175856/` (visited on 12/30/2022).

[82] D. Szabó, L. Rácz, G. Göcsei, and B. Németh, "DLR-based ice prevention method," en,

[83] L. Matikainen, M. Lehtomäki, E. Ahokas, J. Hyyppä, M. Karjalainen, A. Jaakkola, A. Kukko, and T. Heinonen, "Remote sensing methods for power line corridor surveys," *ISPRS Journal of Photogrammetry and Remote sensing*, vol. 119, pp. 10–31, 2016.

[84] L. Ge, H. Chang, C. Rizos, *et al.*, "Mine subsidence monitoring using multi-source satellite sar images," *Photogrammetric engineering and remote sensing*, vol. 73, no. 3, p. 259, 2007.

[85] C. Iasio, F. Novali, A. Corsini, M. Mulas, M. Branzanti, E. Benedetti, C. Giannico, A. Tamburini, and V. Mair, "Cosmo skymed high frequency-high resolution monitoring of an alpine slow landslide, corvara in badia, northern italy," in *2012 IEEE International Geoscience and Remote Sensing Symposium*, IEEE, 2012, pp. 7577–7580.

[86] L. Jingnan, "Progress in deformation monitoring for dams, bridges and power lines," *Annals of GIS*, vol. 16, no. 2, pp. 81–90, 2010.

[87] L. Soli and D. Calabrese, "SAR-based monitoring of non-visible or non-always-visible or partially visible targets and associated monitoring, critical situation detection and early warning systems and methods," U.S. Patent number 11 402 495 B2, Current Assignee: Thales Alenia Space Italia S.p.A. Aug. 2022.

[88] J. Ahmad, A. S. Malik, L. Xia, and N. Ashikin, "Vegetation encroachment monitoring for transmission lines right-of-ways: A survey," *Electric Power Systems Research*, vol. 95, pp. 339–352, 2013.

[89] K. Deb, "Multi-objective optimization," in *Search methodologies*, E. K. Burke, E. K. Burke, G. Kendall, and G. Kendall, Eds. Springer, 2014, pp. 403–449.

[90] C. A. C. Coello, “Multi-objective Optimization,” en, in *Handbook of Heuristics*, R. Martí, P. M. Pardalos, and M. G. C. Resende, Eds. Cham: Springer International Publishing, 2018, pp. 177–204, ISBN: 9783319071244. DOI: `10.1007/978-3-319-07124-4_17`. [Online]. Available: `https://doi.org/10.1007/978-3-319-07124-4_17` (visited on 12/07/2022).

[91] A. Arias Montao, C. A. Coello Coello, and O. Schtze, “Multiobjective optimization for space mission design problems,” in *Computational Intelligence in Aerospace Sciences*, M. Vasile and V. M. Becerra, Eds. American Institute of Aeronautics and Astronautics, Inc., 2014, pp. 1–46.

[92] N. Hitomi and D. Selva, “The effect of credit definition and aggregation strategies on multi-objective hyper-heuristics,” in *International Design Engineering Technical Conferences and Computers and Information in Engineering Conference*, American Society of Mechanical Engineers, vol. 57083, 2015, V02BT03A030.

[93] M. Laumanns, L. Thiele, K. Deb, and E. Zitzler, “Combining convergence and diversity in evolutionary multiobjective optimization,” *Evolutionary computation*, vol. 10, no. 3, pp. 263–282, 2002.

[94] E. Zitzler, M. Laumanns, and L. Thiele, “SPEA2: Improving the strength pareto evolutionary algorithm,” *TIK-report*, vol. 103, 2001.

[95] J. D. Knowles and D. W. Corne, “Approximating the nondominated front using the Pareto archived evolution strategy,” *Evolutionary computation*, vol. 8, no. 2, pp. 149–172, 2000.

[96] K. Deb, A. Pratap, S. Agarwal, and T. Meyarivan, “A fast and elitist multiobjective genetic algorithm: NSGA-II,” *IEEE transactions on evolutionary computation*, vol. 6, no. 2, pp. 182–197, 2002.

[97] D. W. Corne, J. D. Knowles, and M. J. Oates, “The pareto envelope-based selection algorithm for multiobjective optimization,” in *International conference on parallel problem solving from nature*, Springer, 2000, pp. 839–848.

[98] L. N. De Castro, L. N. Castro, and J. Timmis, *Artificial immune systems: a new computational intelligence approach.* Springer Science & Business Media, 2002.

[99] D. Dasgupta, *Artificial immune systems and their applications.* Springer Science & Business Media, 2012.

[100] J. F. Kennedy, R. C. Eberhart, and Y. Shi, *Swarm intelligence* (The Morgan Kaufmann series in evolutionary computation). San Francisco: Morgan Kaufmann Publishers, 2001, ISBN: 9781558605954.

[101] D. Angus and C. Woodward, “Multiple objective ant colony optimisation,” *Swarm intelligence*, vol. 3, no. 1, pp. 69–85, 2009.

[102] Y. Tian, R. Cheng, X. Zhang, and Y. Jin, "PlatEMO: A MATLAB platform for evolutionary multi-objective optimization," *IEEE Computational Intelligence Magazine*, vol. 12, no. 4, pp. 73–87, 2017.

[103] E. Osaba, E. Villar-Rodriguez, J. Del Ser, A. J. Nebro, D. Molina, A. LaTorre, P. N. Suganthan, C. A. C. Coello, and F. Herrera, "A tutorial on the design, experimentation and application of metaheuristic algorithms to real-world optimization problems," *Swarm and Evolutionary Computation*, vol. 64, p. 100 888, 2021.

[104] *Sentinel-1 sar technical guide.* [Online]. Available: `https://sentinels.copernicus.eu/web/sentinel/technical-guides/sentinel-1-sar`.

[105] eoPortal, *Copernicus: Sentinel-1.* [Online]. Available: `https://www.eoportal.org/satellite-missions/copernicus-sentinel-1`.

[106] *Copernicus open access hub.* [Online]. Available: `https://scihub.copernicus.eu/dhus/#/home`.

[107] eoPortal, *COSMO-SkyMed.* [Online]. Available: `https://www.eoportal.org/satellite-missions/cosmo-skymed`.

[108] M. Battagliere and M. Virelli, *COSMO-SkyMed Mission and Products Description*, English, Italian Space Agency. [Online]. Available: `https://www.asi.it/wp-content/uploads/2019/08/COSMO-SkyMed-Mission-and-Products-Description_rev3-1.pdf`.

[109] eoPortal, *COSMO-SkyMed - Second Generation.* [Online]. Available: `https://www.eoportal.org/satellite-missions/cosmo-skymed-second-generation`.

[110] *COSMO-SkyMed Seconda Generazione: System and Products Description*, English, Italian Space Agency. [Online]. Available: `https://earth.esa.int/eogateway/documents/20142/37627/COSMO-SkyMed-Second-Generation-Mission-Products-Description.pdf`.

[111] eoPortal, *ICEYE.* [Online]. Available: `https://www.eoportal.org/satellite-missions/iceye-constellation#mission--development-status-of-the-iceye-x-satellite-constellation`.

[112] ICEYE, *ICEYE Data Brochure.* [Online]. Available: `https://www.iceye.com/hubfs/Downloadables/SAR_Data_Brochure_ICEYE.pdf`.

[113] ICEYE, *ICEYE Mission Brochure.* [Online]. Available: `https://www.iceye.com/hubfs/_DATA_AND_MISSIONS/Missions_Brochure_ICEYE.pdf`.

[114] *Iceye tasking: Products.* [Online]. Available: `https://www.iceye.com/tasking`.

[115] eoPortal, *Capella constellation.* [Online]. Available: `https://www.eoportal.org/satellite-missions/capella-x-sar#development-status`.

[116] Capella Space, *CAPELLA SPACE SAR IMAGERY PRODUCTS GUIDE.* [Online]. Available: `https://vekom.com/wp-content/uploads/2020/12/Capella_Space_SAR_Imagery_Products_Guide.pdf`.

[117] *Sentinel-2 sar technical guide.* [Online]. Available: `https://sentinels.copernicus.eu/web/sentinel/technical-guides/sentinel-2-msi`.

[118] eoPortal, *Copernicus: Sentinel-2.* [Online]. Available: `https://www.eoportal.org/satellite-missions/copernicus-sentinel-2`.

[119] Planet Labs, *Planet imagery product specifications.* [Online]. Available: `https://earth.esa.int/eogateway/documents/20142/37627/Planet-combined-imagery-product-specs-2020.pdf`.

[120] Planet Labs, *Planet labs specifications: Spacecraft operations & ground systems.* [Online]. Available: `http://content.satimagingcorp.com.s3.amazonaws.com/media/pdf/Dove-PDF-Download`.

[121] *PlanetScope.* [Online]. Available: `https://developers.planet.com/docs/data/planetscope/` (visited on 12/16/2022).

[122] eoPortal, *SkySat Constellation.* [Online]. Available: `https://www.eoportal.org/satellite-missions/skysat`.

[123] ESA, *SkySat - Earth Online.* [Online]. Available: `https://earth.esa.int/eogateway/missions/skysat`.

[124] eoPortal, *BlackSky Constellation.* [Online]. Available: `https://www.eoportal.org/satellite-missions/blacksky-constellation`.

[125] Harris Corporation, *SPACEVIEW 24/35/42 Datasheet.* [Online]. Available: `https://satcatalog.s3.amazonaws.com/components/741/SatCatalog_-_L3Harris_Technologies_-_SpaceView_24_-_Datasheet.pdf?lastmod=20210714221224`.

[126] Airbus Intelligence, *Airbus Intelligence | Our Constellation*, en-US. [Online]. Available: `https://www.intelligence-airbusds.com/imagery/constellation/` (visited on 12/28/2022).

[127] *Mission Summary - EO Handbook - Kompsat-2*, 2022. [Online]. Available: `http://database.eohandbook.com/database/missionsummary.aspx?missionID=407`.

[128] *Mission Summary - EO Handbook - Kompsat-3*, 2022. [Online]. Available: `http://database.eohandbook.com/database/missionsummary.aspx?missionID=637`.

[129] *Mission Summary - EO Handbook - Kompsat-3A*, 2022. [Online]. Available: `http://database.eohandbook.com/database/missionsummary.aspx?missionID=698`.

[130] *Mission Summary - EO Handbook - Kompsat-5*, 2022. [Online]. Available: `http://database.eohandbook.com/database/missionsummary.aspx?missionID=638`.

[131] *Mission Summary - EO Handbook - Kompsat-6*, 2022. [Online]. Available: `http://database.eohandbook.com/database/missionsummary.aspx?missionID=761`.

[132] D. Werner, *Iceye and Satlantis propose optical and radar satellite constellation*, en-US, Sep. 2022. [Online]. Available: `https://spacenews.com/iceye-satlantis-tandem4eo/` (visited on 12/27/2022).

[133] *Audizione Enel 10^a Commissione Senato della Repubblica*, Roma, 8 febbraio 2017. [Online]. Available: `https://senato.it/application/xmanager/projects/leg17/attachments/documento_evento_procedura_commissione/files/000/004/711/2017_02_08_-_Documento_depositato_da_Enel.pdf`.

[134] C. Pasolini, *Il più lungo black out in italia: Da una settimana senza luce e riscaldamento, 7 mila case - la repubblica*, `https://www.repubblica.it/cronaca/2017/01/23/news/il_piu_lungo_black_out_in_italia_da_una_settimana_senza_luce_e_riscaldamento_settemila_case-156672409/`, 2017.

[135] "Le gravi alluvioni nelle Marche," it-IT, *Il Post*, Sep. 2022. [Online]. Available: `https://www.ilpost.it/2022/09/16/alluvioni-marche-morti/` (visited on 11/14/2022).

[136] G. Giampieri, "Alluvione nelle Marche 2022, danni per 2 miliardi: Fango nemico numero uno - Cronaca - ilrestodelcarlino.it," it, *il Resto del Carlino*, Oct. 2022, Section: Marche. [Online]. Available: `https://www.ilrestodelcarlino.it/marche/alluvione-2022-danni-1.8152798` (visited on 11/14/2022).

[137] "Alluvione Marche news, 11 morti e 2 dispersi. Senigallia, una giornata di paura. Diretta - Cronaca," it, *il Resto del Carlino*, Sep. 2022, Section: Marche. [Online]. Available: `https://www.ilrestodelcarlino.it/marche/alluvione-news-diretta-1.8084837` (visited on 11/14/2022).

[138] "Alluvione Marche, i dati di monitoraggio del Cnr-Irpi," *ilgiornaledellaprotezionecivile.it*, [Online]. Available: `https://www.ilgiornaledellaprotezionecivile.it//a/alluvione-marche-i-dati-di-monitoraggio-del-cnr-irpi` (visited on 11/14/2022).

[139] "Perché l'alluvione nelle marche ha causato così tanti danni," it-IT, *Il Post*, Sep. 2022. [Online]. Available: `https://www.ilpost.it/2022/09/17/danni-morti-alluvione-marche/` (visited on 11/17/2022).

[140] "Rapporto di evento preliminare - maltempo 15, 16 e 17 settembre 2022," Centro Funzionale Regionale, Tech. Rep., Sep. 2022. [Online]. Available: `https://www.regione.marche.it/portals/0/Protezione_Civile/Manuali%20e%20Studi/Rapporto_Evento_preliminare_20220915.pdf`.

[141] *Regione Marche - Sistema Informativo Regionale Meteo-Idro-Pluviometrico.* [Online]. Available: `http://app.protezionecivile.marche.it/sol/indexjs.sol?lang=it` (visited on 11/14/2022).

[142] *Allegato 1 - comuni della regione marche per zone di allerta per il rischio idrogeologico ed idraulico.* [Online]. Available: `https://console.regione.marche.it/lprm/PROCEDURE/DSPC_2019_all/Allegato%5C%201-%5C%20Zone%5C%20di%5C%20allerta%5C%20MIG.pdf`.

[143] Francesco Comito [@FrancescComito], *+++ Pesanti disagi e allagamenti nei paesi tra Umbria e Marche. Queste foto arrivano da Cantiano - Emilio Morelli*, it, Tweet, Sep. 2022. [Online]. Available: `https://twitter.com/FrancescComito/status/1570473165717143553` (visited on 11/16/2022).

[144] Comune di Senigallia, *Considerati i livelli alti del fiume di serra de conti, il sindaco massimo olivetti, in via cautelare, ha disposto l'apertura del coc.* it, Sep. 2022. [Online]. Available: `https://www.facebook.com/comune.senigallia/posts/pfbid02K8k1XhmpKrFsRmErGaSXzaBYtRbrCHJK51pRtrJokSscT4ZA7v76jVv3SPrpTPixl` (visited on 11/15/2022).

[145] L. Ceccacci, "Maltempo e allagamenti: Piena del Misa a Senigallia. Ponti, strade e scuole chiuse," italiano (italian), *Senigallia Notizie*, [Online]. Available: `https://www.senigallianotizie.it/1327561723/maltempo-e-allagamenti-attesa-piena-del-misa-senigallia-alza-il-livello-di-allerta` (visited on 11/16/2022).

[146] Francesco Comito [@FrancescComito], *+++ Iniziata l'esondazione del fiume Misa a Senigallia. @Emergenza24 https://t.co/JwE4XPciZo*, it, Tweet, Sep. 2022. [Online]. Available: `https://twitter.com/FrancescComito/status/1570532865049513984` (visited on 11/16/2022).

[147] P. Roques, *Systems architecture modeling with the Arcadia method: a practical guide to Capella.* Elsevier, 2017.

[148] Comune di Senigallia Area Protezione Civile, *Piano di emergenza di protezione civile.* [Online]. Available: `https://www.protezionecivilesenigallia.it/wp-content/uploads/Parte_generale.pdf`.

[149] *myDEWETRA.* [Online]. Available: `https://www.mydewetra.org/`.

[150] Arianespace, *Small Spacecraft Mission Service VEGA-C User's Manual*, Sep. 2020. [Online]. Available: `https://www.arianespace.com/wp-content/uploads/2020/10/SSMS-Vega-C-UsersManual-Issue-1-Rev0-Sept2020.pdf`.

[151] S. Dionisio, A. Anselmi, L. Bonino, S. Cesare, L. Massotti, and P. Silvestrin, "The "Next Generation Gravity Mission": Challenges and consolidation of the system concepts and technological innovations," en, in *2018 SpaceOps Conference*, Mar-

seille, France: American Institute of Aeronautics and Astronautics, May 2018, ISBN: 9781624105623. DOI: `10.2514/6.2018-2495`. [Online]. Available: `https://arc.aiaa.org/doi/10.2514/6.2018-2495` (visited on 02/24/2023).

[152] P. Fortescue, G. Swinerd, and J. Stark, *Spacecraft systems engineering*. John Wiley & Sons, 2011.

[153] Y. Tian, W. Zhu, X. Zhang, and Y. Jin, "A practical tutorial on solving optimization problems via platemo," *Neurocomputing*, vol. 518, pp. 190–205, 2023.